

PhD Thesis
Vassilia Zorba

**Study of electron and ion emission
mechanisms from micro/nano-structured Si
surfaces using ultrashort laser pulses**



Physics Department
University of Crete

Heraklion, December 2007

Table of Contents:

Introduction and Overview	1
Chapter 1: Laser Induced Conical Si Microstructures	5
1.1 Introduction	5
1.2 Laser-Solid Interactions: Fundamental Aspects.....	6
1.2.1 Primary Processes	6
1.2.2 Secondary Processes	7
1.3 Laser Induced Periodic Surface Structures	9
1.3.1 Capillary Waves	10
1.3.2 Preferential material removal.....	12
1.3.3 Laser Induced Chemical Etching	12
1.4 Surface Structuring of Si with Lasers	14
Chapter 2: Experimental Methods	17
2.1 Introduction	17
2.2 Laser Sources	17
2.2.1 The KrF excimer laser system.....	18
2.2.2 The Ti:Sapphire laser system.....	19
2.2.3 The Nd:YVO ₄ laser system.....	19
2.3 Experimental Setup	20
2.4 Sample Preparation	21
2.5 Sample Characterization	22
2.5.1 Morphological, structural and compositional analysis.....	22
2.5.2 Optical absorptance measurements	23
2.5.3 Field emission measurements	24
2.5.4 Wetting properties.....	25

Chapter 3: Morphological / Structural Characterization and Replication	31
3.1 Introduction	31
3.2 Morphological analysis	32
3.2.1 Experiments with the Ti:Sapphire fs laser system	32
3.2.2 Experiments with the Nd:YVO ₄ ps laser system	34
3.2.3 Experiments with the ns, ps and fs KrF laser system.....	36
3.3 Structural and compositional analysis.....	43
3.3.1 General Remarks.....	48
3.4 Mechanistic aspects.....	49
3.4.1 Laser-material interaction	49
3.4.2 The role of the reactive gas (SF ₆).....	51
3.4.3 Growth Mechanisms and Laser Pulse Duration.....	53
3.5 Replication of laser fabricated Si structures.....	55
3.6 Conclusions	59
Chapter 4: Optical Properties of Laser Structured Si	61
4.1 Introduction	61
4.2 Optical Parameters	63
4.3 Optical Measurements.....	64
4.3.1 The effect of the reactive gas pressure.....	65
4.3.2 The effect of laser fluence.....	66
4.3.3 The effect of HF treatment.....	68
4.3.4 The effect of laser pulse duration.....	69
4.3.5 The effect of thermal annealing	70
4.3.6 Discussion	71
4.4 Applications	72
4.5 Conclusions	73

Chapter 5: Field Emission from Laser Structured Si	75
5.1 Introduction.....	75
5.2 Fundamentals of Field Emission.....	77
5.2.1 Field-emission from a metal	77
5.2.2 Field-emission from a semiconductor.....	81
5.3 Field emission from laser structured Si.....	82
5.3.1 The effect of laser pulse duration on field emission	83
5.3.2 Continuous areas vs. spot arrays of Si emitters.....	87
5.4 Applications	90
5.5 Conclusions	91
Chapter 6: Wetting Properties of Laser Structured Si	93
6.1 Introduction.....	93
6.2 Fundamentals	95
6.2.1 Young’s Equation.....	95
6.2.2 Wettability and Surface roughness: Wenzel and Cassie Baxter states	96
6.3 Hydrophobic laser structured Si surfaces.....	98
6.3.1 Morphology and Static Contact Angle Measurements	99
6.3.2 Manipulation of liquids by using surface tension gradients.....	103
6.4 Superhydrophobic laser structured Si surfaces	106
6.4.1 Morphology and Static Contact Angle Measurements	107
6.4.2 Sliding Angle Experiments	109
6.5 Water repellence: laser structured Si vs. the lotus leaf	114
6.6 Electrowetting on Dielectric (EWOD).....	120
6.7 Chemically induced wetting.....	128
6.8 Conclusions and Future Prospects	132
Concluding Remarks	135
Appendix	137

Table of Contents

Relevant Publications	141
References	143

Introduction and Overview

Introduction

Silicon (Si) is a material widely used in electronic and optoelectronic applications. Its properties combined with its abundance and low-cost, have constituted Si as the basis of the integrated circuit (IC) technology and made its use possible in a number of applications in everyday life. Compatibility to this technology as a means of avoiding multilevel interconnects, thus increasing reliability and minimizing manufacturing costs, is very important for commercial viability. But despite the advantages of Si, as in any other material, there are limitations for its use in certain types of applications. In order to overcome these limitations and extend the use of Si based devices in interdisciplinary applications, extensive research has been directed in finding ways to improve silicon's properties

Bottom-up and top-down fabrication approaches have been implemented for addressing this problem. In many cases, the key engineering challenges are related to the application of this technology beyond the laboratory environment. To this end, a significant amount of research effort has been devoted in quest of fabrication techniques with limited processing steps which can optimize and/or extend the properties of Si, in low vacuum and cleanliness conditions.

This thesis describes a method which exploits a number of phenomena taking place under the action of intense pulsed laser irradiation of crystalline Si in the presence

of a reactive gas, in order to induce morphological, structural and compositional modifications on its surface. The resulting structures, apart from their unique (conical) morphology, also exhibit improved optical, electronic and wetting response. In particular, proper tuning of the laser and reactive gas parameters can lead to the formation of structures which exhibit:

- a) Increased absorptance of more than 90% even for below-bandgap wavelengths and throughout a wide spectral range ($250 \text{ nm} < \lambda < 2.5 \text{ }\mu\text{m}$).
- b) Low-threshold field-electron emission, with a threshold as low as $2.5 \text{ V}/\mu\text{m}$, comparable to that observed in some of the best field emitters to date (e.g. carbon nanotubes).
- c) Hydrophobic, or even superhydrophobic and highly water repellent behavior equivalent to that of the “model” superhydrophobic and water repellent natural surface (lotus leaf).

Content and organization

This thesis is organized as follows:

Chapter 1 reviews the basic processes taking place upon the interaction of intense laser pulses with solids (semiconductors) and comments on the formation mechanisms of the conical surface structures on Si.

Chapter 2 shows the experimental setup and instrumentation used for the fabrication of the Si surface structures as well as for their characterization.

In **Chapter 3** we study the morphology of the structures fabricated using different laser sources and reactive gas parameters. We also compare the structure and composition of the morphologies obtained using laser pulses of different duration. Furthermore, we comment on the possible formation mechanisms dominant in each case with respect to our experimental findings. Finally, we show how these structures can be used as “master” morphologies for subsequent transfer of their surface pattern on other materials.

In **Chapter 4** we examine the optical properties of the laser formed structures. We study the effect of laser and reactive gas parameters, as well as thermal annealing, on the optical absorptance of the Si structures. We find increased absorptance which can reach up to more than 90% for UV to NIR wavelengths. The behavior observed is interpreted with respect to the morphology and composition of the samples.

In **Chapter 5** we examine the field emission properties of the laser formed structures in continuous areas and spot array geometries. The effect of laser pulse duration is extensively studied in order to identify the optimum processing conditions for inducing low-threshold field-electron emission in each case. Furthermore, we demonstrate the possibility of fabricating Si spike emitters for practical applications, such as cold emission arrays through a fast and efficient maskless process.

In **Chapter 6** we investigate the wetting response of structured Si surfaces. We find that the initially hydrophilic surface becomes hydrophobic upon laser structuring, and use morphology gradients in order to induce spontaneous motion of liquids. By implementing an additional step to the laser structuring process, which is related to the deposition of chloroalkylsilane monolayers, we are able to fabricate superhydrophobic-highly water repellent surfaces and compare their properties to the lotus leaf. Finally, we demonstrate the possibility of dynamically tuning the wetting response of laser structured Si surfaces by means of electrowetting-on-dielectric and chemically induced wetting.

Chapter 1

Laser Induced Conical Si Microstructures

1.1 Introduction

The interaction of laser irradiation with materials has been of scientific and technological interest since the development of the first lasers. ^[1] Absorption of laser irradiation by a solid can lead to a permanent modification of its surface, causing melting and resolidification, vaporization, or ablation of the material. Laser processing of solids, using both continuous and pulsed lasers, has been studied over the years for different classes of materials including metals, ^[2,3] semiconductors ^[4,5] and dielectrics. ^[6]

Today abrasive laser machining (e.g. drilling, cutting, trimming), laser induced morphological, structural and compositional transformations of material surfaces (e.g. annealing, glazing) and processing applications that involve an overall change in the chemical composition of the surface (e.g. cladding), are extensively used for modifying the properties of materials.

In this chapter, we review the fundamental laser-solid interactions and discuss the resulting phenomena from a microscopic point of view. Furthermore, we introduce the proposed mechanisms underlying the spontaneous formation of periodic structures on the surfaces of materials upon laser irradiation in reactive gas ambients. A brief review on the

recent progress in laser induced surface structuring of Si is presented at the end of this chapter.

1.2 Laser-Solid Interactions: Fundamental Aspects

The interpretation of the basic interaction mechanisms between the intense light of a laser beam and matter, is an aspect of most interest.^[2] Laser light and material interaction mechanisms are strongly dependent on the laser beam parameters (i.e. wavelength, pulse duration, intensity, spatial and temporal coherence, polarization etc.), the physical and chemical properties of the material employed (absorption coefficient, thermal diffusion, heat of vaporization etc.), as well as on the environmental conditions (vacuum, reactive or non-reactive surrounding medium). In this section we focus on the fundamental primary and secondary processes that take place upon the interaction of laser pulses with semiconductors.

1.2.1 Primary Processes

The first step in any structural modification of any material by laser irradiation is the deposition of a certain amount of laser energy. The total laser energy and the spatial and temporal energy distribution determine the kind of final modification that will be obtained.^[7] The initial interaction of laser pulses with a semiconducting material is the excitation of electrons; upon photon absorption electrons are excited from their equilibrium states into higher-lying unoccupied states. Optical excitation in a semiconductor solid is described by four basic processes as illustrated in Figure 1.1.

The electrons can undergo interband transitions by **(a)** single-photon excitation, **(b)** multi-photon excitation, **(c)** intraband transitions by free-carrier excitation, or finally **(d)** impact ionization. Single-photon band-to band excitation is the primary process whereas the multi-photon excitation becomes increasingly significant with laser intensity, where the probability of nonlinear absorption is accordingly increased.^[7]

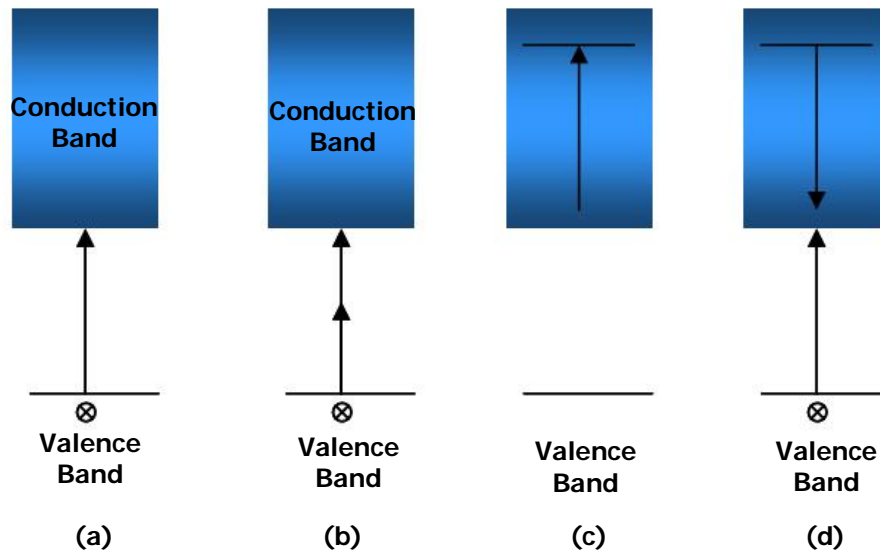


Figure 1.1 : Schematic of electronic excitation in a semiconductor by laser pulses: (a) single-photon excitation, (b) multi-photon excitation, (c) free carrier-absorption, (d) impact ionization

Free-carrier excitation refers to the linear absorption of several photons by a conduction band electron, sequentially moving to higher states in the conduction band Figure 1.1(c). If the carrier density in the conduction band is sufficient, some free carriers can acquire enough energy to create additional conduction band electrons by impact ionization [Figure 1.1 (d)]. A highly excited electron in the conduction band (higher than the band gap energy) relaxes by releasing part of its energy through promoting another electron from the valence band to the conduction band. This process increases the number of free carriers in the conduction band. If the laser intensity is high enough, multi-photon absorption and impact ionization can lead to optical breakdown, which produces a plasma.^[8]

1.2.2 Secondary Processes

The initial electronic excitation is followed by a complex hierarchy of secondary processes. The excited electrons relax and the deposited energy is redistributed through a number of processes which eventually end in the structural modification of the material. The time scales of this chain of events can be crudely classified^[7] as shown in **Figure 1.2**

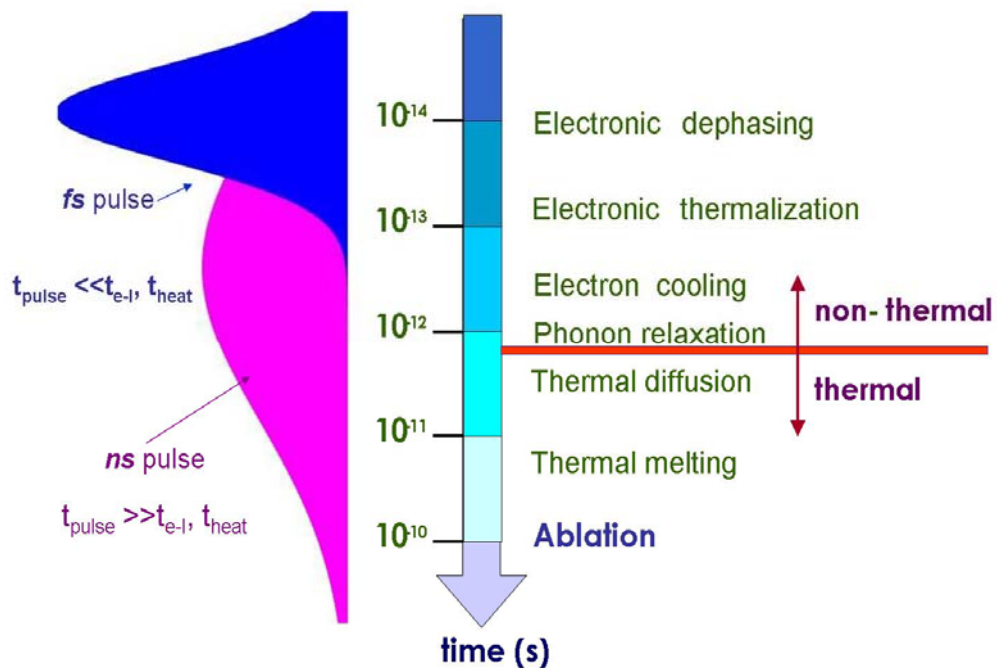


Figure 1.2 : Timescales of the various secondary processes- in comparison to the pulse duration at FWHM in the case of ns and fs pulses.

The primary electronic excitation is associated with very short-lived coherent polarization of the material. Dephasing processes destroy the polarization roughly on a time scale of about 10^{-14} sec.^[9] The initial distribution of excited electronic states is rapidly changed by carrier-carrier interaction processes, and a quasi-equilibrium situation is established among the electrons on a time scale of about 10^{-13} sec. The quasi-equilibrium electrons cool down on a timescale of 10^{-13} to 10^{-12} sec by emission of phonons (carrier-phonon scattering).

The final stage of the thermalization process is the redistribution of the phonons over the entire Brillouin zone according to a Bose-Einstein distribution. At this point the temperature of the laser excited material can be defined, and the energy distribution is characterized by the temperature. Subsequent processes are of thermal nature. After phonon relaxation and phonon redistribution, the diffusion of heat from the surface to the bulk, follows on the time scale of 10^{-11} s. If the laser pulse intensity exceeds the melting threshold, melting occurs. Finally, thermal ablation takes place on a timescale of 10^{-10} s.

There is a distinct dividing line at about 10^{-12} s defining the regime between non-thermal and thermal processes. Mechanisms leading to structural modifications using picosecond and longer laser pulses are in most cases thermal, i.e., they take place on timescales longer than a picosecond. On the other hand, employment of ultrashort (femtosecond) pulses leads to a different kind of modification. As illustrated in **Figure 1.2**, when the pulse duration is significantly less than electron-to-lattice (ions) energy transfer time (and subsequently to the heat conduction time), non-thermal pathways may be accessed that take place on a timescale shorter than a picosecond, hence before thermal processes kick in. However, there are still several aspects of femtosecond laser induced modification of solids yet to be interpreted.

1.3 Laser Induced Periodic Surface Structures

Laser-Induced Periodic Surface Structures (LIPSS)^[5] is a form of laser induced surface modification which appears to be spatially periodic in nature, and which occurs on a wide variety of both opaque and transparent materials. Birnbaum^[10] was the first to report these grating-like morphologies on the surfaces of several semiconducting materials, which were used as Q-switching elements in a pulsed ruby-laser system. Since then, similar patterns have been produced in semiconductors,^[11,12] metals,^[13,14] and dielectrics^[15,16] with the use of both continuous and pulsed laser sources. The common morphological characteristics found in all these materials^[17] have led to the conclusion that the formation of laser-induced periodic surface structures by a single laser beam is a universal phenomenon that can appear on any material absorbing radiation, regardless of its dielectric constant.^[4]

Structures that develop on solid surfaces under the action of laser light can be classified into coherent and non-coherent ones.^[18] Coherent structures are directly related to the coherence, the wavelength and the polarization of the laser light. These structures have a common origin: the oscillating radiation field on the material surface, which is generated by the interference between the incident laser beam and scattered/excited surface waves. The spatial periods of such structures are therefore proportional to the

laser wavelength, while their orientation is perpendicular to the electric vector of the incident light. Non-coherent structures however, are not directly related to any spatial periodicity of the energy input caused by interference phenomena; their period is related to the laser-beam intensity and the ambient gas pressure, when such is used,^[18] rather than the laser wavelength and polarization. They appear at higher intensities as compared to coherent structures, and they exhibit a wave-like topography with a spatial period much larger than the incident laser wavelength.^[19] The formation of these periodic structures has been related to capillary waves.^[20]

Capillary wave excitation is believed to be responsible for the formation of an initial wave-like pattern on the Si surface in our experiments, following laser irradiation in a reactive gas ambient. This pattern acts as a precursor to the development of the Si microstructures. Subsequent laser induced preferential material removal as well as chemical etching of the Si surface (by the reactive gas), promote conical feature formation on the Si surface. Since the formation of the Si structures is governed by the simultaneous action of complex surface deformation mechanisms, their exact role and relative contribution is not easy to identify. In the following sections we review on the basic characteristics of each process, by treating them separately.

1.3.1 Capillary Waves

Surface melting under the action of laser light may result in the excitation of convective fluxes within the liquid layer. Such convective fluxes play an important role in material transport in laser processing. With uniform laser light irradiation and intensities that do not cause significant evaporation, convection may originate either from changes in material density related to temperature gradients in the z-direction or from surface tension effects.^[18] In laser processing the latter is usually dominant, because the molten layer depth, h_l , is smaller than the capillary length (l_c), i.e., $h_l < l_c = (\sigma/\rho g)^{1/2}$ where σ is the surface-tension coefficient of the air/liquid interface, ρ is the density of the liquid and g is the gravitational acceleration.^[1]

^[1] For molten Si, a typical value of l_c is a few mm.

In other words, if the above condition is met at laser fluences close to the material melting threshold, the dominant restoring force is provided by surface tension, and capillary waves can be excited at the air/liquid-material interface. If the decay of the capillary wave activity is not complete by the time the surface resolidifies, a permanent record of the wave-like structures is “frozen” onto the surface. [4]

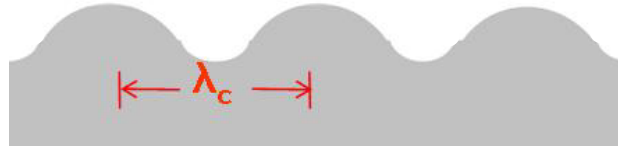


Figure 1.3 : Capillary waves excited on a material surface. λ_c is the wavelength of the capillary waves.

The dispersion of the natural oscillation frequency ω_c for shallow capillary waves is given by the following expression. [21]

$$\omega_c = \left(\frac{\sigma \cdot h}{\rho} \right)^{1/2} \cdot \kappa_c^2 \quad (\text{Eq. 1.1})$$

where h is the thickness of the liquid and κ_c is the wave vector of the surface perturbation while

$$\kappa_c = 2\pi/\lambda_c, \quad (\text{Eq. 1.2})$$

where λ_c is the wavelength of the capillary wave.

Alternatively the wavelength of the capillary wave is given by:

$$\lambda_c = \left[\frac{\sigma \cdot h}{\rho} \right]^{1/4} \cdot (2 \cdot \pi \cdot \tau_c)^{1/2} \quad (\text{Eq. 1.3})$$

where τ_c is the period of the capillary wave.

Capillary waves are damped by viscous dissipation within the bulk liquid. [22] The viscous forces cause the amplitude A of the capillary waves to decay as:

$$A \sim e^{-\gamma t}, \quad (\text{Eq. 1.4})$$

where

$$\gamma = (2\eta/\rho)\kappa^2 = 2\nu\kappa^2. \quad (\text{Eq. 1.5})$$

with, η being the shear viscosity and ν the kinematic viscosity of the liquid. ^[4]

1.3.2 Preferential material removal

Growth of high-roughness conical surface structures from the initial wave-like pattern has been interpreted on the basis of preferential material removal, as a result of further laser interaction with the solid. The formation of microstructures is possible, owing to the increase of reflectivity of the surface with the increase of the incident angle. ^[23,24] This results in material removal mostly in those areas of the target material that are oriented normally to the laser beam axis. This variation of the reflectivity provides the preservation of roughness at laser fluence close to the threshold of melting.

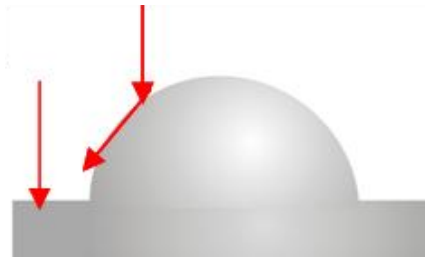


Figure 1.4 : Schematic of light reflection off a protrusion leading to enhanced light absorption in the intercone areas.

Moreover the laser irradiation reflected from the cone slopes can lead to light entrapment in between the high roughness areas, where the local laser fluence is sequentially increased (**Figure 1.4**).

1.3.3 Laser Induced Chemical Etching

Laser chemical processing of materials is a means of material modification, inducing either an overall change in the chemical composition of the material or the activation of a real chemical reaction. ^[18] Alternatively, photochemical etching of semiconductors is based on the interaction between radicals and carriers within the

semiconductor surface. Radicals can be formed spontaneously by molecule-surface interactions, by selective electronic excitation, or by vibrational excitation of the etchant.

The photochemical etch rates sequentially depend on the concentration of the active species within the ambient medium, on the optical penetration depth of the laser light in the semiconductor surface, carrier lifetimes, recombination processes etc. One of the most extensively used gases for etching of semiconductors, and in particular Si with which it is very active, is SF₆.

At room temperature SF₆ is stable and does not chemisorb on Si. However heating at approximately 1000 °C may initiate a thermal reaction. This suggests that laser heating could cause a reaction. SF₆ can be physisorbed at 90K or for P ≥ 1Torr at room temperature.^[18] The dissociation of SF₆ leading to the formation of fluorine radicals is well known in plasma etching applications.^[25,26] Etching of Si can then occur through the formation of these F radicals, which eventually react with Si to form volatile Si containing fluorine compounds.

Laser induced etching of Si with SF₆ can take place via a vibrationally or electronically excited molecule, or a radical created by photodissociation. The course of the latter interaction has been studied using CO₂ laser pulses in the presence of SF₆ at normal incidence to the Si substrate. It has been suggested that gaseous or physisorbed SF₆ molecules are excited into higher vibrational states via coherent multiphoton excitation. In contrast to ground-state SF₆, vibrationally excited SF₆ can dissociatively chemisorb on Si surfaces resulting to the formation of fluorine ions. Part of the chemisorbed F⁻ ions penetrate into the Si forming a fluorosilyl layer. Via a number of subsequent processes SiF₄ is formed and desorbs from the surface.^[29]

With high fluences and parallel incidence of the CO₂ irradiation, decomposition of SF₆ may occur due to coherent and multiphoton absorption (via the vibrational state ladder) resulting in its dissociation.²⁷ SF₆ molecules decompose into SF₅ and F atoms. SF₅ (being very unstable) decomposes into SF₄ and another F atom, which both diffuse into the Si surface and react to form SiF₄. Gas-phase photodissociation of SF₆ producing fluorine radicals has also been demonstrated for intense femtosecond irradiation at 800 nm.^[28] Finally, Lowndes et al^[29] have suggested that fluoride compounds such as SiF₂

and SiF₄, which are volatile at the transient temperatures reached during laser heating, can be formed under irradiation of Si with a KrF ($\lambda=248$ nm, $\tau=25$ ns) excimer laser.

1.4 Surface Structuring of Si with Lasers

The formation of conical structures on the Si surface has been examined over the past few years, by using several different laser sources ^[24,29-38] in various ambients. The dynamics of the formation of these structures on Si with ns laser irradiation were first systematically studied by Sanchez et al.,^[30,31] by using an ArF laser (193nm, 23ns). Lowndes et al. ^[29,32,33] subsequently studied the early stages of the structure formation in air and in SF₆ with the use of a KrF (248 nm, 25 ns) excimer laser. In 2000, Evtukh et al.^[34] demonstrated first the possibility of using of structured Si as a field emitter, but with high turn-on fields. In that work a Nd:YAG (1.06 μ m, 0.2ms) laser system was used and structuring took place in air. Later Shafeev et al.^[35,36] used a Cu vapor laser (510.6nm, 20ns) for irradiation of Si in the same atmosphere, to demonstrate the possibility of low-threshold field electron emission from the structures obtained.

Extensive work on the formation of laser structured Si has been performed by Mazur and co-workers ^[37,38]. Using a Ti:Sapphire laser (800 nm, 100 fs) in different ambients (vacuum, Cl₂, SF₆) they systematically studied the morphology, structure and composition of the resulting structures. They were also the first to report the possibility of using laser microstructuring for increasing the optical absorptance of Si, throughout a wide spectral range.^[24,44] Recently they investigated also the possibility of improving the wetting properties of structured Si by coating them with fluoroalkylsilane monolayers.^[39]

In the present work, we pursue these studies further and identify the optimal laser and reactive gas parameters for tailoring the optical, electronic and wetting properties of laser structured Si. More specifically:

a) Morphological, structural and compositional studies / Replication

The laser pulse duration is a critical parameter which is expected to influence the quality of the obtained structures. This is due to the differences in the laser-matter

interaction mechanisms for different pulse duration.^[18] In this work, we study the effect of laser pulse duration on the morphology, structure and composition of textured Si surfaces by using a KrF laser capable of emitting pulses at 248 nm of 15 ns, 5 ps and 500 fs. This allows the optimization of the laser parameters involved for a given ambient atmosphere through the interplay of laser fluence, number of pulses and pulse duration. Furthermore, a high repetition rate, high-power Nd:YVO₄ (1064nm, 12ps) laser system is used for the fast fabrication of Si structures over extended areas. The resulting morphologies are subsequently used for replication purposes, allowing the initial Si surface pattern to be transferred on other materials as well.

b) Optimization of Properties

i) Optical absorptance

The optical absorptance of structures fabricated using different laser sources (248 nm, 15ns; 5ps), (1064 nm, 12 ps) and gas parameters (vacuum, 50-500 Torr SF₆) is studied. The phenomena observed are interpreted with regard to the morphological, structural and chemical changes the surface undergoes upon laser treatment.

ii) Field emission properties

The field emission properties of structures fabricated using UV laser pulses of the same wavelength 248 nm at 15ns, 5ps, 500 fs are also studied. Furthermore, the field emission properties of continuous areas of microstructures are directly compared to spot array geometries, both fabricated using the Ti:Sapphire laser system (800 nm, 180 fs). In all cases, the observed field emission properties are correlated to localized field enhancement originating from the geometry of the structures.

iii) Wetting properties

The wetting properties of laser structured Si are extensively studied by using a Ti:Sapphire laser (800nm, 180 fs) system. We study the static and dynamic behaviour of water droplets on Si surfaces without any additional coating. In addition, we attempt to combine different surface morphologies for inducing spontaneous

motion of liquids. Furthermore, through the additional step of depositing chloroalkylsilane monolayer on the structured surfaces, we study their static and dynamic wetting response and directly correlate them to the “model” superhydrophobic natural surface of the sacred lotus leaf (*Nelumbo-Nucifera*). Finally, we introduce two alternative ways to manipulate the behaviour of liquids in contact with these surfaces; electrowetting and chemically induced wetting.

Chapter 2

Experimental Methods

2.1 Introduction

This chapter includes a description of the laser sources and the experimental apparatus employed for surface structuring of Si. Also a description of the systems used for measuring the optical absorptance and field emission, as well as the instrumentation implemented for the characterization of the wetting response of the structured Si samples, is given.

2.2 Laser Sources

The laser sources employed for surface micro/nano structuring of Si were:

- A distributed-feedback dye-laser based KrF excimer laser system ($\lambda=248nm$, $\tau_{FWHM}=500fs; 5ps; 15ns$)
- A regenerative amplified Ti:Sapphire laser system ($\lambda=800nm$, $\tau_{FWHM}=180fs$)
- A diode pumped mode locked Nd:YVO₄ laser ($\lambda=1064nm$, $\tau_{FWHM}=12ps$)

2.2.1 The KrF excimer laser system

This laser system can operate either as a conventional KrF excimer laser emitting pulses of 15 ns duration, or produce pulses of 5 ps or 500 fs duration through distributed feedback amplification. Femtosecond laser pulses are obtained from a hybrid excimer-dye laser system through a complicated arrangement.^[40,41] The output of a double-cavity excimer laser (Lambda Physik EMG 150MSC) excimer laser (at 308 nm) is used as a pump laser for a special femtosecond dye laser amplifier system, and as an amplifier (at 248 nm) for the frequency-doubled output pulses of the dye laser set-up. Part of the output of the XeCl laser is used to pump a Distributed Feedback Dye Laser (DFDL), which in turn generates the pumping laser beam for the KrF laser cavity. This pump source consists of two dye lasers, two amplifier stages and a gated saturable absorber (GSA) placed between the amplifiers. The resulting output pulse has a duration of a few ps, while being centred at 365 nm, and is used for pumping the DFDL which allows the generation of short, femtosecond pulses from a seeding pulse of longer duration. The output wavelength of the DFDL is set to twice the KrF wavelength (496 nm), and is sequentially amplified via a two-stage amplifier, separated by a saturable absorber and

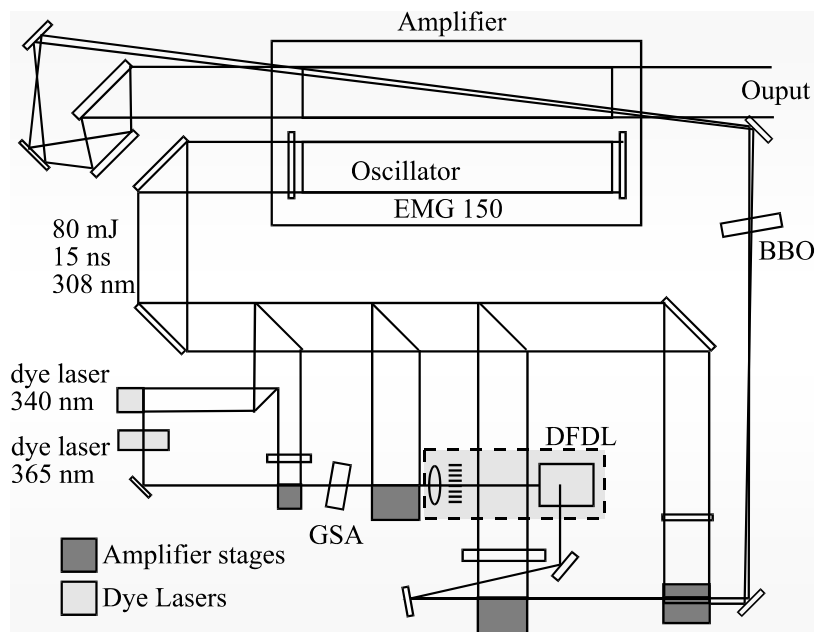


Figure 2.1: Schematic of the set-up of the fs excimer laser

frequency doubled by a Beta-Barium Borate (BBO) crystal to yield picosecond seeding pulses of 248 nm wavelength. This seeding pulse is amplified through a KrF excimer laser, via a double pass arrangement shown in **Figure 2.1**, yielding pulse energies up to 10 mJ with pulse length of 500 fs. 5 ps laser pulses can also be generated by insertion of a multiple reflection etalon in the dye laser set-up.

2.2.2 The Ti:Sapphire laser system

This laser system is based on a Spectra Physics Tsunami oscillator, which delivers 80-100 fs pulses at a repetition rate of 81 MHz with a power of 500 to 600 mW and a FWHM of 10 nm. The pump laser used for this system is a Spectra Physics Millennia Nd:YLF, which pumps the oscillator with a power of 5 W. A Thales Laser System (stretcher, amplifier, compressor) amplifies the beam by using another Ti:Sapphire crystal and a 12 W Q-switched Nd:YLF pump laser (B. M. Industries). During the chirped pulse amplification the repetition frequency is lowered from 81 MHz to 1 kHz by a pulse picker (pockels cell) inside the cavity of the amplifier. After being amplified the pulse is linearly polarized, it has a length of 180 fs with a repetition rate of 1 kHz and a power of 500 to 600 mW, respectively.

2.2.3 The Nd:YVO₄ laser system

This infrared picosecond laser system (STACCATO from Lumera) consists of a diode pumped mode locked Nd:YVO₄ laser, a pulse picker and a regenerative diode pumped amplifier. Linearly polarized laser pulses with a wavelength of 1064 nm at a fixed repetition rate of 50 kHz can be delivered with this system. The pulse duration is 12 ps at full width at half maximum, and the pulse energies can be adjusted up to 110 μ J, corresponding to an average power of up to 5.5 W.

2.3 Experimental Setup

Si microstructuring took place in a vacuum chamber (**Figure 2.2**) evacuated down to a residual pressure of $\sim 10^{-2}$ mbar by means of a rotary pump (Alcatel). The background pressure was measured using a pirani gauge. A micro valve system attached to the chamber enabled a precise backfilling of a halogen-containing ambient gas (SF_6). The pressure of the backfilling gas was measured with a baratron gauge (MKS Instruments).

In most cases, the laser beam was shaped by an iris and was focused with a quartz lens on the sample, mounted to a sample holder inside the vacuum processing chamber. The laser fluence was varied by using filters or attenuators. The laser beam entered the chamber through a quartz entrance window, while the irradiation process could be monitored through a plexiglas window, which was laterally mounted on the vacuum chamber.

Minor variations and adjustments were made on the experimental setup to meet the specific requirements of each laser system, regarding the optical configuration, means of laser triggering and scanning method, as follows.

- **Ti:Sapphire laser system**

The processing chamber was placed on a computer driven high precision X-Y translation stage (Standa) with spatial resolution of 1 μm allowing sample displacement with regard to the laser beam up to 100 mm [**Figure 2.2(a)**]. This system allowed control over the amount of overlap between consecutive scans when large area microstructuring was required. For this laser system operating at a repetition rate of 1 kHz, direct triggering from the laser was not possible, and so a mechanical shutter (Uniblitz) was synchronized to the computer driven translation stages, allowing to direct laser pulse packages into the processing chamber.

- **KrF laser system**

The scanning system described in the previous paragraph was used for this laser system as well. In this case however, the number of incoming pulses as well as the delay between

subsequent pulses was determined by synchronizing the laser to the computer controlled translation stages.

- **Nd:YVO₄ laser system**

With this system, instead of rastering the sample over the laser beam as previously shown, the laser beam was scanned across the sample [Figure 2.2(b)]. This was achieved by means of a computer controlled galvo-scanner from Scanlab with a maximum speed of 1 m/sec and a spatial resolution of 1 μm . In order to avoid distortions of the beam due to scanning through the focussing optic, an 80 mm f-theta objective was used.

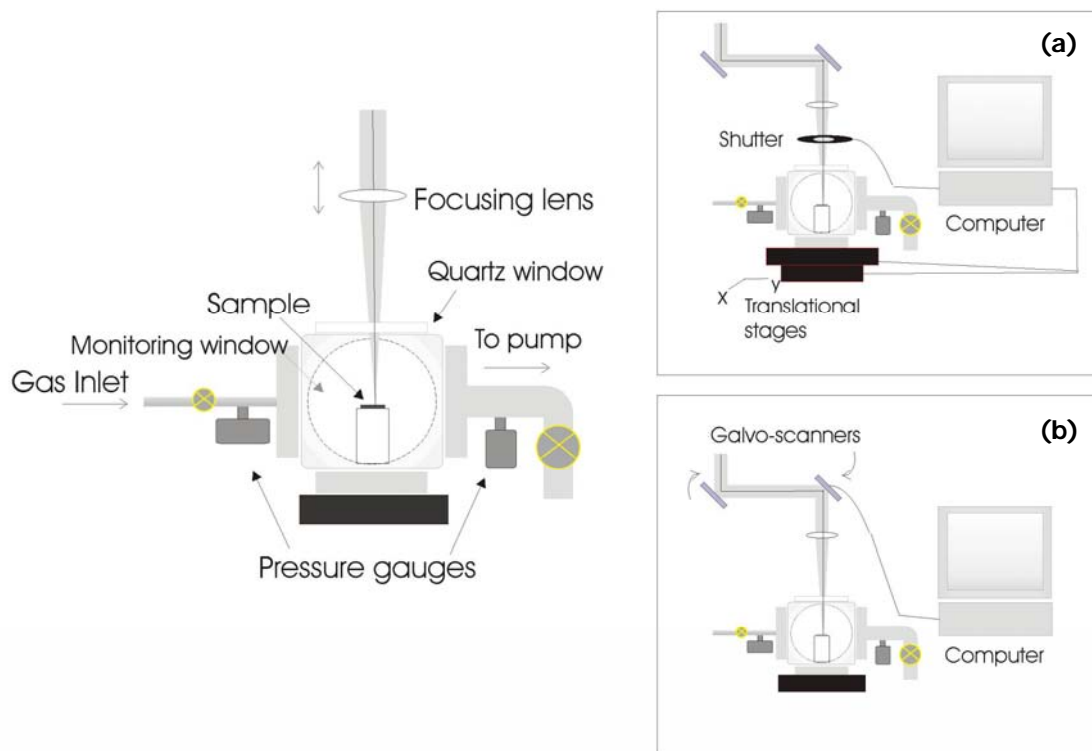


Figure 2.2: The experimental set-up used for structuring of Si

2.4 Sample Preparation

The samples used for producing the Si microstructures were 10mm x 10mm squares cut from 3- or 4- inch commercial single crystal (Siltronix). Depending on the properties tested, the samples used were n-type (phosphorous-doped) Si (100) wafers with a

resistivity of either 2-8 Ohm·cm or 50-100 Ohm·cm respectively, and a thickness of 400-450 μm. The samples were cleaned in an ultrasonic acetone bath prior to irradiation, followed by isopropanol and deionized water baths. In order to remove part of the oxide grown on the structured Si surface during the irradiation process, the samples were dipped in a 10% HF aqueous solution and subsequently rinsed with copious amounts of water.

▪ **Silanization procedure**

In the cases where silanization was required, the samples were placed in a flask containing 0.5 ml of dimethyldichlorosilane ((CH₃)₂SiCl₂, DMDCS) reagent. Hydrophobic DMDCS monolayers were subsequently deposited on the sample's surface through adsorption reactions. The vapor-phase reactions were carried out overnight at room temperature. The hydrophobized wafers were rinsed with toluene (two aliquots), ethanol (three aliquots), 1:1 ethanol/water (two aliquots), deionized water (two aliquots), ethanol (two aliquots), and deionized water (three aliquots) and were finally dried in a clean oven at 120 °C for 30 min.^[42]

2.5 Sample Characterization

2.5.1 Morphological, structural and compositional analysis

The structured Si samples were characterized morphologically using a JEOL JSM-840 or a CamScan Series No.2 Scanning Electron Microscope (SEM). An image processing algorithm (Media cybernetics-Image Pro Plus) was utilized in order to obtain quantitative information concerning the macroscopic characteristics of the structures that were formed, i.e. spike density, height, cone tip radius and distribution, from top and side-view SEM pictures of the structured areas.

Transmission Electron Microscopy (TEM), High Resolution Electron Microscopy (HRTEM), Electron Energy Loss Spectroscopy (EELS) and Selected Area Electron Diffraction (SAED) were implemented in order to determine the fabricated cones',

structure and crystallinity, using an FEI CM20 TEM equipped with a Gatan GIF200 energy filter. Their composition was determined by means of Energy Dispersive X-ray Spectroscopy (EDS). The cross-section samples for TEM observations were prepared by mechanical grinding followed by dimpling and finally ion beam milling at a liquid nitrogen cooled stage.

Intermittent contact-atomic force microscopy (AFM-Nanoscope IIIA) was utilized in order to characterize the quality of the silane coatings, when used, on the flat part of the Si samples outside of the irradiating regions. The corresponding rms roughness was determined by an image processing algorithm.

Finally, a Rudolph Instruments (series 439) manual ellipsometer operating at 632 nm was used, in order to quantify the thickness of the silane layers as well as the silicon oxide layers grown on the unstructured part of the samples, in some of the wetting experiments.

2.5.2 Optical absorptance measurements

The optical absorptance of a sample can be determined through reflectance and transmittance measurements, with the use of a spectrophotometer. However, measuring the optical properties of rough surfaces may sometimes be difficult because of scattering, which enhances the diffusive component of the reflectance and transmittance. A common way to measure reflectance and transmittance from strongly scattering materials is to use an integrating sphere; a hollow sphere coated internally with a matte finish, diffusing type material. In this way the light that enters the sphere can be scattered uniformly around its interior through multiple reflections, before it is detected.

The absorptance ($A = 1 - R - T$) of the structured and unstructured Si surfaces was determined by reflectance (specular and diffuse) and transmittance (direct and scattered) measurements. The measurements were performed using a UV/VIS/IR spectrophotometer equipped with an integrating sphere (PerkinElmer Lambda-950). An all-reflecting, double monochromator optical system was used, for the UV/Vis and NIR range. The two radiation sources, a deuterium lamp and a halogen lamp covered the

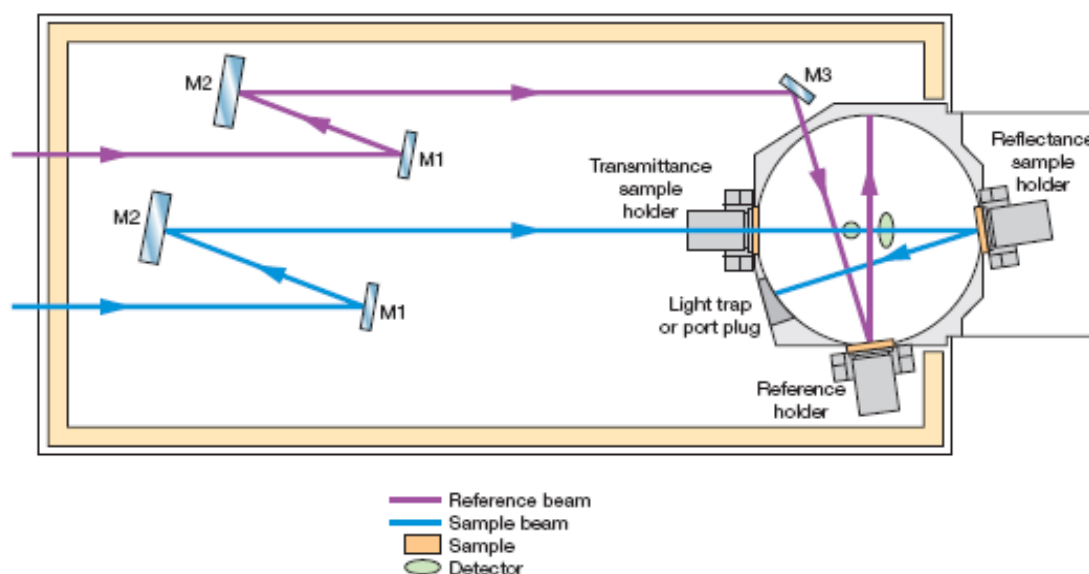


Figure 2.3: The optical design of the spectrophotometer equipped with an integrating sphere

working range of the spectrometer (**Figure 2.3**). The beam diameter on the sample surface was $\sim 0.3 \times 0.3 \text{ cm}^2$.

The interior of the integrating sphere was constructed of Spectralon, a material which exhibits high diffuse reflectance across the 250-2500 nm wavelength range. The transmitted and reflected light was detected by a UV/Vis detector (R955 photomultiplier tube (PMT)) and a NIR lead sulphide (PbS) photocell detector mounted inside the integrating sphere.

2.5.3 Field emission measurements

The experimental apparatus used for measuring the field emission properties of laser structured samples is shown in **Figure 2.4**. The samples were tested under vacuum ($<10^{-5}$ Torr), as cold cathode field emitters in a, short-circuit protected, planar diode system. Each sample was used as the cathode and the emitted electrons were collected on a CuSn anode. The distance was always set at least three times the height of

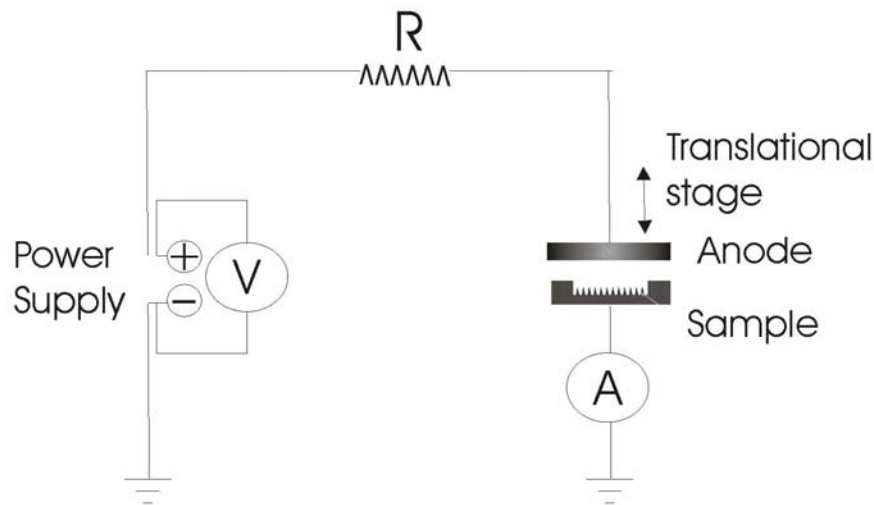


Figure 2.4: Apparatus used to measure field emission from structured Si

the highest observable spike of each sample to ensure that the emission field was not influenced by the anode location.^[43] The distance between the anode and the cathode was determined with a 10 μm resolution, using a translational stage. A voltage was applied between the anode and the cathode ((SRS-PS350) power supply, 5000V max) to extract the electrons out of the microspikes. A current-limiting resistance of $R= 41 \text{ M}\Omega$, was placed after the power supply, in order to protect the circuit and the sample from possible damage. The emitted current was recorded during the increase and decrease of the applied voltage using a Keithley 617 Electrometer.

2.5.4 Wetting properties

▪ Static and dynamic behaviour of liquid drops

The experimental setup shown in **Figure 2.5** was used for the static contact angle measurements and dynamic measurements, with minor adjustments to meet the requirements of each specific experiment.

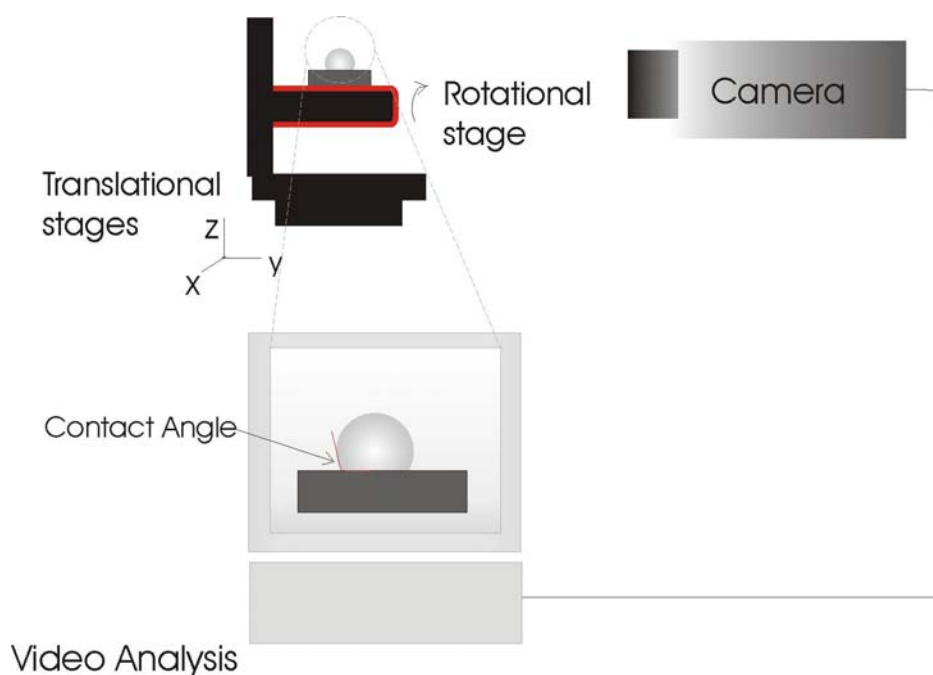


Figure 2.5: The experimental setup used for examining the static and dynamic behavior of liquids in contact with the structured surfaces.

For the sessile drop static contact angles, an automated tensionmeter (Material Interface Associates Inc.) was used to determine the contact angle, based upon a collection of digital images of sessile drops. The liquid drop was gently deposited on the samples using a micro litre plunger-operated pipette (Transferpette-BRAND (1-10 μ l)).

A similar experimental setup was used for the determination of contact angle hysteresis, the sliding angle experiments, and the uphill motion demonstration. Inclination of the sample up to 30 deg could be achieved with the use of a rotational stage. A CCD camera (30 fps), vertically positioned recorded the profile of the drops either in digital images or videos, from which certain frames were captured. The contact angle formed in each case was determined through a best circle fit approximation (ImageJ). A best circle fit can be safely used to determine the contact angle formed at the liquid-solid interface in our case, since for small drop volumes, typically < 5 μ l, gravitational forces are negligible, and the drop is not significantly deformed. For the water repellence experiments, where high temporal resolution was required, a Photon Focus – Hurricane high speed camera with a special optical system for magnification replaced the typical CCD camera. In this way up to 1000 fps could be captured. For these

experiments the drop was not deposited on the surface, but was left to perform free fall from different heights.

- **Electrowetting setup**

The electrowetting experimental system is illustrated in **Figure 2.6**. Liquid drops with volumes of a few μl , were gently deposited on the samples (positioned on a xyz translational stage) using a micro-liter pipette. Applying an DC potential between the electrode underneath the sample and the platinum wire electrode, which was inserted into the liquid droplet, decreased the contact angle of the liquid droplet on the solid surface. In every case the diameter of the wire was much smaller than the diameter of the drop. The voltage was applied through a power supply (Kikusui electronics (0-350 V)). A

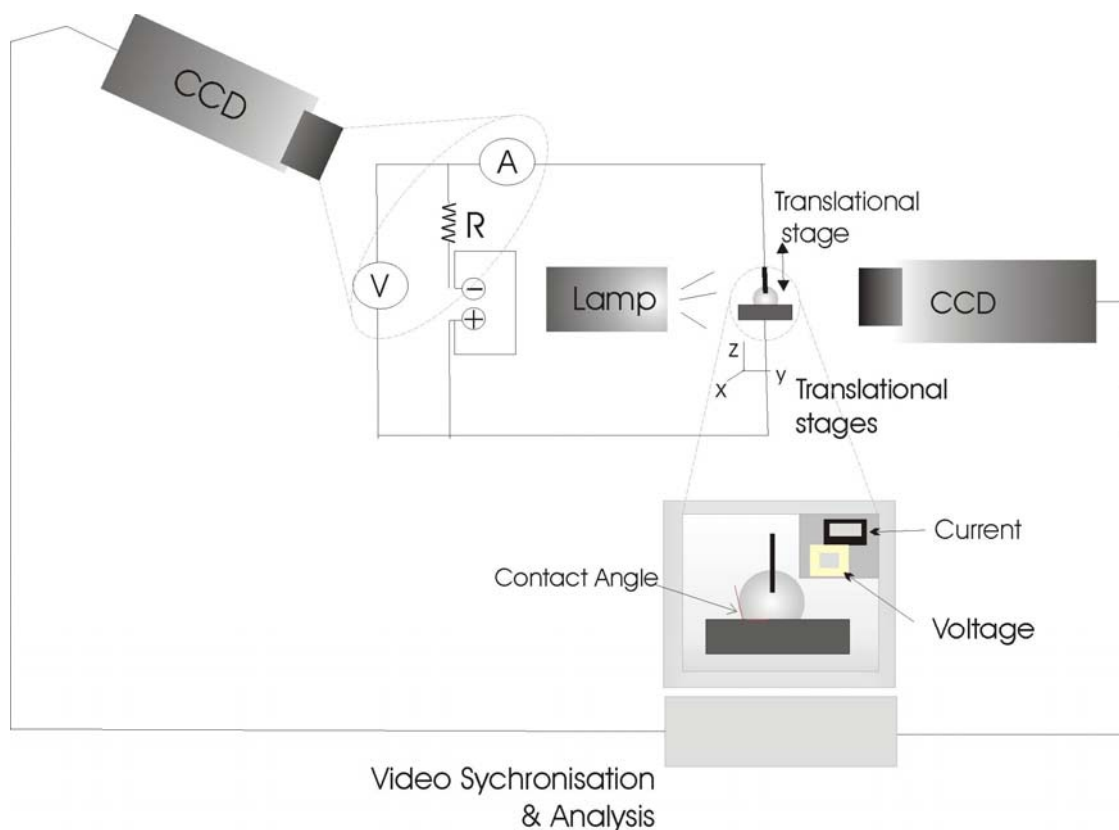


Figure 2.6: The setup used for the electrowetting experiments.

protection resistance ($R=100\text{ k}\Omega$) was placed in series with the power supply, and the current was recorded using a Keithley 485 electrometer.

A computer controlled CCD camera with an optical lens system for magnification positioned vertically with regard to the system, allowed monitoring of the change in the contact angle with time. A second CCD camera recorded simultaneously the changes in the applied voltage and the current fluctuations as a function of time. Video synchronization was used in order to perform the analysis, and extract the information on the contact angle change as a function of applied voltage and current. Then the contact angle for each frame was determined by using a best circle fit approximation.

- **Chemically induced wetting setup**

The experimental setup used for the chemically induced wetting is shown in **Figure 2.7**. A fixed volume organic solvent in liquid phase was injected into the bubbler with the help of a micro syringe through the inlet pipe of the bubbler. The bubbler was immersed inside a water tank for several minutes prior to the experiments, so as to achieve a stable and uniform temperature throughout the volume of the solvent in the bubbler. Due to the high vapour pressure of most of the organic solvents tested, vapour of the solvent can be easily formed at room temperature. However, the water tank-bubbler system was positioned on a heating plate, giving the ability to increase the temperature for the case when non-highly volatile liquids were tested. The organic solvent in vapour form was carried to the test chamber by the dry carrier gas N_2 at a fixed flow rate measured with a mass flow meter (Aalborg, GFM37). The flow range was 0-50 lt/min, with a 0.1 lt/min resolution. The process was initiated by opening the nozzle valve above the drop, after the flow of the vapour was stabilized.

The process was monitored with a computer controlled CCD camera (30 fps) through a magnifying lens assembly. The camera was positioned vertically with regard to the system, allowing monitoring of the change in the contact angle with time.

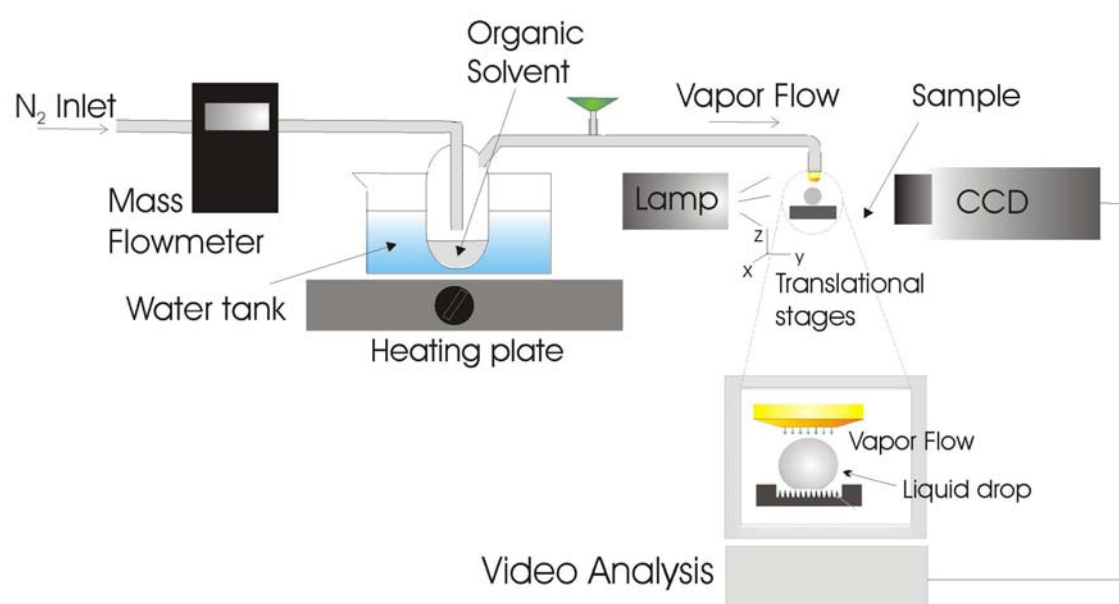


Figure 2.7: The experimental setup used for chemically induced wetting.

Chapter 3

Morphological / Structural Characterization and Replication

3.1 Introduction

In this chapter we examine the morphology, structure and composition of the patterned Si samples fabricated using different laser sources. The effect of laser parameters (e.g. laser fluence and average number of pulses), as well as the reactive gas pressure (SF_6), on the morphology of the structures obtained, is examined for each laser system. Furthermore, structural and compositional analysis of samples fabricated using different laser pulse durations at the same wavelength, is given. Through qualitative observations and phenomenological models we assess the proposed formation mechanisms and correlate them to our experimental findings. Finally, by using the Si features as “master” morphologies, we were able to successfully transfer the surface reliefs on PDMS (polydimethylsiloxane) and subsequently on the organic-inorganic hybrid material ORMOCER (ORganically MODified CERamic), via replica molding.

3.2 Morphological analysis

3.2.1 Experiments with the Ti:Sapphire fs laser system

In this section we study the formation of microstructures on the surface of Si, by using the Ti:Sapphire laser system ($\lambda=800$ nm, $\tau=180$ fs), operating at a repetition rate of 1 kHz. The effect of the laser processing parameters and the reactive gas (SF_6) pressure on the morphology and geometrical characteristics of the structures fabricated is investigated. For these experiments, an average number of pulses ranging from 100 to 3000, were tested for fluences varying from 0.20 to 2.32 J/cm² and for different reactive gas (SF_6) pressures ranging from 0 to 500 Torr.

Upon increasing laser fluence, conical microstructuring is promoted on the Si surface, with structures becoming more pronounced and spatially separated. SEM images of Si spikes fabricated in an SF_6 pressure of 500 Torr and 500 pulses under different fluences are shown in **Figure 3.1 (a-c)**. Under these conditions, no spikes were formed for fluences lower than 0.32 J/cm², while decreasing spikes density (tuned between 10⁶ and 10⁷ spikes/cm² [**Figure 3.2 (b)**]) was observed with increasing laser fluence.

An increase in the average spike height was observed with increasing number of laser pulses [**Figure 3.1 (d-f)**] or increasing laser fluence [**Figure 3.1 (a-c)**]. In this case the height of the cones ranged from a few to less than 20 μm [**Figure 3.2 (a)**]. Furthermore the presence of secondary tip decoration on the cone surfaces is promoted with increasing number of pulses or fluence.

The reactive gas also plays a distinct role in the spikes fabrication process, since it determines the sharpness of the structures obtained [**Figure 3.1 (g-i)** and **Figure 3.2 (a)**]. The Si structures fabricated in vacuum were blunt and irregular. However they became more pronounced with increasing ambient gas pressure (250-1250 Torr). Increasing reactive gas pressure, as laser fluence and number of pulses, acts favorably to the formation of second-lengthscale roughness on the surface of the cones.

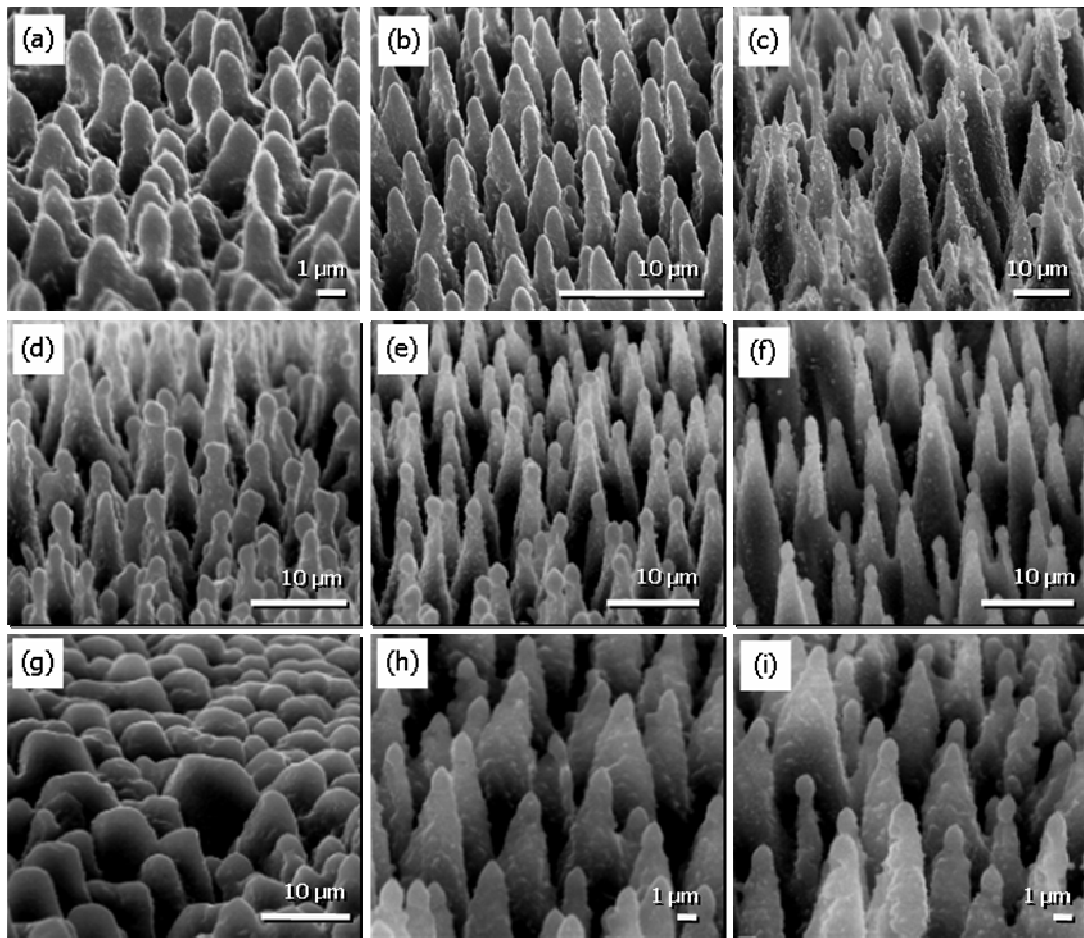


Figure 3.1 : Side SEM images of Si microstructures fabricated using the Ti:Sapphire laser source. **(a-c)** the laser fluence effect; irradiation in a 500 Torr SF₆ atmosphere, with an average of 500 pulses at a fluence of (a) 0.56 J/cm², (b) 0.78 J/cm², and (c) 1.5 J/cm². **(d-f)** the number of pulses effect; irradiation in a 500 T SF₆ atmosphere, at a laser fluence of 2.32 J/cm² with (d) 250 pulses, (e) 750 pulses and (f) 1500 pulses. **(g-i)** the reactive gas pressure effect; irradiation with 1000 pulses under a fluence of 1.2 J/cm² in (g) vacuum, (h) 500 Torr SF₆ and (i) 1250 Torr SF₆ atmosphere.

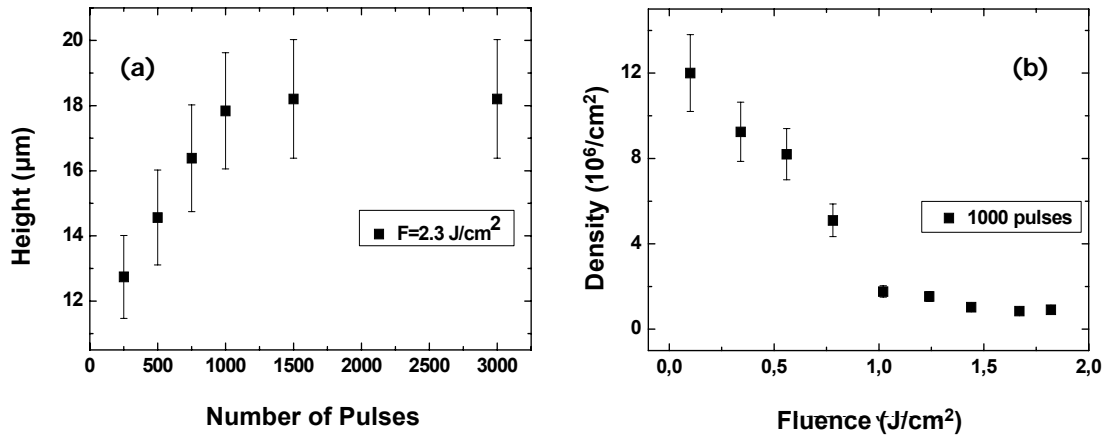


Figure 3.2 : Morphological characteristics of the spikes fabricated using the Ti:Sapphire laser source: (a) The spikes' height as a function of the number of laser pulses and (b) the spikes' density as a function of laser fluence.

3.2.2 Experiments with the Nd:YVO₄ ps laser system

Fabrication speed is an important aspect in laser materials processing, and in laser microstructuring the overall processing time is determined by the laser energy output, the laser repetition rate and the sample (or laser beam) scanning speed. For standard laser and scanning systems this can be a time consuming process.

In this section we utilize a high power, high repetition rate picosecond laser Nd:YVO₄ ps laser system ($\lambda=1064\text{nm}$, $\tau=12\text{ps}$) operating at a repetition rate of 50 kHz, for the fast fabrication of extended surface areas containing Si microstructures. The time to process a $5 \times 5 \text{ mm}^2$ area of each sample varied from 25 to 150 sec, depending on the average number of pulses required in each case, a decrease up to hundreds of times compared to the Ti:Sapphire laser system structuring process.

Structuring took place at different reactive gas pressures and irradiation parameters (average number of pulses and laser fluence). An average number of pulses ranging from 500 to 3000 were tested for fluences varying from 0.5 to 1.4 J/cm^2 and for different reactive gas (SF_6) pressures ranging from 0 to 500 Torr.

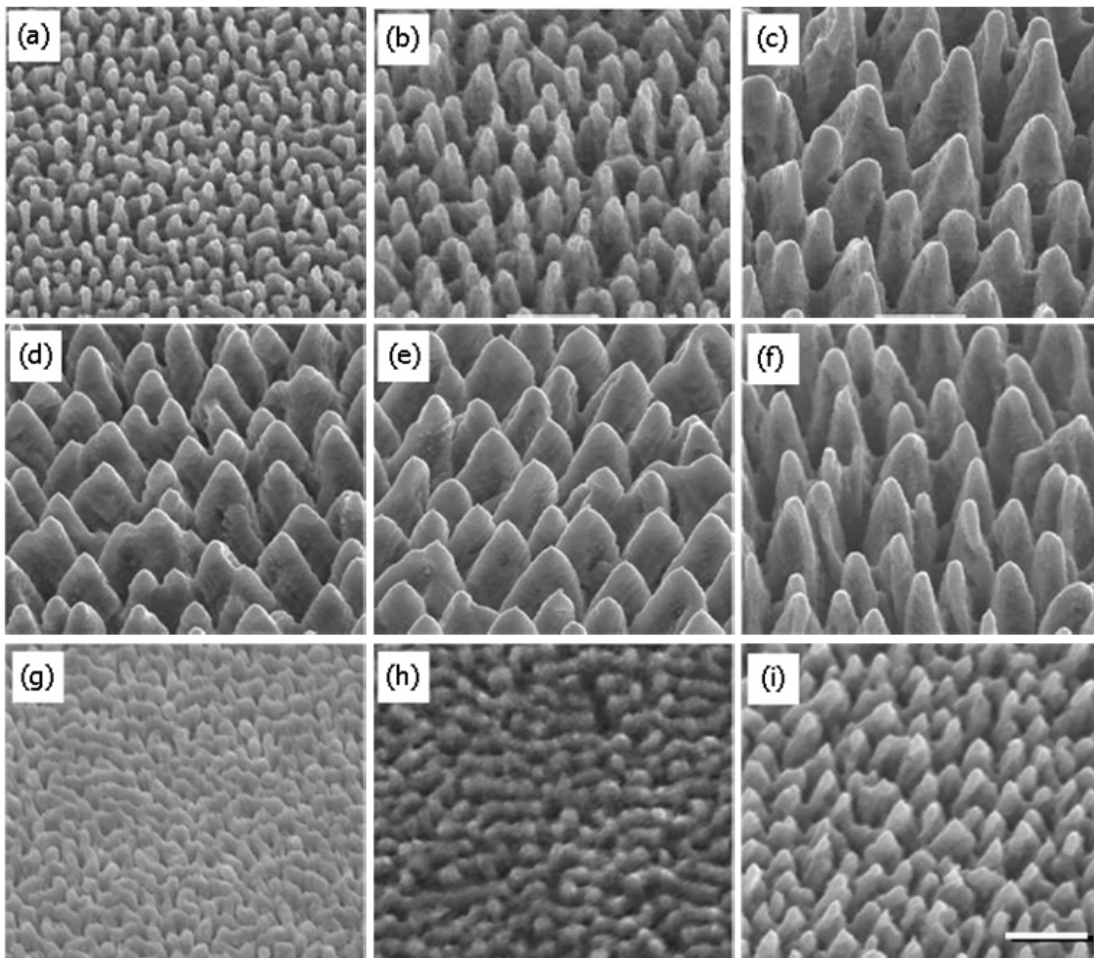


Figure 3.3 : Side SEM images of Si microstructures fabricated using the ps Nd:YVO₄ laser source (a-c) the laser fluence effect; irradiation in a 500 Torr SF₆ atmosphere, with an average of 1000 pulses at a fluence of (a) 0.5 J/cm² (b) 1.0 J/cm² and (c) 1.4 J/cm². (d-f) the number of pulses effect; irradiation in a 250 Torr SF₆ atmosphere, at a laser fluence of 1.4 J/cm² with (d) 500 pulses, (e) 715 pulses and (f) 1000 pulses. (g-i) the reactive gas pressure effect; irradiation with 1000 pulses under a fluence of 0.75 J/cm² in (g) vacuum, (h) 50 Torr SF₆ and (i) 500 Torr SF₆ atmosphere. The scale bar is 10 μm

Figure 3.3(a-c) shows SEM pictures of Si spikes fabricated at a SF₆ pressure of 500 Torr and with an average of 1000 pulses, under different fluences. Decreasing spikes density (tuned between 10⁶ and 10⁷ spikes/cm² (**Figure 3.4 (b)**) is observed with increasing laser fluence. We also find the average spike height to increase with increasing number of laser pulses [**Figure 3.3 (d-f)**] or increasing laser fluence [**Figure 3.3 (a-c)**], with their height ranging from 3.5 to more than 15 μm [**Figure 3.4 (a)**]. As, in the case

of the Ti:Sapphire irradiation source, the reactive gas is crucial for the formation of sharp conical structures with this laser system as well [Figure 3.3 (g-i)].

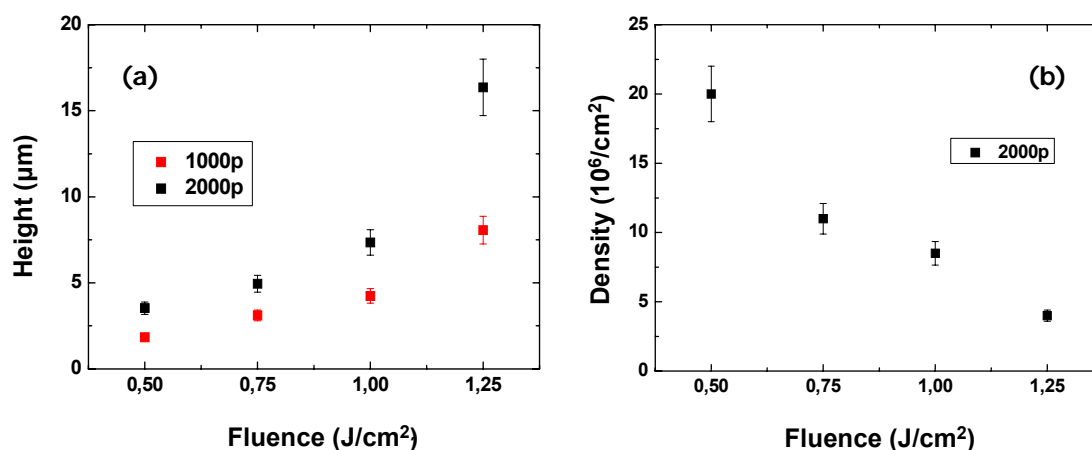


Figure 3.4 : Morphological characteristics of the spikes fabricated using the ps Nd:YVO₄ laser source in a 500 Torr SF₆ atmosphere; (a) The spikes' height as a function of laser fluence and (b) the spikes' density as a function of laser fluence.

3.2.3 Experiments with the ns, ps and fs KrF laser system

Laser pulse duration is expected to be one of the most important parameters concerning the macroscopic morphological characteristics of the resulting structures (see **Chapter 1**). The way that laser pulse duration affects the morphology and structure of the obtained features, and how they in turn determine the material properties, are still open questions. Previous attempts to address this physical problem^[8] have been limited to comparative studies between nanosecond (ns) and femtosecond (fs) laser sources, emitting however at very different wavelengths.

In this section we study the effect of laser pulse duration on the morphology of structures fabricated using the KrF laser system (248 nm) emitting pulses with different durations: 15 ns, 5 ps, and 500 fs. The influence of laser fluence, number of laser pulses (i.e. irradiation time) and ambient gas pressure (SF₆) on the morphology of the Si microcolumns obtained, is examined and information concerning the height and spike

density as a function of the number of pulses and the laser fluence respectively are shown.

- **248 nm, 15 ns**

The fluences tested were in the range of 1.6-2.7 J/cm² for 10 to 3000 laser pulses, at a repetition rate of 4 Hz. Experiments took place in vacuum as well as in the presence of SF₆ at pressures ranging from 250 -1250 Torr.

Figure 3.5 (a-c) shows the effect of laser fluence on the morphology of the structures fabricated in a 500 Torr SF₆ atmosphere. The spacing between neighboring spikes increases with increasing laser fluence, and observation also reflected in the spikes density as function of laser fluence [**Figure 3.6 (b)**]. Furthermore the spikes height increases with increasing number of pulses **Figure 3.5 (d-f)** and laser fluence [**Figure 3.6 (a)** and **Figure 3.5 (a-c)**].

With this laser source, more than 750 pulses are required for the formation of conical microstructures at fluences typically above 1.8 J/cm². In agreement to the results shown previously, the reactive gas plays an essential role in making the structures more conical, as in vacuum they are less sharp. Secondary tip decoration is also present on the cones' sides, which becomes a lot more pronounced at elevated reactive gas pressures **Figure 3.5 (g-i)** or fluences.

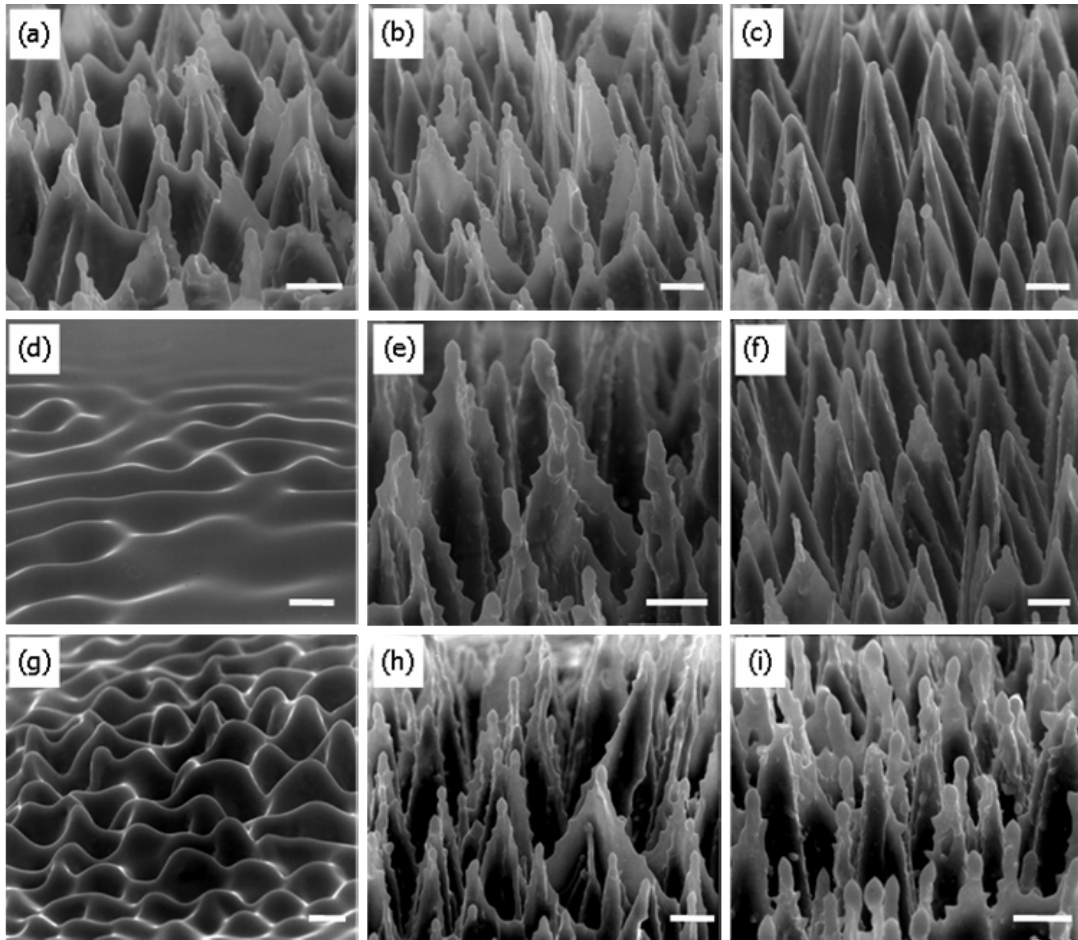


Figure 3.5 : Side SEM images of Si microstructures fabricated using the ns KrF laser source **(a-c)** the laser fluence effect; irradiation in a 500 Torr SF₆ atmosphere, with an average of 3000 pulses at a fluence of (a) 1.55 J/cm² (b) 1.85 J/cm² and (c) 2.15 J/cm². **(d-f)** the number of pulses effect; irradiation in a 500T SF₆ atmosphere, at a laser fluence of 2.15 J/cm² with (d) 250 pulses, (e) 750 pulses and (f) 2000 pulses. **(g-i)** the reactive gas pressure effect; irradiation with 3000 pulses under a fluence of 2.1 J/cm² in (g) vacuum, (h) 500 Torr SF₆ and (i) 1250 Torr SF₆ atmosphere. The scale bar is 10 μm.

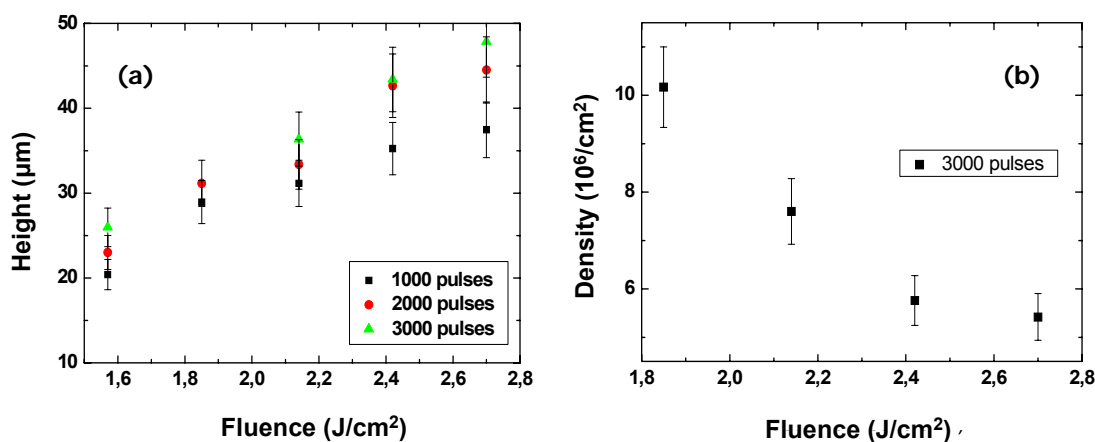


Figure 3.6 : Morphological characteristics of the spikes fabricated using the ns KrF laser source, in a 500 Torr SF₆ atmosphere; (a) The spikes' height as a function of laser fluence and (b) the spikes' density as a function of laser fluence.

- **248 nm, 5 ps**

The morphology of the structures obtained using the KrF ps laser source is studied in this section. The fluences used were in the range of 0.34 - 1.76 J/cm², while the number of pulses ranged between 50 and 1000, at a repetition rate of 4 Hz. Experiments were performed in vacuum as well as in the presence of SF₆, with its pressure varying from 250 to 1250 Torr. **Figure 3.7 (a-c)** shows SEM pictures of samples fabricated at different laser fluences.

The spikes density decreases with increasing laser fluence [**Figure 3.8 (b)**], in agreement to the trends observed with the other laser sources examined. **Figure 3.7 (d-f)** shows the effect of the number of pulses on the morphology of the structures obtained. Their height increases with the number of pulses as well as with laser fluence **Figure 3.8 (a)**. The formation of the structures with this laser system is initiated for more than 200 pulses, for fluences typically above 300 mJ/cm². Again the presence of the reactive gas is crucial for the formation of sharp conical microstructures, while the presence of secondary tips on the cones' peripheries becomes a lot more pronounced as the reactive gas pressure [**Figure 3.7 (g-i)**] or laser fluence increases.

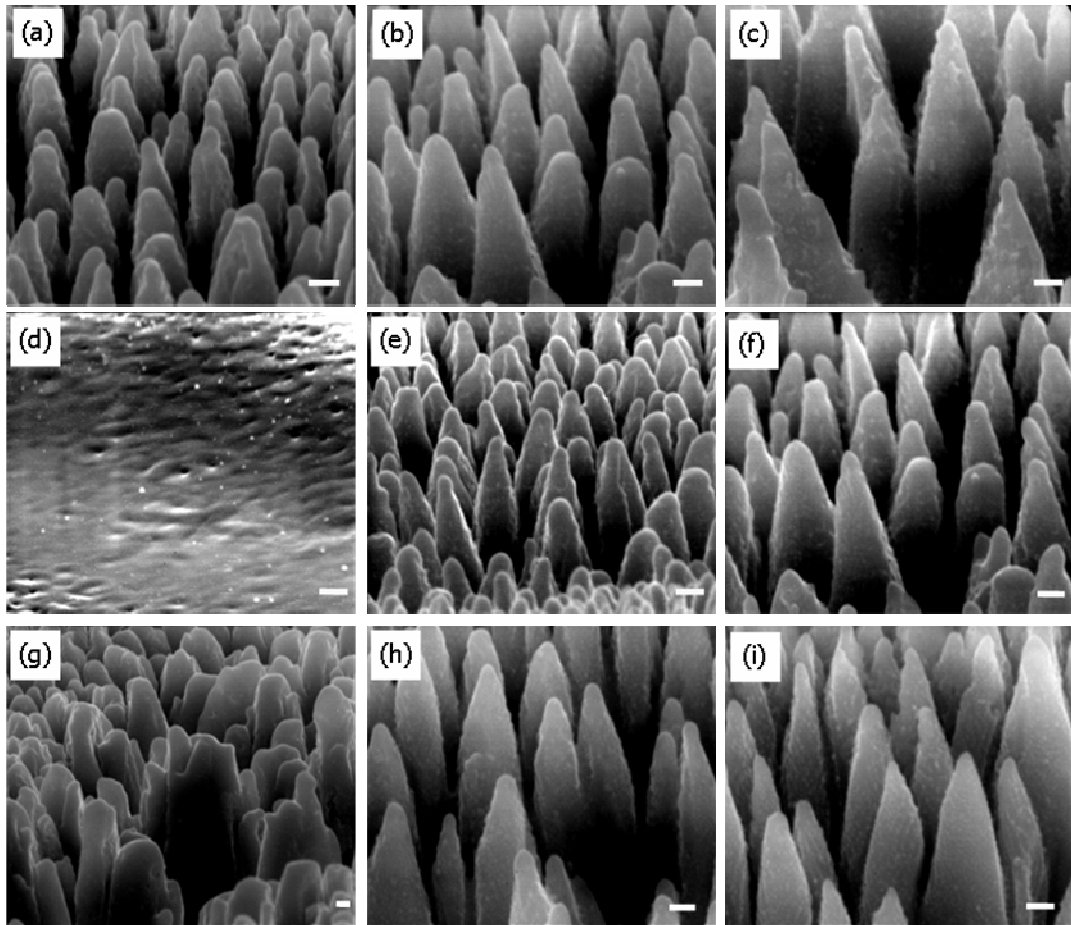


Figure 3.7 : Side SEM images of Si microstructures fabricated using the ps KrF laser source **(a-c)** the laser fluence effect; irradiation in a 500 Torr SF₆ atmosphere, with an average of 750 pulses at a fluence of (a) 340 mJ/cm², (b) 490 mJ/cm², and (c) 980 mJ/cm². **(d-f)** the number of pulses effect; irradiation in a 500T SF₆ atmosphere, at a laser fluence of 490 mJ/cm² with (d) 100, (e) 500, (f) 750 pulses. **(g-i)** the reactive gas pressure effect; irradiation with 1000 pulses under a fluence of 980 mJ/cm² in (g) vacuum, (h) 500 Torr SF₆ and (i) 1250 Torr SF₆ atmosphere. The scale bar is 10 μm.

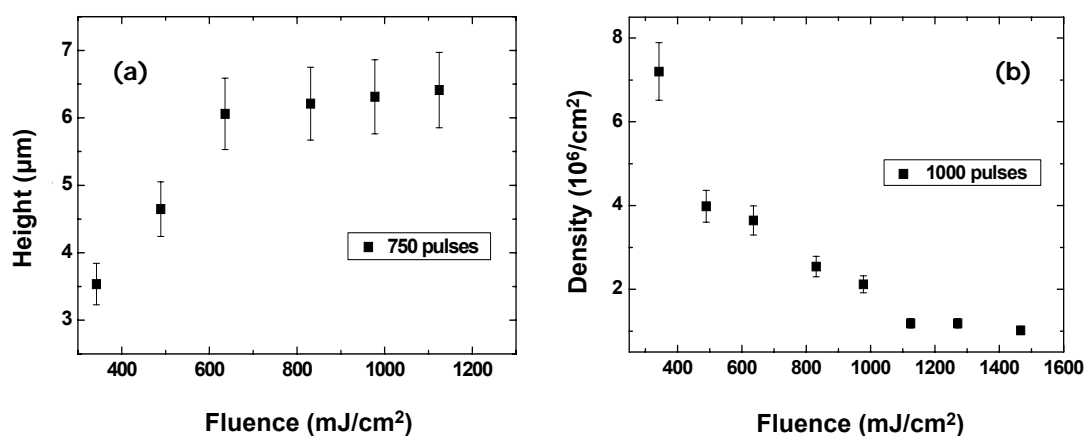


Figure 3.8 : Morphological characteristics of the spikes fabricated using the ps KrF laser source, in a 500 Torr SF₆ atmosphere; (a) The spikes' height as a function of laser fluence and (b) the spikes' density as a function of laser fluence.

- **248 nm, 500fs**

Figure 3.9 (a-c) depicts SEM images of Si spikes obtained with the use of the KrF fs laser source in the presence of 500Torr of SF₆. The laser fluences tested were in the range 0.34 - 0.87 J/cm², and the number of pulses from 10 to 3000, at a repetition rate of 4 Hz. As shown in **Figure 3.9 (a-c)**, the Si spikes separation increases (thus spikes density decreases) with increasing laser fluence [**Figure 3.10 (b)**].

The threshold for spikes formation using this laser source is relatively low as compared to the other pulse durations, at the same wavelength. Low number of pulses are also required in order for conical structuring to be promoted on the surface of Si with this laser source; less than 20 pulses are required for fluences typically above 300 mJ/cm², for structuring in a 500 Torr SF₆ atmosphere. Again the height of the structures increases with increasing number of pulses **Figure 3.9 (d-f)** and laser fluence **Figure 3.10 (a)**. Similar to the behavior reported for the other laser sources used, the presence of the reactive gas is crucial for obtaining sharp cones **Figure 3.9 (g-i)**.

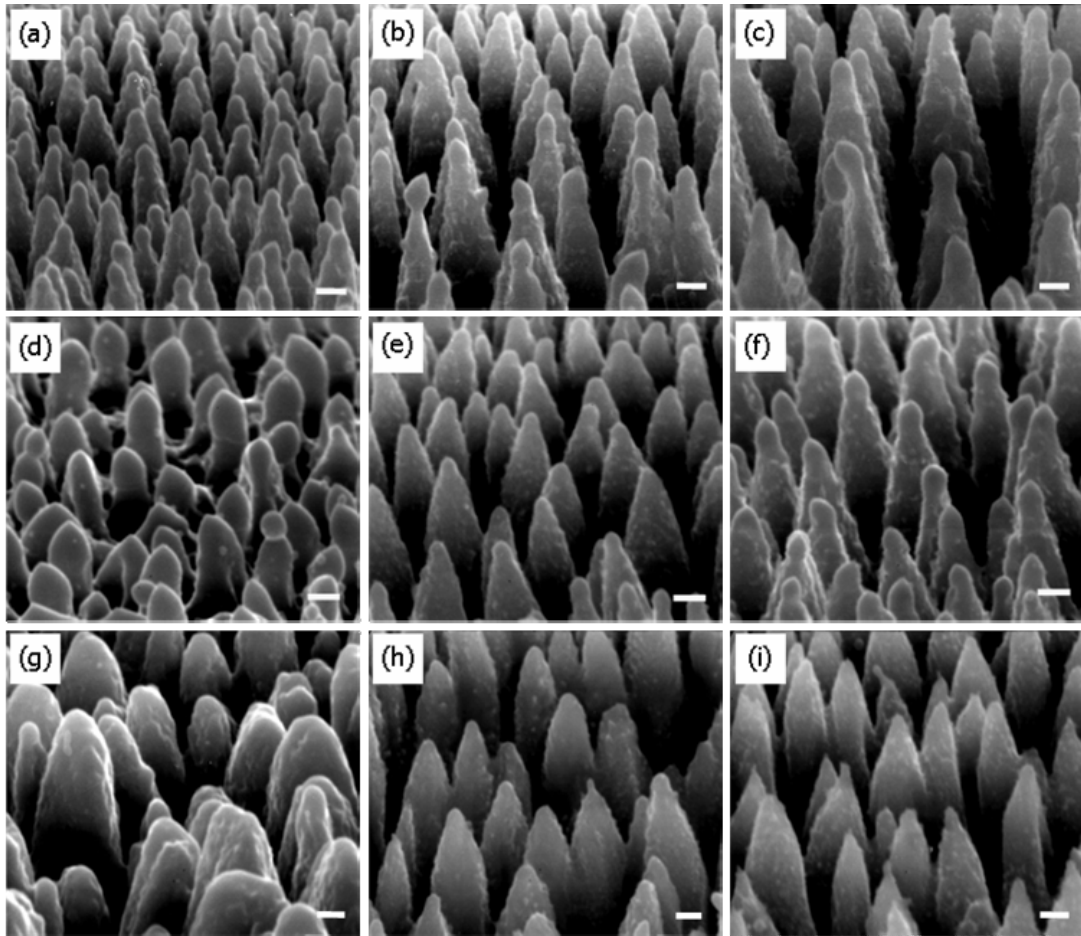


Figure 3.9 : Side SEM images of Si microstructures fabricated using the fs KrF laser source **(a-c)** the laser fluence effect; irradiation in a 500 Torr SF₆ atmosphere, with an average of 250 pulses at a fluence of (a) 340 mJ/cm², (b) 620 mJ/cm² and (c) 790 mJ/cm². **(d-f)** the number of pulses effect; irradiation in a 500 Torr SF₆ atmosphere, at a laser fluence of 525 mJ/cm² with (d) 20, (e) 50 and (f) 100 pulses. **(g-i)** the reactive gas pressure effect; irradiation with 750 pulses under a fluence of 525 mJ/cm² in (g) Vacuum, (h) 500 Torr SF₆ and (i) 1250 Torr SF₆ atmosphere. The scale bar is 10 μm.

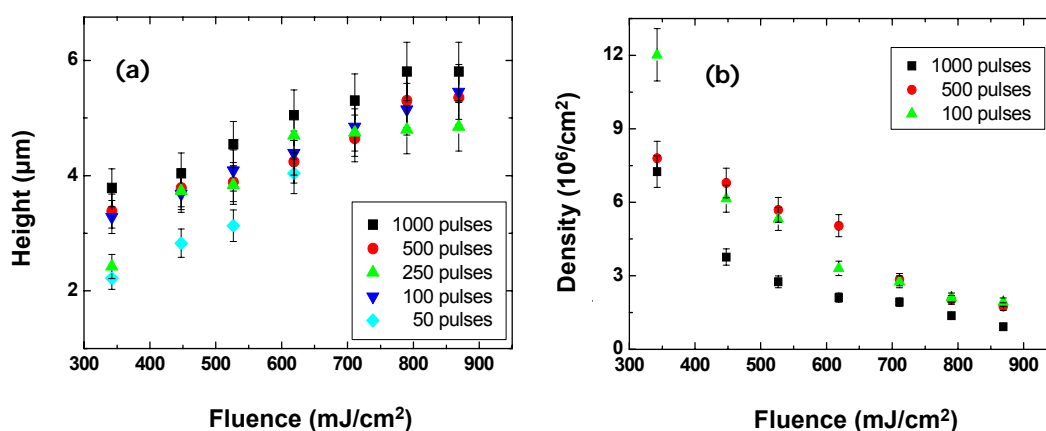


Figure 3.10 : Morphological characteristics of the spikes fabricated using the fs KrF laser source, in a 500 Torr SF₆ atmosphere; (a) The spikes' height as a function of laser fluence and (b) the spikes' density as a function of laser fluence.

3.3 Structural and compositional analysis

In this section we study the effect of laser pulse duration on the structure and composition of Si microcones fabricated using the KrF laser system (248 nm) emitting pulses at 15 ns, 5 ps, and 500 fs.

The micro-structured regions were 2x2 mm² wide. Transmission Electron Microscopy (TEM), High Resolution Electron Microscopy (HRTEM), Electron Energy Loss Spectroscopy (EELS) and Selected Area Electron Diffraction (SAED) were implemented in order to determine the fabricated cones' structure and crystallinity. Their composition was determined by means of Energy Dispersive X-ray Spectroscopy (EDS).

Typical images of the cones fabricated by using all three laser sources are shown in **Figure 3.11 (a-c)** obtained after cumulative irradiation of the Si wafers with the 15 ns, 5 ps, and 500 fs laser 248 nm pulses, respectively. **Figure 3.11 (d-f)** shows bright field cross section images of Si microcones fabricated using the ns (**d**), ps (**e**) and fs (**f**) laser

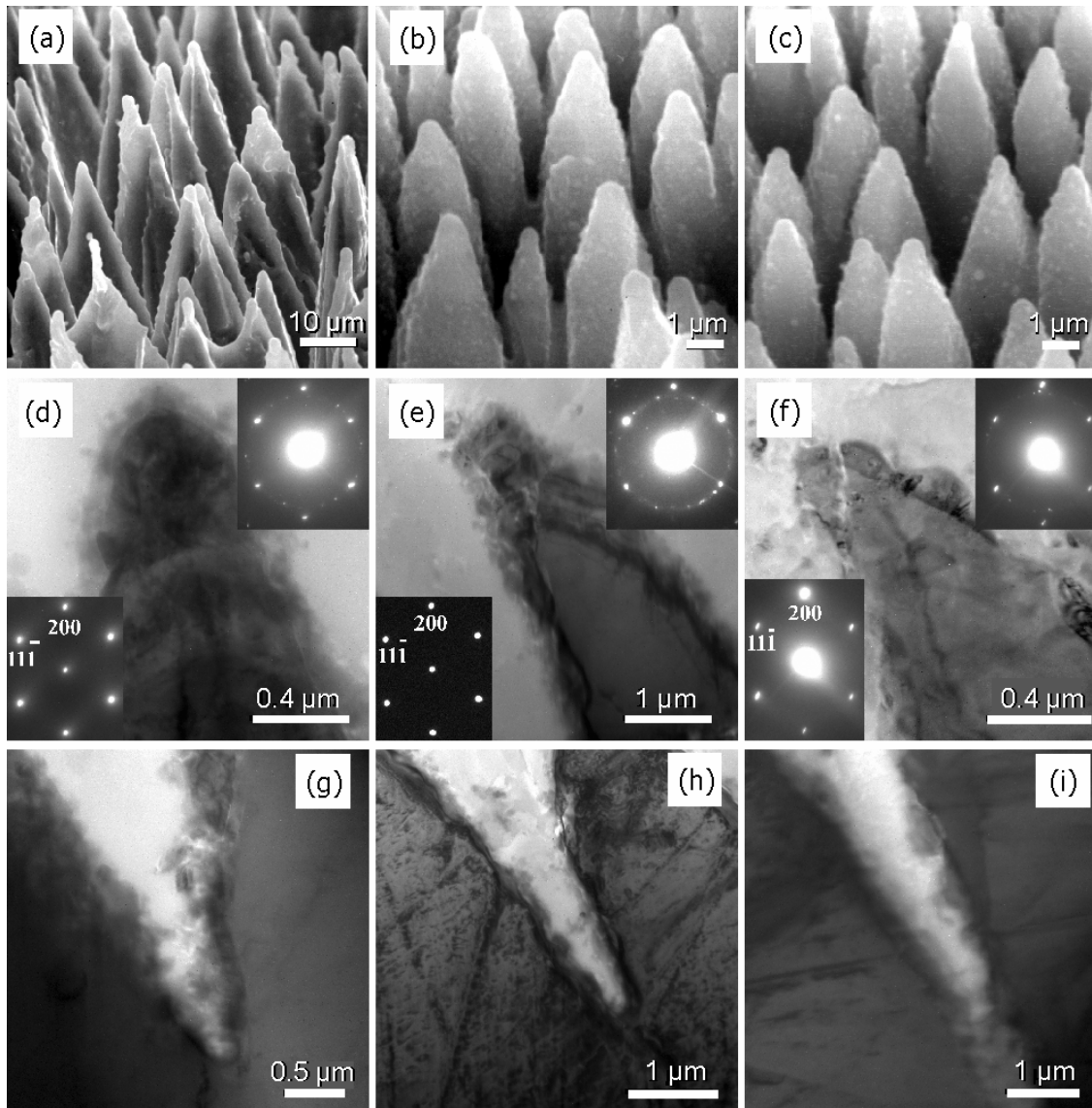


Figure 3.11: Side SEM view of Si spikes formed on Si (100) in a 500 Torr SF₆ atmosphere using (a) the ns laser source (2.14 J/cm², 2000 pulses), (b) the ps laser source (0.83 J/cm², 1000 pulses) and (c) the fs laser source (0.53 J/cm², 750 pulses). Bright field cross section images near the sample tip are shown for (d) the ns, (e) the ps and (f) the fs laser source fabricated samples, as well as the corresponding SAED patterns of the external layer and the spikes interior (upper and lower insets respectively). Bright field cross section images near the bases of the cones for the samples fabricated using (g) the ns (h) the ps and (i) the fs laser source, are also shown.

source. In all cases, the formed structures consist of a core of undisturbed Si covered with a few hundred nm thick, highly disordered layer. **Figure 3.11 (g-i)** shows cross section, bright field images corresponding to the bases of the Si cones. Previously published results^[8] on TEM characterization of samples fabricated using ns laser irradiation under similar conditions to ours, report only parts of the structures being covered by a disordered layer, and the tips of the structures being free of visible disorder. As it is clearly shown here, the disordered layer covering the Si cones extends from their tips down to their bases for all the laser pulse durations examined, while no interface can be distinguished between the Si substrate and the Si cones.

SAED patterns along the [110] Si zone axis of the cone interior are presented at the lower insets of **Figure 3.11 (d-f)**. It is evident that the interior of the spikes is single crystalline independently of the laser pulse duration used. Moreover, since the Si substrate is also oriented along the [110] crystallographic axis, the spikes obtain the same orientation as the substrate that they are grown on. The upper insets of **Figure 3.11 (d-f)** show the SAED patterns obtained from both the surface layer and the interior of the Si cones at the same orientation. Apart from the six Si {111} and {200} spots originating from the single crystalline interior of the cones, a ring pattern corresponding to the {111} Si planes can also be observed. This ring can be attributed to the highly disordered layer covering the Si cones, i.e. this layer comprises of many small Si crystallites, a result also verified by extensive dark field imaging in the TEM. This is in agreement with previously reported SAED results^[44, 45] on Si irradiated by fs, NIR laser pulses.

Figure 3.12 shows a HRTEM image of the structures fabricated by using the ps laser source at the interface between the core and the disordered outer layer. At the interior of the spike the fringes of the {111} and {200} Si planes are imaged. The associated fast Fourier transform (FFT) diffraction pattern shown in the upper inset indicates the high crystal quality of the spike. In the surrounding disordered layer, a Si nanocrystal can be observed, showing the {111} Si lattice fringes, as verified by the corresponding FFT diffraction pattern presented in the lower inset.

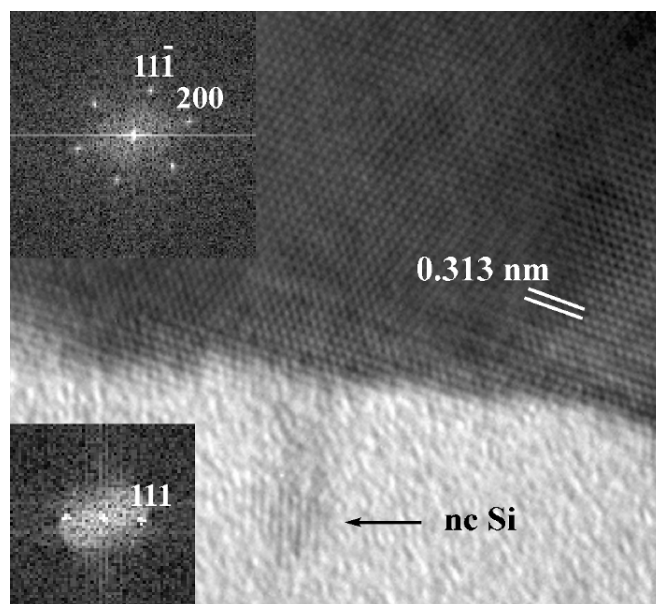


Figure 3.12: HRTEM image of Si structures fabricated using the ps laser source, at the external layer - core interface. The associated FFT diffraction patterns for the core and the surrounding layer are shown in the upper and lower insets respectively.

Still since none of the already exploited techniques are able to trace amorphous phases, EELS^[10] was implemented in order to probe the local bonding environment around the Si atoms. Typical electron loss Si L_{2,3} near edge spectra obtained from the interior and from the disordered layer around the Si spikes can be seen in **Figure 3.13 (a)**. The spectra are background subtracted and subsequently zero loss deconvoluted using the Fourier ratio method^[46] in order to obtain single scattering spectra. The electron energy loss near edge structure (ELNES) obtained from the interior of the spikes shows a first peak at 103.5 eV assigned to diamond-like coordinated Si, i.e. crystalline Si^[47,48] in agreement with the results obtained by SAED and HREM techniques. This peak is followed by a SiO₂ or SiO_x^[49,50] minute peak at 110.3 eV probably formed after the TEM sample was ion thinned, while the very broad peak at around 130 eV is reported for crystalline and amorphous Si, Si oxides and for some compounds^[47,49,50,51] Qualitatively the same features characterize the ELNES of the surrounding layer, although the silicon oxide peak (110.3 eV) is more pronounced, due to the high porosity of the layer leading to an increase of the (silicon oxide cover)/(Si bulk of the nanocrystals) ratio. More importantly, since the features corresponding to amorphous Si^[15] (a shoulder at 102 eV

and the absence of a peak at 110 eV) are not observed in the ELNES of the disordered surrounding layer, it may be concluded that it does not contain amorphous Si. The above results indicate that the disordered surface layer is a porous nanocrystalline Si layer.

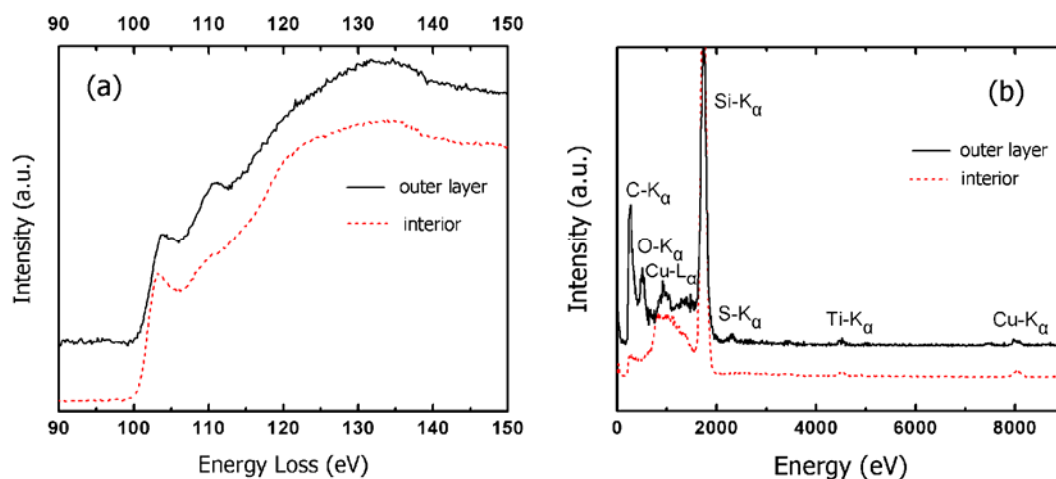


Figure 3.13: (a) Typical electron energy loss spectra and (b) typical EDS spectra from the core and the outer layer of the spikes. In both figures the corresponding spectra have been vertically translated with respect to each other for clarity. These spectra remain the same independently of the laser pulse duration used.

In order to determine the composition of both the disordered outer layer, as well as the interior of the fabricated microcones, EDS was implemented. The corresponding spectra are shown in **Figure 3.13 (b)**. Averaging over a 100nm area, it is found that the surface layer contains sulphur (S), a result of the photodissociation of SF₆, at a concentration of the order of 1 wt%. However no sulphur was detected in the spikes interior. Furthermore the presence of O on the EDX spectrum of the outer part of the spikes suggests the existence of silicon oxide on the surface of the cones, a result also confirmed by the EELS analysis. Finally it should be mentioned that the peaks corresponding to Cu and Ti originate from the TEM sample holder.

3.3.1 General Remarks

Despite the differences in the quantitative characteristics, a few common trends in the obtained Si spikes morphology were observed, independently on the laser system employed:

- The density of the microstructures increases with increasing laser fluence.
- The height of the resulting structures increases with increasing number of pulses, or laser fluence. Increasing either of these parameters also promotes the formation of secondary tips on the cones' surfaces.
- The Si spikes formed in vacuum are blunt and irregular. However they become more pronounced with increasing SF₆ pressure. Increase of secondary tip decoration (of the order of a few tens or hundredth nanometers) on the cone tip bodies especially at elevated SF₆ pressures (i.e. 1000-1250 Torr) is also observed.

The effect of laser pulse duration

Laser pulse duration plays a distinct role in the morphology of the structures. The spikes' dimensions as well as the average spacing decrease as the laser pulse duration is decreased, up to several times. We have observed an increase in the average spike height with the use of 15 ns laser source, which can reach up to several tens of micrometers, while the tip diameter ranges between 1.5 to 2 μm. On the contrary, with the 5 ps laser source, the height of the microstructures does not exceed 10 μm while the tip diameter can reach down to 900 nm. Similar behavior is observed with the 0.5 ps laser pulses, where the height of the microstructures can reach up to ~8 μm. The density of the structures formed by the 0.5 ps and the 5 ps irradiation is of the same order (10⁷ /cm²), whereas in the ns case it may be reduced down to 10⁵ /cm², a decrease up to two orders of magnitude.

Even though the morphology depends strongly on the laser pulse duration, it appears not to be crucial as far as the structure, composition and crystallinity of the formed spikes is concerned, since similar trends are present for all the laser sources used. The core of the spikes is single crystalline Si, following the crystallographic orientation

of the substrate they are grown on, while their surface is covered with a few hundred nm thick sulphur-doped nanocrystalline Si layer, where no amorphous phase is present.

3.4 Mechanistic aspects

The formation of the structures on the Si surface, upon laser irradiation in the presence of SF₆, as discussed in **Chapter 1**, has been attributed to the combination of 2 interactions; the interaction of laser with Si and the interaction of laser with the reactive gas, leading to chemical etching. However, due to the complexity of the process itself, their exact role and relative contribution are hard to identify. In the next sections, we try to assess these proposed mechanisms, and qualitatively correlate them to our experimental findings.

3.4.1 Laser-material interaction

The interaction of laser with material for the formation of Si microcones is two-fold; it forms the starting inhomogeneity and the subsequently preferentially removes material from the roughened surface. Material melting and subsequent capillary wave formation, has been proposed as the mechanism responsible for the formation of the initial surface roughening.^[23, 52] Further growth and development into microcones, has been ascribed to preferential material removal from the Si surface, owing to reflectivity variation with the angle of incidence.^[52]

▪ Starting inhomogeneity

The resulting inter-spike distance has a direct correlation to the spatial distribution of the initial inhomogeneity. The depth and/or the lifetime of the molten layer are known to increase with increasing laser fluence. Increasing the fluence deposits more energy in the Si substrate, melting more Si and therefore increasing the liquid layer depth and lifetime.^[20] On this basis, as may be derived from the dispersion relation for capillary waves (**Chapter 1**), increasing the laser fluence should correspond to the formation of capillary waves with higher spatial period. This is indeed observed experimentally for all the laser systems employed.

But also both the depth and/or the lifetime of the molten layer are expected to increase as the thermal diffusion length increases with pulse duration^[53] thus leading to an increase of the capillary wave period.^[52] It is thus anticipated that longer laser pulses will have a beneficiary effect to spike spacing. We have indeed shown that irradiation with the ns laser acts favorably to the spikes' morphology towards lower spikes' density and higher spikes' height, compared to ps and fs irradiation at 248 nm.

▪ Preferential material removal

In order to study how the surface roughness affects the microcone formation for 248 nm irradiation, we have developed an iterative phenomenological simulation. Starting from a sinusoidal surface, we calculated the transmitted energy per surface area in each iteration step.^[54] We then assumed that material is removed from the surface, i.e. its height is reduced, by a fraction of the penetration depth of the laser beam that is analogous to the transmitted energy. The new surface is input to the next step of the iterative process. Each iteration step actually represents the action of a single laser pulse. Our simulation, although very simple, is quite useful for obtaining a qualitative insight on the process.

The absorbed laser energy per surface area can be estimated using the Fresnel equations for different angle of incidence.^[55] For Si the refraction index at 248 nm is complex $n = 1.73 + 0.98i$.^[56] In this case, the absorptivity of the UV laser beam is practically constant $T = 0.35$ ^[57] (where $T = 1 - R$, and R is the reflectivity) for incidence angles up to 60° and then drops almost linearly to zero at 90° .

Figure 3.14 depicts the results of the simulation after 18 iterations for a sinusoidal initial surface with period (a) 2 μm and (b) 10 μm and height 200 nm. The simulation results show that as the period gets smaller the hills are more quickly transformed into cone shaped structures. This result can be justified by the fact that for the same height, the smaller period leads to higher surface slope between hills and valleys and thus to an enhancement of the spatial inhomogeneity of the absorbed energy. On the other hand, as the period is increased the surface slope is reduced and the energy is more homogeneously absorbed.

This simulation shows that the characteristic conical shape of the formed spikes could be attributed to the dependence of the absorbed laser energy to the surface slope. Likewise, for an arbitrary shaped surface the steepest microstructures transform faster into spikes. The final periodicity of the spiked Si surface is influenced not only by the periodicity of the original template, but also by the height distribution of the surface.

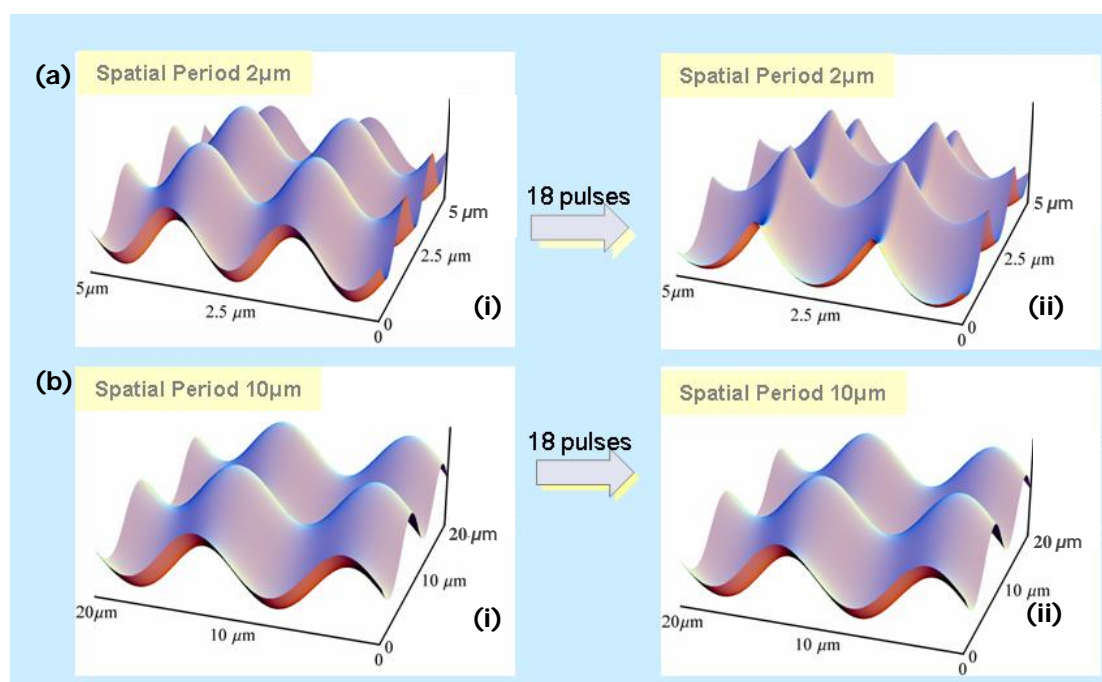


Figure 3.14: Simulation results for different periodic structures (a):(i) for 2 μm period, 0 pulses and (ii) after the irradiation with 18 pulses (b):(i) for 10 μm period, 0 pulses and (ii) after the irradiation with 18 pulses.

3.4.2 The role of the reactive gas (SF_6)

As has already been underlined, the Si spikes formed in vacuum are blunt and irregular, while they become more pronounced with increasing SF_6 pressure. Similar behavior has been observed in halogen containing atmospheres (e.g. Cl_2 ^[38]). Also of interest is the observation that Si spikes do not form in a neutral atmosphere such as Ar^[29] or N_2 . This is consistent with the interpretation of Si spikes formation as a synergy of laser-matter interaction and laser assisted chemical etching.

The etching role of SF₆ is attributed to the formation of F radicals, which may be formed through a number of processes reviewed in **Chapter 1**. Nevertheless, the exact way that the chemical etching of Si takes place, as part of the Si spikes formation process is still unclear.

On the other hand, the presence of S in a high concentration in the EDS spectra, as shown in **Chapter 3**, suggests that the formation mechanism involves the dissociation of SF₆. This can take place through excitation of SF₆, (e.g. vibrationally excited SF₆ is very reactive with Si) or its direct photodissociation in the gas phase. Any of these processes are highly likely to take place under the irradiation conditions used in the experiments we have described, through multiphoton absorption in SF₆. This is because the laser intensities employed ($I=10^8$ - 10^{12} W/cm²) exceed the threshold intensity above which multiphoton phenomena may take place in polyatomic molecules having a high density of states ($\sim 10^6$ W/cm²).

A simplified possible scenario^[58] explaining how SF₆ may react with the Si surface is the following (**Figure 3.15**):

- Laser pulses are focused onto the Si surface.
- The high intensity pulses disrupt the molecules close to the surface leading to the creation of reactive fluorine radicals [**Figure 3.15 (b)**].
- These radicals react with silicon (possibly in a liquid form) and form SiF_x compounds [**Figure 3.15 (c)**].
- These compounds are desorbed by the laser, while volatile species (such as SiF₄) leave the surface [**Figure 3.15 (d)**].

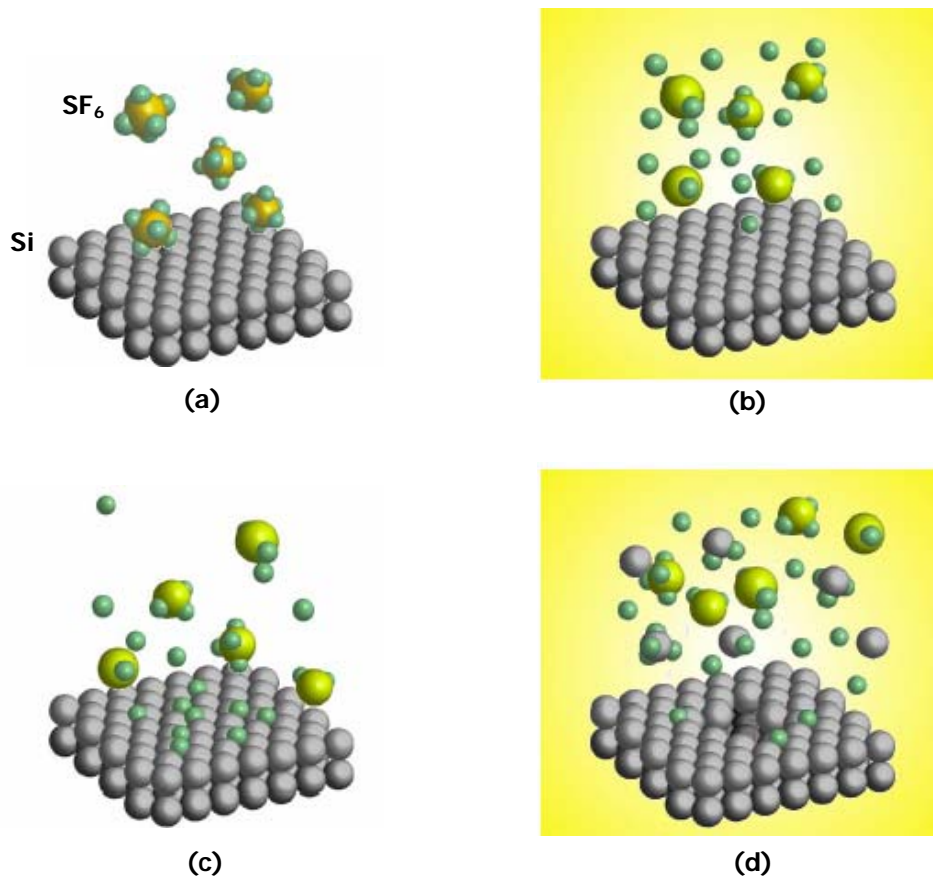


Figure 3.15: Possible interaction mechanism of SF₆ with Si. ^[58]

3.4.3 Growth Mechanisms and Laser Pulse Duration

Figure 3.16 depicts a cross sectional view of the Si spikes obtained in an SF₆ environment using different laser sources. A striking feature is the fact that the structures formed with the ns KrF laser source protruded tens of microns above the initial surface in oppose to the all the other structures fabricated either with the fs or the ps KrF laser sources where the spikes do not protrude above the initial surface at all. The same trend was observed in the case when microstructuring took place using the Ti:Sapphire laser system.

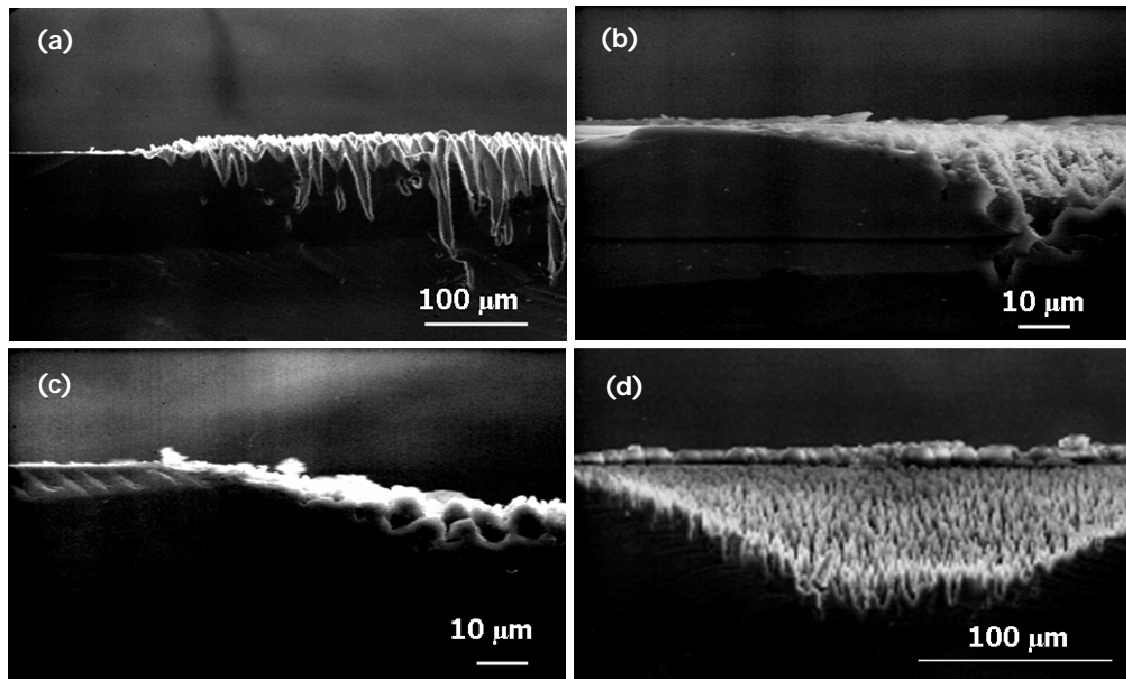


Figure 3.16: Cross sectional view of single spots containing Si spikes, obtained in a 500 Torr SF_6 atmosphere using (a) the KrF ns, (b) the KrF ps, (c) the KrF fs and (d) the Ti:Sapphire fs laser source.

This suggests that in the case that ns laser pulses are employed for Si microstructuring, growth should involve redeposition (not merely erosion) since the obtained cones grow well above the surrounding surface. It has been proposed that growth occurs by a “catalyst free” VLS (vapor-liquid-solid) mechanism^[52] that involves repetitive melting of the tips of the columns/cones and redeposition there of the ablated flux of Si-containing vapor produced by ablation of the surface region between columns (especially from pits or grooves). This mechanism explains the fact that Si spikes protrude above the initial surface.

On the contrary, the fact that the structures made with fs and ps laser pulses have not been seen to protrude above the initial Si surface suggests that ablation or removal of Si by chemical etching in this case is dominant over redeposition. The presence of nearly spherical tips of cones made by fs irradiation has been explained as the result of resolidification of a molten droplet. This phenomenon has also been observed in the past when ns irradiation was applied.^[31] The presence of this resolidified molten droplets at

the tips of the obtained Si cones opens up the possibility that a VLS growth mechanism similar to that observed for ns irradiation operates with fs pulses as well.

The structures made with different pulse durations exhibit many qualitative similarities so we can assume that similar processes are operative for their formation. However it is clear that the balance between these processes is different in each case.

3.5 Replication of laser fabricated Si structures

In this section we demonstrate the replication of laser fabricated Si conical microstructures. Large areas containing Si structures are fabricated by using the Nd:YVO₄ laser system ($\lambda=1064$ nm, $\tau=12$ ps), in the presence of SF₆. These structures serve as the “master” morphologies which are replicated on PDMS, by molding in vacuum. Using the PDMS mold carrying the negative spikes morphology, replicas of the initial spiked Si morphology can be made out of several materials. As an application we demonstrate the successful reproduction of the Si morphologies on ORMOCER (ORganically MOdified CERamic), a UV photocurable organic-inorganic hybrid material, with particularly interesting properties which may find use mainly in optical and biological applications.^[59, 60, 61]

Replication, i.e. the copying of 3D surface microstructures from a master sample mold into a formable material, may offer an important fabrication technology for certain types of applications. This technology features limited processing steps and prompts lower production costs for mass production, since many copies can be made from a single mold. PDMS (polydimethylsiloxane), a silicon elastomer widely used in replica molding is used in a second step of this work in order to copy the laser fabricated Si morphologies, under vacuum.

The replication process involves three processing steps as illustrated in **Figure 3.17**; **(a)** The laser fabrication of the micrometer scale structures (which serve as the master pattern), **(b)** the fabrication of a negative PDMS replica (negative mold) from the original Si master and **(c)** casting of liquid ORMOCER followed by UV curing and

careful peeling off. Its surface now replicates the relief microstructures on the surface of the original master.

The initial surface morphology is casted with PDMS (polydimethylsiloxane). The material used is Sylgard 184 provided by SESCO semiconductor as a complete kit with curing agent. The rather viscous liquid is mixed thoroughly with the curing agent in the weight ratio 10:1 for 15 min with a stirrer. Pouring a liquid prepolymer of PDMS over the master structure and allowing it to cure at 110 °C in vacuum produces a mold which holds the negative of the original pattern.

For the subsequent replication of the original pattern on ORMOCER, the liquid prepolymer containing 1.8 wt% of the radical photoinitiator Irgacure 369 is poured on the

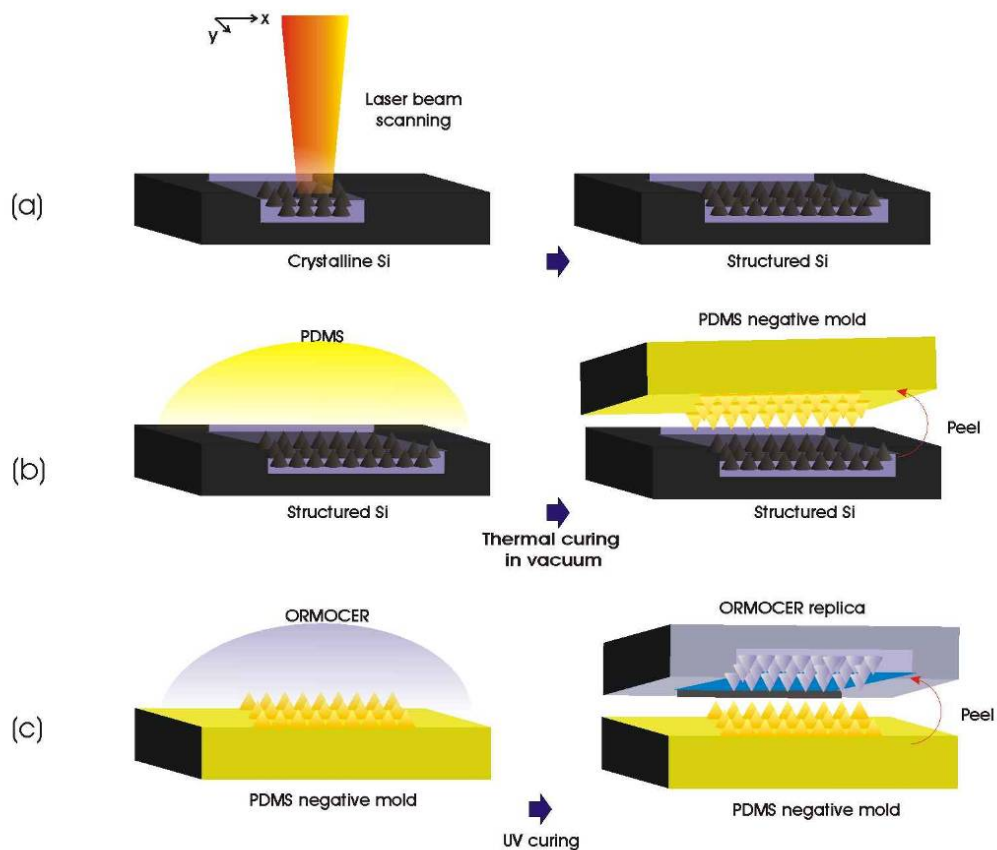


Figure 3.17 : The replica-molding process: (a) Fabrication of large areas containing Si spikes on crystalline Si by ps laser irradiation. This will serve as the master structure. (b) The master is coated with PDMS to form a PDMS mold and (c) ORMOCER replicas are subsequently cast from the PDMS mold.

fabricated PDMS mold. ORMOCER can be polymerized by illumination with ultraviolet light around 365 nm. The photoinitiator is radicalized with exposure to ultraviolet light.

The laser structured Si samples used as masters for the replica molding, consisted of a standard 5 x 5 mm² structured area, plus an area containing the letter “Z”, shown in **Figure 3.18 (a)**. This offered the possibility to always image the same region of the sample. In this case processing took place in a 500 Torr SF₆ atmosphere with a scanning speed of 100 mm/s exposing any given spot on the Si surface to an average of 500 pulses. The laser fluence was 1.3 J/cm².

The density of the Si spikes at the central areas of the processed regions is of the order of 5 x 10⁶ spikes/cm². This corresponds to the minimum density obtained. In these regions the height reaches up to 9 μm while the tip radius of the order of 500 nm, resulting to an aspect ratio of ~18. However, since macroscopic patterns are made out of overlapping between consecutive scans of the laser beam, and taking into account the dimensions of the structured area carrying the letter “Z” engraving with regard to the focused beam size, it is expected that structures near the edge pad will have smaller dimensions in terms of period, height and aspect ratio. This results to a wider statistical distribution, corresponding to the presence of different morphologies in the whole structured area.

SEM images of the resulting structures are shown in **Figure 3.18 (a-c)** with increasing magnification viewed under a 45° tilt. **(a)** the letter “Z” containing Si spikes, **(b)** higher magnification at one of the edges of the letter “Z” and **(c)** central area of the processed region.

In a second step, the surface morphology is casted with PDMS. In this case, silanization of the structured Si surface was not required as is extensively done in other replication techniques,^[62, 63] in order to prevent adhesion between the PDMS and the Si master. Following the mixing process, the liquid mass contains air, which has to be removed before the molding. For this purpose the PDMS is put in a vacuum chamber for 45 min. At room temperature the PDMS with the curing agent can be handled for about 2 hours. In the meantime the Si samples with the structured surfaces are placed in small bowls made from aluminium foil. The structured side is facing up.

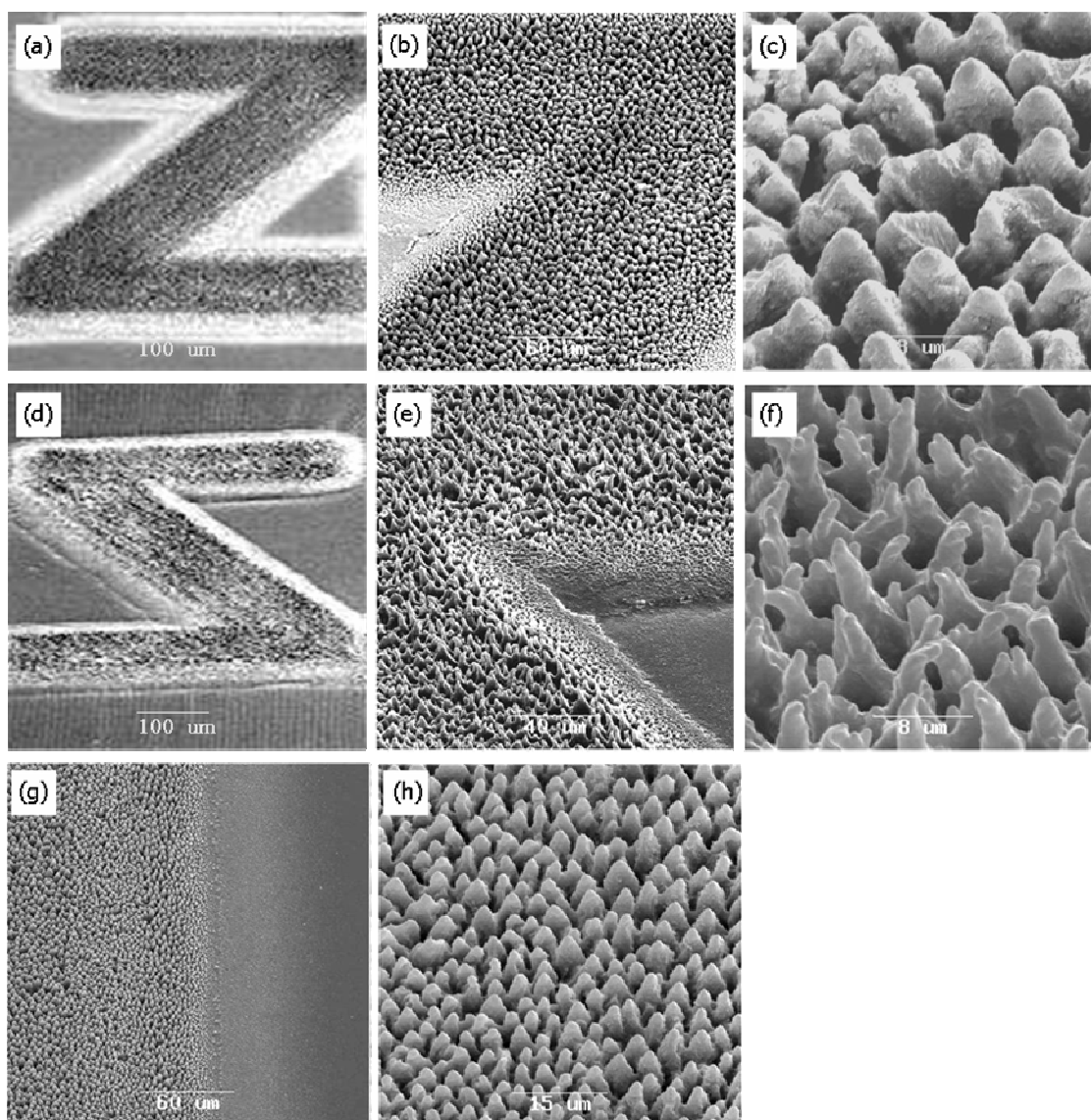


Figure 3.18 : (a-c) Side scanning electron microscope view of Si surfaces structured by an average of 500 pulses by ps-laser irradiation in a 500 Torr atmosphere, under successive magnification. The laser fluence was 1.3 J/cm^2 . (d-f) SEM pictures of structures transferred on PDMS from the (unsilanized) master structure shown in (a-c), under successive magnification. (g-h) SEM images of the produced ORMOCER replicas which are cast from the PDMS negative mold. (g) the area at the edge and (h) higher magnification of the interior.

When the air is removed from the PDMS mixture the liquid mass is poured into the small bowls submerging the samples. For avoiding air trapping in the deep structures between the cones the samples are placed again in the vacuum chamber. After one hour

the samples are heated up to 110°C for 24 hours. In this time the PDMS hardens to a rubber like consistency. When the samples are cooled the PDMS is carefully peeled off of the Si pieces. The resulting surface replicates the negative relief microstructures on the original master structure. **Figure 3.18 (d-f)** shows SEM images of the transferred morphology on PDMS, under successive magnification. The surface morphology has been accurately reproduced on PDMS, indicating that all the air had been removed. The slight distortion observed on the top of the transferred morphologies, is something which is not uncommon for high aspect ratio pattern transfer. ^[63] However the distortion towards the edges where lower aspect ratio structures are present is not as pronounced.

In the third step the negative surface morphology is transferred into ORMOCER. The PDMS regions carrying the negative Si morphology are covered with the ORMOCER which is liquid in the initial state and is polymerized by illumination with ultraviolet light. For this purpose the samples are illuminated with an 8 W (electrical power consumption) UV Lamp emitting at 366 nm for 20 min. While the polymerization process is a radical reaction, it is sensitive to the air. The contact with oxygen prohibits the polymerization. But also the PDMS contains a lot of air that has been diffused into its fiber like structure after polymerization, so that samples are put in the vacuum chamber again.

When the air is removed out of the chamber the ORMOCER containing the photoinitiator is polymerized. The hardened ORMOCER is carefully removed from the PDMS with tweezers. Meanwhile the negative morphology on the PDMS surface remains unaltered, being available for further moldings. The resulting surface of the ORMOCER is investigated again with SEM. **Figure 3.18 (g)** shows the resulting structure on ORMOCER while **Figure 3.18 (h)** corresponds to a higher magnification image, showing the central processed area accurately replicated from the original Si surface morphology.

3.6 Conclusions

In conclusion we have used laser irradiation in a SF₆ environment for the fabrication of conical microstructures on the surface of single crystalline Si. Laser microstructuring was

tested by using different laser sources. We have studied the effects of the processing parameters (laser and reactive gas) on the morphology, composition and structure of the features obtained to find common trends to be present independently of the laser source used. More specifically we find decreasing density with increasing laser fluence (typically tuned between 10^5 - $10^7/\text{cm}^2$) and increasing height with increasing number of pulses or laser fluence (from 1 to 60 μm). The reactive gas is proven to be essential for promoting sharp conical feature formation.

Laser pulse duration is identified as the critical laser parameter for the morphology of the structures obtained; the size and aspect ratio of the structures decreases with decreasing pulse duration. However pulse duration does not affect the structure and composition of the surfaces obtained, since they both remain practically unaltered for all the pulse durations used. The cones consist of a core of single crystalline Si following the crystallographic orientation of the substrate they were grown on, which is covered by a disordered nanocrystalline, sulphur-doped Si layer with a thickness of a few hundred nanometers, on which no amorphous phase could be detected. We have correlated and interpreted our results with regard to possible mechanisms operative during the irradiation process.

We have shown that by choosing high peak power, high repetition rate laser systems we are able to accelerate the fabrication process up to hundreds of times, and have utilized these structures as “master” morphologies for replication purposes. Replica molding was used in order to successfully and precisely transfer the fabricated morphologies on PDMS under vacuum. These structures served as a mold which was in turn used for the structuring of the photocurable, organic/inorganic hybrid material ORMOCER.

Chapter 4

Optical Properties of Laser Structured Si

4.1 Introduction

Si is a semiconductor commonly used in optoelectronic devices, such as solar cells and photodetector applications. However certain shortcomings make its use limited in certain types of applications; for example as an indirect bandgap material, it is a poor light emitter. Furthermore, the crystalline Si band gap (1.1 eV) makes its absorption and photoresponse to abruptly decrease for wavelengths typically above 1100 nm. This makes crystalline Si unsuitable for many near infrared applications, since it is insensitive to wavelengths that are extensively used for both telecommunications and scientific instrumentation.

Significant amount of research effort has been oriented towards overcoming this limitation. The main strategy followed is related to the implementation of alternate semiconducting materials or compounds (Ge, InGaAs etc.) for detection in the near infrared. Extended detection ranges as well as high responsivity have been reported for germanium (Ge) on Si photodetectors and wafer bonded photodetectors on Si substrates.^[64,65] Nevertheless, Si-based near infrared detectors could lower production costs and facilitate integration with other microelectronics.

Laser irradiation in a reactive gas atmosphere resulting to the formation of surface structures, could be used as such as an alternate approach for improving the optical

properties of Si. For example (**Figure 4.1**) the initially grey Si surface turns black upon structuring (*black Si*), suggesting a change in the optical properties of this surface with respect to the flat, in the visible spectral range. However, laser structuring in the presence of SF₆ can increase substantially the absorption of Si in near infrared as well. [44,45]

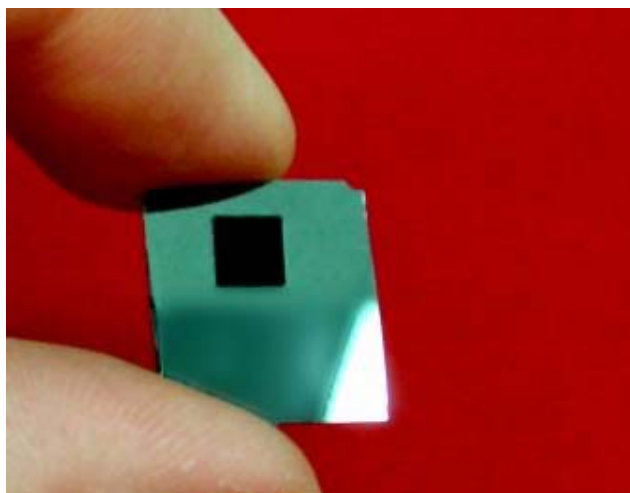


Figure 4.1: Top view of a fs laser structured Si surface (black area) with respect to the flat Si surface (grey area)

The optical properties of laser structured Si have been studied by Mazur et al.^[44,45] The findings of these authors are almost exclusively based on studies using fs Ti:Sapphire lasers. It is yet to be defined whether the use of this fs laser offers some particular advantage on the optical properties of the resulting surfaces. We pursue these studies further through the employment of lasers with different pulse durations. Furthermore, we examine ways for increasing the speed of the process in order to eventually produce practical devices. In particular, in this chapter we study the optical properties of laser structured Si. Using different laser sources, we fabricate extended areas of Si spikes and measure the absorptance as a function of wavelength. We study the effect of different laser irradiation parameters (e.g. laser fluence, laser pulse duration) and reactive gas pressure on the optical absorptance of the fabricated structures, as well as their response to post-irradiation HF treatment and thermal annealing. We discuss and correlate these findings with respect to the chemical and structural modifications the Si surface undergoes upon intense laser irradiation.

4.2 Optical Parameters

Three processes can take place when light impinges on a surface: reflection, transmission, and absorption.

Reflectance (R), Transmittance (T) and Absorptance (A) are related through:^[66]

$$R(\lambda) + T(\lambda) + A(\lambda) = 1 \quad (\text{Eq. 4.1})$$

The relative contribution of each process is determined by a material-dependent complex refractive index:^[67]

$$\tilde{n} = n + ik \quad (\text{Eq. 4.2})$$

The real part n is called the refractive index and relates the velocity of light in a medium to that in vacuum:

$$v = \frac{c}{n} \quad (\text{Eq. 4.3})$$

where c is the velocity of light in vacuum.

The imaginary part k is called the extinction coefficient and is a measure of the absorption in the material. The absorption coefficient α of a medium is defined by the well known Lambert-Beer's Law: the transmittance, $T \equiv \frac{I_t}{I_i}$, of a layer decreases exponentially with the distance traveled through the layer (z), where I_i is the incident intensity and I_t is the transmitted intensity.^[67]

$$I_t(z) = I_i \cdot e^{-\alpha \cdot z} \quad (\text{Eq. 4.4})$$

with

$$a = \frac{4 \cdot \pi \cdot k}{\lambda} \quad (\text{Eq. 4.5})$$

where α^{-1} is the distance by which the incident flux has decreased to $1/e$ and is called skin or penetration depth.

For normal incidence of light from air to the material, the reflectance of a material, defined as the reflected to incident intensity ratio, is expressed as:^[67]

$$R \equiv \frac{I_r}{I_i} = \frac{(1-n)^2 + k^2}{(1+n)^2 + k^2} \quad (\text{Eq. 4.6})$$

4.3 Optical Measurements

We measure the total hemispherical reflectance (R) and transmittance (T) of our samples from 250 nm to 2500 nm using the spectrophotometer described in **Chapter 2**, equipped with an integrating sphere. The absorbance (A) of each sample is then calculated through

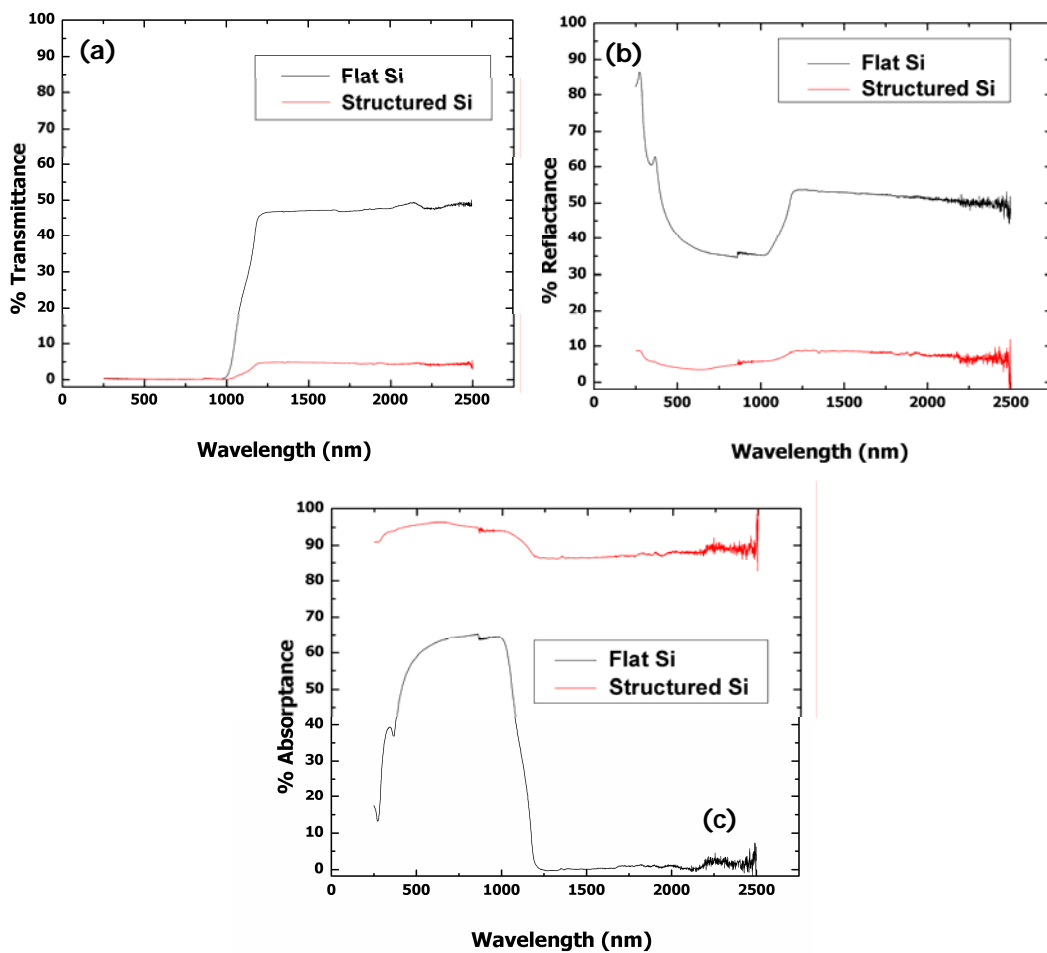


Figure 4.2: (a) Transmittance, (b) Reflectance, and (c) the calculated Absorbance of Si structured using the 12 ps at 1064 nm laser source (1.375 J/cm^2 , 1000p, 250 T SF_6). The same measurements are shown for unstructured, single crystalline Si for reference.

Eq. 4.1. Typical reflectance, transmittance and absorptance spectra of the structured samples are shown in **Figure 4.2**. The corresponding spectra of unstructured Si surfaces are also shown for comparison

Generally speaking, there are two ways to produce below-band gap absorption in ordinary Si; by introducing impurity atoms or by changing the structural order. First of all, impurity atoms bind electrons with a different potential and thus can introduce states in the band gap. On the other hand, structural changes cause deviations from the periodic crystal lattice and introduce electronic energy levels within the band gap. Transitions from or to these levels can then occur, which enable absorption of photons with below bandgap energies. Amorphous silicon (a-Si), polycrystalline silicon (poly-Si), and damaged/deformed silicon exhibit below bandgap absorptance.^[68, 69, 70] In all cases, the presence of significant disorder broadens the abrupt band edge of crystalline Si producing so called band tails of localized states extending into the gap.

The spectra shown in **Figure 4.2** show absorption at below band gap wavelengths ($>1.1 \mu\text{m}$), where crystalline Si does not normally absorb, suggesting that chemical modification, structural modification or combination of both maybe responsible for the improved optical performance of the laser structured samples. In the following sections, the effect of SF₆ pressure, laser fluence, laser pulse duration and thermal annealing on the optical properties of laser structured surfaces is studied. The observed trends are interpreted with regard to the structural and chemical modifications of the surface associated with the laser treatment, as demonstrated in **Chapter 3**.

4.3.1 The effect of the reactive gas pressure

This section examines the effect of the SF₆ pressure on the optical absorptance of laser structured Si. The laser system used was the ps Nd:YVO₄ laser ($\lambda=1064\text{nm}$, $\tau=12\text{ps}$). **Figure 4.3** shows the absorptance spectra for samples fabricated in vacuum and at different reactive gas pressures (50-500 Torr). We find the absorptance to increase with SF₆ pressure, primarily for below bandgap wavelengths. However, the visible absorptance remains practically unaltered, close to 90%, within the reactive gas pressure

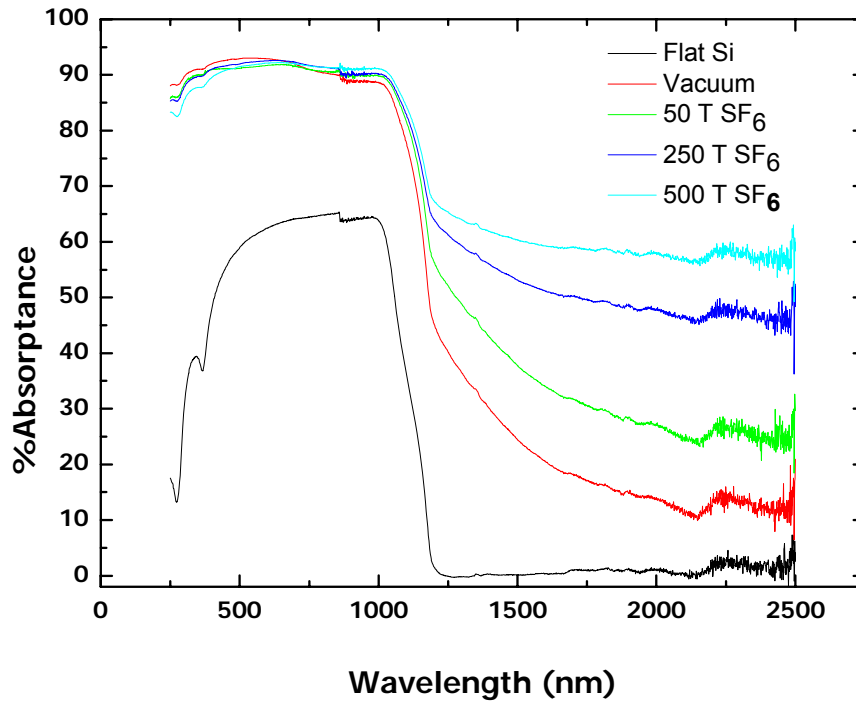


Figure 4.3: Absorbance of laser fabricated Si structures as a function of the wavelength for different pressure of SF₆. All the samples were fabricated using 1000 pulses at a laser fluence of 0.5 J/cm². The absorbance of the unstructured Si substrate is also shown for comparison.

range tested. For lower gas pressure and in vacuum the optical absorbance tends to decrease with increasing wavelength, at the below bandgap region.

4.3.2 The effect of laser fluence

In this section the effect of the laser fluence on the structures obtained is studied, for samples fabricated both in vacuum as well as under 500 Torr of SF₆, using the ps Nd:YVO₄ laser laser system ($\lambda=1064\text{nm}$, $\tau=12\text{ps}$). For the samples fabricated in vacuum (**Figure 4.4**), the absorbance at the visible spectral range, reaches values of more than 85% independently of the laser fluence used. An increase in the absorbance in the below-bandgap region is also observed with increasing laser fluence, while its absolute value decreases for higher wavelengths, until reaching a stabilization region in the area of 2000-2500 nm.

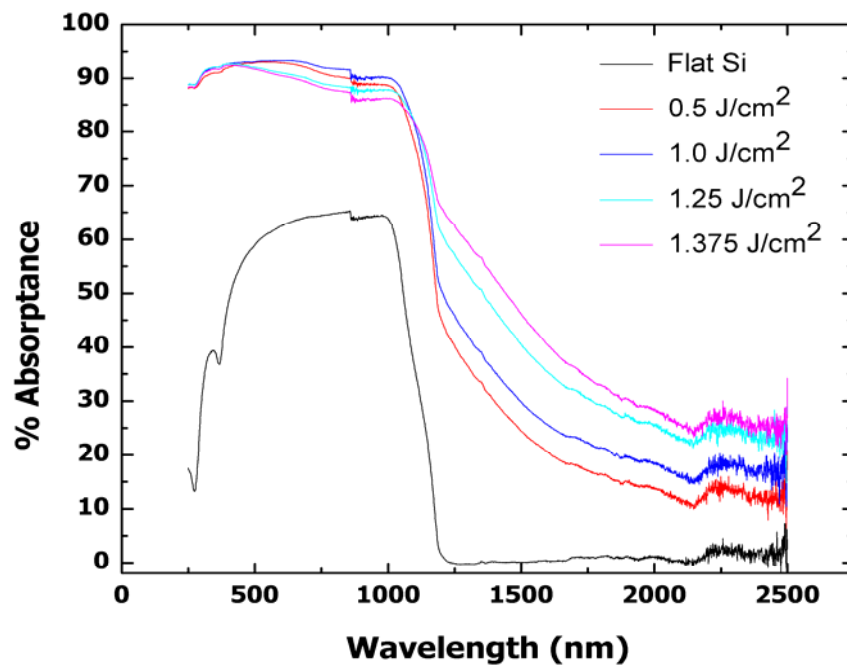


Figure 4.4: Absorptance of laser fabricated Si structures as a function of the wavelength for different fluences. All the samples were fabricated using 1000 pulses in vacuum. The absorptance of the unstructured Si substrate is also shown for comparison.

For the samples fabricated in a 500 Torr SF₆ atmosphere (**Figure 4.5**), again increased absorptance (>90%) is observed for all above-bandgap wavelengths. The absorptance for the below-bandgap wavelengths increases with increasing laser fluence. In fact for the highest laser fluences used, the value of the below-bandgap absorptance remains practically constant in the wavelength range (~ 1300-2500 nm).

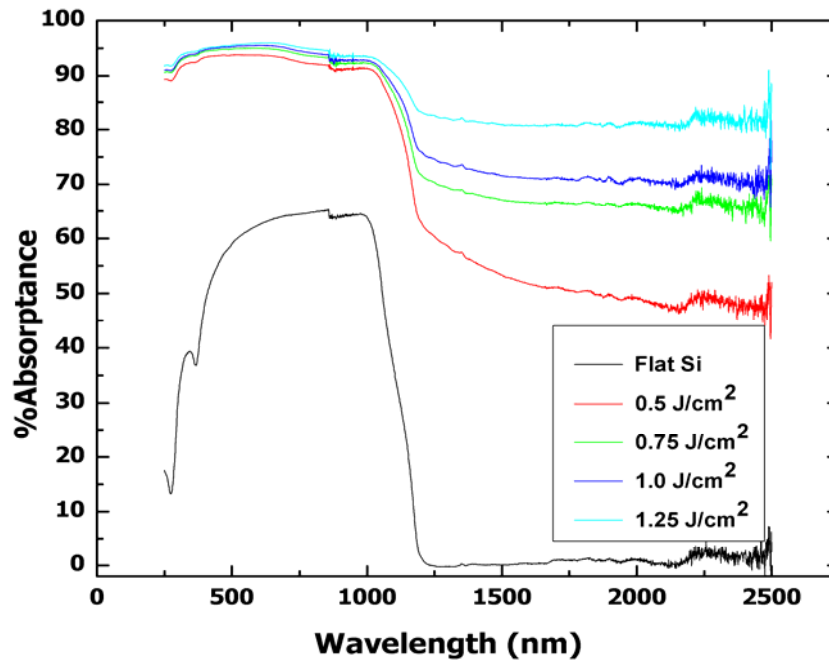


Figure 4.5: Absorbance of laser fabricated Si structures as a function of the wavelength for different fluences. All the samples were fabricated using 2000 pulses in a 500 Torr SF₆ atmosphere. The absorbance of the unstructured Si substrate is also shown for comparison.

4.3.3 The effect of HF treatment

A silicon oxide layer may be formed on the surface of structured Si during the irradiation process. A common way of removing the oxide from a Si surface is through HF treatment. In this section we investigate how the existence of this layer may affect the absorbance of the material by comparing the absorbance of the processed samples before and after HF treatment. Structuring in this case took place using the ps Nd:YVO₄ laser system ($\lambda=1064\text{nm}$, $\tau=12\text{ps}$) in a 250 Torr SF₆ ambient. We find the absorbance to be identical for the samples which did not undergo HF treatment and the ones treated with HF for 100 min at concentration of 10% (**Figure 4.6**). Independently of the laser fluence used, the way that the surface absorbs in the two cases remains practically unaltered, both for the UV/visible as well as for the below-bandgap wavelengths. These results demonstrate that the thickness of the oxide layer grown on the structured surfaces

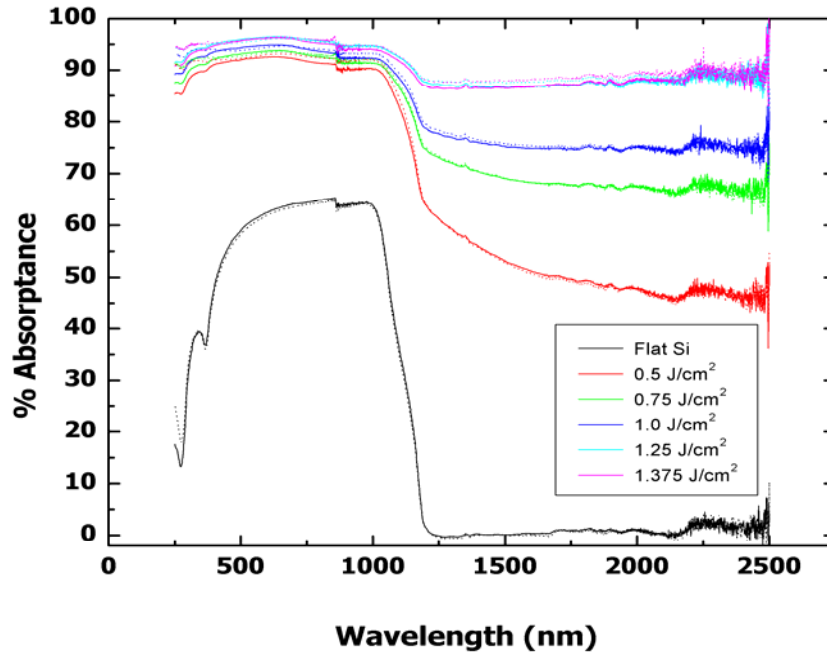


Figure 4.6: Absorbance of laser fabricated Si structures as a function of the wavelength for different fluences for samples treated with HF (solid lines) and for the untreated ones (dashed lines). All the samples were fabricated using 1000 pulses in a 250 Torr SF_6 atmosphere. The absorbance of the unstructured Si substrate is also shown for comparison.

upon laser irradiation, does not play any significant role in the absorbance of the samples.

4.3.4 The effect of laser pulse duration

Figure 4.7 shows the absorbance spectra of Si microstructures fabricated by using the 15 ns and 5 ps at 248 nm KrF laser system, in comparison to that of flat Si. Increased absorbance from 250 nm to 2.5 μm is observed for both samples structured; more than 90% for wavelengths below the crystalline Si band gap, and slightly less for NIR/IR wavelengths. In this regime the absorbance of the ns laser structured samples exceeds that of the ps ones.

The samples were irradiated in a 500 Torr SF_6 atmosphere, and were chosen because of their optimized aspect ratio, which could lead to more efficient trapping of irradiation and thus to enhanced absorbance. The irradiation parameters were 2.14 J/cm^2 ,

2000 pulse for the ns laser fabricated sample and 0.83 J/cm², 1000 pulses for the ps laser fabricated one.

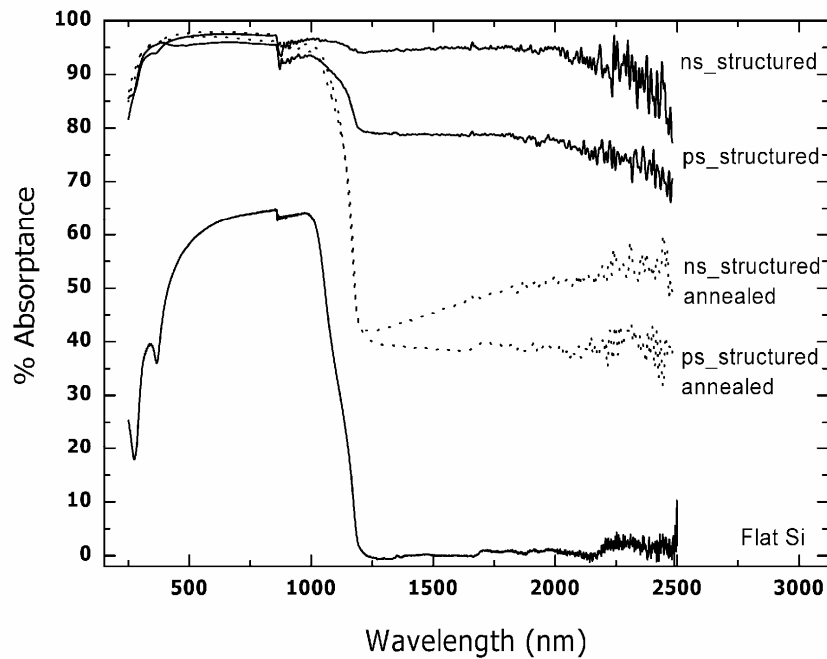


Figure 4.7: Absorbance of the ns laser and ps laser fabricated Si structures as a function of the wavelength, before and after thermal annealing at 600 °C for 90 min in vacuum. The absorbance of the unstructured Si substrate is also shown for comparison.

4.3.5 The effect of thermal annealing

It is important to note that increased absorbance by itself is not sufficient for the fabrication of a functional device. A critical parameter is responsivity, i.e. the ratio of the electrical output to the optical input; often, this may be poor. A common way to overcome problems associated with poor conversion of light in electrical output, is by thermal annealing.

Thermal annealing at 600 °C^[45] in vacuum for up to 120 min, does not change the visible absorbance of the samples. However the absorbance in the below-band gap spectral region decreases it significantly (**Figure 4.7**). Annealing in vacuum at 600 °C causes a drop in the observed absorbance for both samples. In the ps laser structured sample the absorbance curve is stabilized after 30 min of annealing, while for the ns case

90 min are necessary for reaching stabilization. Further annealing up to 120 min does not affect the absorbance curve observed in both cases. For the ps laser fabricated sample the below bandgap absorbance stabilized close to 40%. On the other hand the corresponding part of the curve of the annealed ns laser fabricated sample reveals a non-uniform annealing effect; the near band gap absorbance becomes markedly lower than for longer wavelengths, reaching up to ~55% at 2500 nm.

4.3.6 Discussion

For samples fabricated both in vacuum and in SF₆, and independently of the reactive gas pressure, there is an increased absorbance (close to 90 %) observed in the visible spectral range. The increased absorbance in the visible spectral range can be interpreted as a result of irradiation trapping between the intercone areas, leading to multiple reflections and thus to enhanced absorbance.^[45] This is in consistency to the observation that visible absorbance is not affected by annealing.

On the other hand, SF₆ appears to be crucial for the increased absorbance below-bandgap. An increase in the IR absorbance is observed when structuring takes place in vacuum, and becomes more pronounced with increasing incident laser fluence reaching a value of 35 % in the region 2000-2500 nm (**Figure 4.4**). This can be attributed to disordered material that can be formed upon laser irradiation of Si. Nevertheless, very high absorbance values in this spectral region can be reached when processing takes place in the presence of SF₆. The absorbance in the infrared spectral range, suggests an altered band structure associated with the introduction of sulphur impurity bands within the Si bandgap.^[45] A doping concentration of the order of 1%,^[71] can induce states within the Si bandgap. Then the absorption of photons with energies below the band gap of ordinary Si is enabled, making it possible for infrared light to promote electrons from these impurity states into the conduction band.

Thermal annealing decreases the below-band gap absorbance for both the ns and ps laser fabricated structures. This decrease can be most likely attributed to bond rearrangement within the Si matrix caused by annealing, rendering the sulphur impurities optically inactive.^[45] However the origin of the differentiation in the stabilization time of

the absorptance after annealing for the samples structured with different laser pulse duration is subject to further investigation.

4.4 Applications

The improved optical properties, make structured Si attractive for a number of applications such as photodetectors, infrared imaging, infrared microbolometers, as well as biomedical and chemical sensors.^[72] In many cases, thermal annealing is required in order to increase the responsivity of such systems. On the other hand, thermal annealing decreases the optical absorptance observed (e.g. **Figure 4.7**). Successful fabrication of functional devices can therefore be achieved through compromise between responsivity and absorptance optimization.

Mazur et. al ^[73] have recently studied the current–voltage characteristics and responsivity of photodiodes fabricated with Si that was microstructured by use of fs laser pulses in a sulphur-containing atmosphere. The photodiodes fabricated exhibit a broad spectral response (400–1600 nm), while optimized samples exhibit responsivities that are 2 orders of magnitude higher than those of commercial Si photodiodes in the visible and 5 orders of magnitude higher in the near infrared.

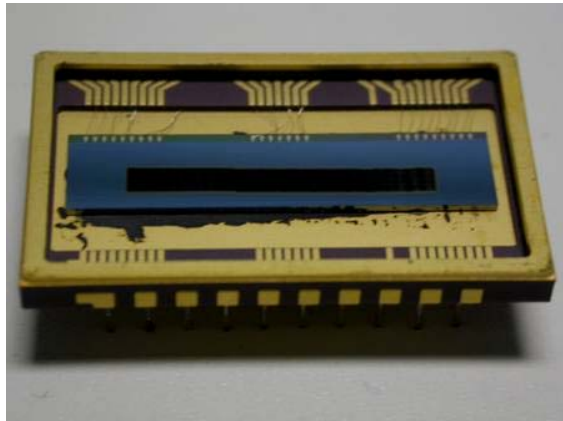


Figure 4.8: A fs laser (800 nm at 180 fs) structured back illuminated CCD circuit. Structuring took place in the presence of 500 Torr SF₆

These findings open up the possibility for exploiting laser fabricated laser fabricated Si structures in even more complex and systems, such as CCD circuits (**Figure 4.8**). Still, the main challenge is their commercialization. Processing time is a very important aspect in this case and laser processing using standard laser systems can be a time consuming process. The strategy to overcome this shortcoming is to use special high power-high repetition rate systems combined with fully automated scanning beam or sample processes. As we have shown in **Chapter 3**, it is possible to obtain high absorptance structures (e.g. **Figure 4.2**), while having minimized the processing time up to hundreds of times, by using the Nd:YVO₄ system.

4.5 Conclusions

Laser microstructuring in SF₆ is a very promising technique for tailoring the optical absorptance of Si. In particular we have found, under optimum conditions an absorptance over 90 % over a wide spectral range ($250 \text{ nm} < \lambda < 2.5 \text{ }\mu\text{m}$):

- The increased absorptance in the UV and visible is attributed to the irradiation trapping in between the high roughness cones, and is observed independently of the irradiation environment (even in vacuum).
- Significant below bandgap absorptance ($\lambda > 1100 \text{ nm}$) is observed only when SF₆ is used during the irradiation process. This is ascribed to the presence of S in the cone surface at high concentration as discussed in **Chapter 3**, which is capable of introducing impurity states or bands within the Si bandgap.

Chapter 5

Field Emission from Laser Structured Si

5.1 Introduction

Field-electron emission, otherwise known as cold cathode emission, is a form of quantum mechanical tunneling in which electrons pass through a barrier in the presence of an electric field. This phenomenon is highly dependent on both the properties of the material and the shape of the particular cathode, so that higher aspect ratios (height/tip radius) produce higher field emission currents at lower applied electric fields. Arrays of conductive or semiconductive structures, can be integrated in a large number of devices that utilize cold emission and ballistic transport of electrons from emitting cathodes to appropriate collector electrodes. Potential applications include field emission displays, ultrahigh-frequency power sources and amplifiers, high-speed logic and signal processing circuits, MEMS, electron microscopy and sensors.

A wide range of materials placed at different geometries have been considered as cold cathode field emitters. Metal-insulator-vacuum (MIV) structures,^[74] thin films,^[75] diamond and diamond films,^[76] graphite and graphite pastes,^[77] polymers,^[78,79] carbon fibres^[80] and nanotubes^[81,82,83] are some of the materials tested so far. The most familiar structure of a cold cathode field emitter is an array of microtips or Spindt tips named after Capp Spindt who first described the fabrication of these structures in 1968,^[84] based on lithography. This technology prompts well defined, high quality structures. The main

shortcoming of this technology is that it is a multi-step process involving clean room facility requirements.

When evaluating the potential of a new fabrication technology, several factors should be considered, such as how precise and reproducible it is, as well as how suitable it is for manufacturing emitter arrays over extended areas and for integrating with complementary circuits.^[85] Si based microtip emitters have attracted interest due to the existing wealth of knowledge of Si processing techniques that may also allow their easy integration to the existing Si technology. In addition Si is a material which can be easily doped, allowing for user-specified modification of its electrical properties.

An alternative approach to cold cathode field emitter manufacturing is the use laser irradiation of Si surfaces in the presence of a reactive gas, for the formation of high aspect ratio surface structures. This is a simple one-step production method of quasi-periodical micro-tip arrays yielding fairly reproducible average spacing, height and aspect ratio of the obtained microstructures, under conditions of reduced atmosphere.

A small number of studies on the field emission properties of laser structured Si have been performed. Evtukh et al.^[34] have fabricated structures using a Nd:YAG (1.06 μ m, 0.2ms) laser and have found a field emission threshold of the order of 20 V/ μ m. Shafeev et al.^[35] have also reported threshold fields as low as 4-5 V/ μ m for n-type microstructured Si, by a Cu vapor laser (510.6nm, 20ns). In both cases the samples were fabricated in air and their studies were limited to continuous emitting area geometries.

In this chapter we discuss the use of conical Si microstructures as potential field-electron emitters. We study the effect of the laser pulse duration used (15 ns, 5 ps and 500 fs at 248 nm) for processing Si in an SF₆ atmosphere, on their performance as cold cathode field emitters. Additionally large areas of uniformly shaped Si spikes and arrays of spots containing spikes have been fabricated using the Ti:Sapphire laser system (800 nm, 180 fs) and their structural and electrical properties have been examined in comparison. In all cases, the observed currents are correlated to localized field enhancement originating from the geometry of the spikes. Finally, we discuss the extend to which geometry can account for the observed emission results.

5.2 Fundamentals of Field Emission

Field emission refers to the emission of electrons from a solid cathode (generally in the shape of a sharp tip) into vacuum under the influence of a strong electric field.^[86] The pointed or conical shape of the cathode strongly enhances the electric field at the tip, originating from biasing the cathode negatively with respect to a nearby anode. Field emission occurs when electrons tunnel through the potential energy barrier at the interface between the cathode and the vacuum. This is in contrast with the more familiar phenomenon of thermionic emission, wherein electrons are emitted from a cathode when they acquire sufficient thermal energy to overcome this potential barrier.

5.2.1 Field-emission from a metal

In this section we review the fundamental theory of field emission as described by Gomer,^[86] and subsequently discussed by Busta.^[87] We first consider the case of field emission from a metal. The relevant energy level diagrams are shown in **Figure 5.1**, where the potential energy as a function of position for an electron near a metallic surface is shown for three different electric field regimes.^[87] Within the metal, energy states up to the Fermi energy E_F are occupied. In the vacuum, the lowest accessible level is at an energy $E_F + \Phi$, where Φ is the work function of the metal.

Figure 5.1 A shows the energy diagram for thermionic emission. In this case, the field there is very small, so no deformation of the energy barrier Φ takes place. Only electrons that acquire enough thermal energy from heating the emitter can overcome the barrier. At higher fields and still elevated temperatures, the barrier is deformed (the potential energy in the vacuum is now a linear function of distance from the metal-vacuum interface) and field dependant emission caused by barrier lowering due to the image charge takes place. This is shown in B and is known as Schottky emission.^[88] As the field increases, the barrier continues to become lower, but also narrower. Under specific conditions (concerning the material work function and the applied field), the barrier may become sufficiently narrow that electrons can tunnel through it, even at $T=0$ K. This is known as field emission and is shown by C.

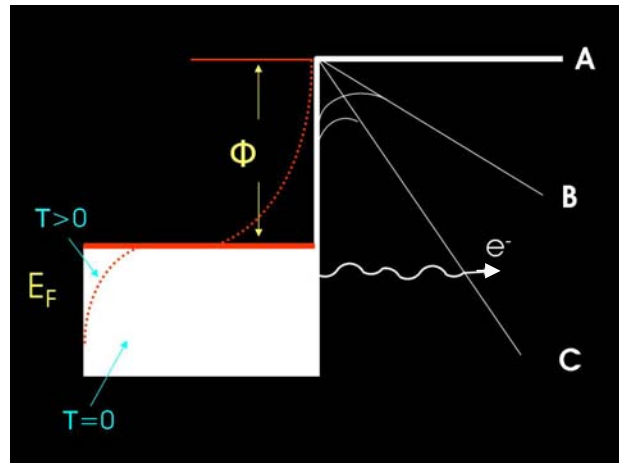


Figure 5.1 : Energy diagram for thermionic emission (A), Schottky emission (B) and field emission (C). The electron distributions in the emitter are plotted for the cases $T=0$ K and elevated temperature $T>0$ K. E_F is the Fermi energy of the metal and Φ is the barrier height or work function

A qualitative understanding of the tunnelling phenomenon can be obtained from the Heisenberg uncertainty principle. Supposing that the electrons can escape from the solid to the field-free vacuum along the x -direction and E_F is the energy at the Fermi level, the potential barrier a valence electron has to overcome in order to leave the material is:

$$E_B = E_F + \Phi - E_x \quad (\text{Eq. 5.1})$$

where E_x is the kinetic energy of the electron along the x -direction. In thermionic emission and photoemission^[10], where the surface potential has not been modified, the barrier is so high that tunnelling of electrons through it, is impossible. Therefore an electron needs to be given an energy equal to E_B in order to be emitted from the material. However in the presence of a very strong external electric field, \mathcal{E} , the width, ω , of the potential barrier is modified according to the equation:

$$\omega = \frac{E_F + \Phi - E_x}{\mathcal{E} \cdot e} \quad (\text{Eq. 5.2})$$

where e is the charge associated with a single electron. Small values of ω and E_B make it possible for the electrons to pass “through” the barrier (tunneling) rather than having to climb over it. An electron within the metal, with a kinetic energy of E_x due to its velocity in the x -direction, experiences a potential barrier at the metal-vacuum interface with height $E_F + \Phi - E_x$ and width $(E_F + \Phi - E_x) / \epsilon e$.

According to Heisenberg’s principle there is an uncertainty in defining the momentum, Δp , and position, Δx , of an electron, which is described by the well known equation:

$$\Delta x \cdot \Delta p = \frac{\hbar}{2}, \quad \text{with} \quad \hbar = \frac{h}{2\pi} \quad (\text{Eq. 5.3})$$

If we consider an electron with an energy near the Fermi level, the uncertainty in momentum stems from defining its energy, $E = (\Delta p)^2 / 2m$, within the energy gap Φ . For this energy uncertainty to result in a kinetic energy that equals the barrier height, the corresponding momentum uncertainty is $\Delta p = \sqrt{2 \cdot m \cdot \Phi}$, where E has been substituted by E_F , and m is the rest mass of the electron. According to **Eq. 5.3**, the corresponding uncertainty in position is:

$$\Delta x = \frac{\hbar}{2 \cdot \Delta p} = \frac{\hbar}{2 \cdot \sqrt{2 \cdot m \cdot \Phi}} \quad (\text{Eq. 5.4})$$

If Δx is greater or equal to ω , then there is a finite possibility that the electron will be found on either side of the surface of the material. Combining **Eqs. 5.2** and **5.4** the condition for field emission is roughly:

$$\frac{\hbar}{2\sqrt{2 \cdot m \cdot \Phi}} \geq \frac{\Phi}{\mathcal{E} \cdot e}$$

or

$$\mathcal{E} \geq \sqrt{\frac{8m}{\hbar^2 \cdot e^2}} \Phi^{3/2} \quad (\text{Eq. 5.5})$$

for an electron at the Fermi level.

However, a more detailed analysis of the probability for electron tunneling requires the application of more complex quantum mechanics. Implementing the Schrödinger equation in this one-dimensional motion of the electron, we have:

$$\frac{d^2\psi}{dx^2} + \frac{2 \cdot m}{\hbar^2} E \cdot \psi = 0 \quad (\text{Eq. 5.6})$$

inside the metal and

$$\frac{d^2\psi}{dx^2} + \frac{2 \cdot m}{\hbar^2} [E - (\Phi + E_F) + e \cdot x \cdot \mathcal{E}] \cdot \psi = 0 \quad (\text{Eq. 5.7})$$

outside the metal and within the potential barrier, where E is the kinetic energy in the x -direction and ψ is the wave function of the electron. These two equations are solved by applying the boundary conditions that ψ and $d\psi/dx$ are continuous at $x=0$. The solution inside the potential barrier is an attenuated wave and the tunneling probability (D) as a function of the electron energy E_x is given by:

$$D(E_x) = \frac{4[E_x \cdot (E_F + \Phi - E_x)]^{1/2}}{E_F + \Phi} \cdot \exp\left[-\frac{4}{3} \cdot \left(\frac{2m}{\hbar^2}\right)^{1/2} \cdot \frac{(E_F + \Phi - E_x)^{3/2}}{\mathcal{E} \cdot e}\right] \quad (\text{Eq. 5.8})$$

The emitted current density is found by multiplying this tunnelling probability by the rate of arrival at the barrier of electrons with energy E_x (Fermi-Dirac distribution), and then integrating over the energy range $0 \leq E_x \leq E_F$. The resulting equation, first described in 1928, is the Fowler-Nordheim expression^[89] (**Eq. 5.9**).

$$J = a_{FN} \cdot (\beta \mathcal{E})^2 \cdot \exp\left(-\frac{b_{FN}}{\beta \mathcal{E}}\right) \quad (\text{Eq. 5.9})$$

where $a_{FN} = \frac{A}{1.1 \cdot \Phi \cdot e^{\frac{9.84}{\sqrt{\Phi}}}}$ and $b_{FN} = 0.94 \cdot B \cdot \Phi^{3/2}$

with $A = 1.54 \cdot 10^{-6} \text{ AV}^{-2}\text{eV}$ and $B = 6.83 \times 10^7 \text{ Vcm}^{-1}\text{eV}^{-3/2}$. Finally β is the field enhancement factor ($\beta \geq 1$), describing the amplification of the electric field (e.g. on a sharp tip).

The Fowler-Nordheim equation is a useful tool for evaluating the origin of a given emission current (i.e. field emission, thermionic emission or even photo-emission). If the current emitted from the cathode is attributed to field emission, it is expected to follow the \mathcal{E} -dependence described in **Eq. 5.9**. Thus, we can plot $\ln(J/\mathcal{E}^2)$ vs. $1/\mathcal{E}$ and expect

a linear relation if the current J is the result of field emission. The values a_{FN} and b_{FN} can also be extracted from the slope and y -intercept of the linear Fowler-Nordheim plot.

5.2.2 Field-emission from a semiconductor

Field-emission from a semiconductor is described by a very similar theory to that for the field emission from a metal, as summarized above in the Fowler-Nordheim equation. But, the more complicated energy band-structure in a semiconductor leads to a few important modifications. **Figure 5.2** illustrates the energy states of the semiconductor near the semiconductor-vacuum interface.

When the penetration of the applied electric field is neglected, tunneling can occur from the valence band if the applied field is sufficiently intense as illustrated in **Figure 5.2 (a)-ii**. In this case, the current obeys the Fowler-Nordheim behavior, having however an effective work function $\Phi_{effective} = X + E_g$, X being the electron affinity and E_g the bandgap of the semiconductor. In the case when the conduction band is thermally or optically occupied, tunneling also takes place from the conduction band, but this is not usually the case.

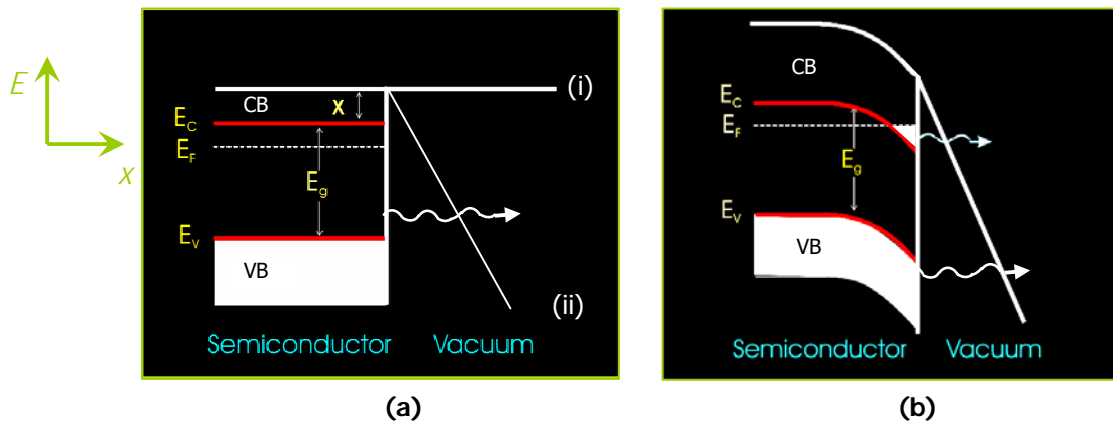


Figure 5.2: Potential energy of an electron vs. position near a semiconductor surface. Energy states of semiconductor near the semiconductor-vacuum interface: (a)(i) without an applied field, (ii) in the presence of an applied field and (b) in the presence of an applied field with its penetration into the surface taken into account. The conduction band is labeled CB and the valence band is labeled VB.

Still, if the penetration of the applied electric field into the semiconductor is taken into account, the picture becomes somewhat more complicated. The electric field in this case can cause the deformation of the potential experienced by the electrons (**Figure 5.2 (b)**). If the deformation is strong enough, the bottom of the conduction band is at a lower energy than the Fermi energy on the semiconductor side of the interface, and electrons accumulate in the dip in the conduction band. Tunneling must then be considered, and sequentially field emission, from two distinct groups of electrons, those in the valence band and those in the dip in the conduction band. Field emission attributed to the conduction band electrons follows Fowler-Nordheim behavior with an effective work function $\Phi_{effective} = X - (E_F - V_0)$, V_0 being the energy by which the bottom of the conduction band is shifted in the presence of the applied field. Clearly, the electrons in the altered conduction band can then tunnel through the barrier by a lower electric field than must be used to induce tunneling by the valence-band electrons. Thus, in some cases, two regimes of field-emission are considered for two regimes of applied field strength.

5.3 Field emission from laser structured Si

In the following sections we examine the effect of the laser pulse duration used for processing Si, on the performance of the resulting structures as cold cathode field emitters. Large areas of uniformly shaped Si spikes and arrays of spots containing spikes have also been fabricated and their structural and electrical properties have been examined in comparison. The extent to which geometry can account for the observed emission results is finally discussed.

We have used n type (phosphorous doped) Si (100) wafers with a resistivity of 2-8 Ohm cm.^[ii] Prior to electrical measurements, the samples were immersed in a 10% HF

^[ii] n-type Si prompts a shift of the Fermi level closer to the conduction band. Accordingly a lower applied field is required to commence field emission.

aqueous solution for 100 min in order to remove the oxide grown on the surface of the spikes. The distance between the Si spike tips and the anode was always set at least three times the height of the highest observable spike of each sample to ensure that the emission field is not influenced by the anode location.^[43] This distance was $d = 150 \pm 10 \mu\text{m}$ for the samples irradiated by 500 fs and 5 ps, 248 nm pulses as well as for the 180 fs, 800 nm pulses, while the distance was set at $d = 300 \pm 10 \mu\text{m}$ for the samples irradiated by 15 ns laser pulses at 248 nm.

5.3.1 The effect of laser pulse duration on field emission

In this section we study the influence of the laser pulse duration (15 ns, 5 ps and 500 fs at 248 nm) on the field emission properties of the structured Si surfaces. Among the fabricated samples (shown in **Chapter 3**), we have chosen those with the highest aspect ratio for each laser pulse duration used, since these are expected to exhibit the largest field enhancement. For those samples $2 \times 2 \text{ mm}^2$ areas were structured and subsequently tested as cold cathode field emitters.

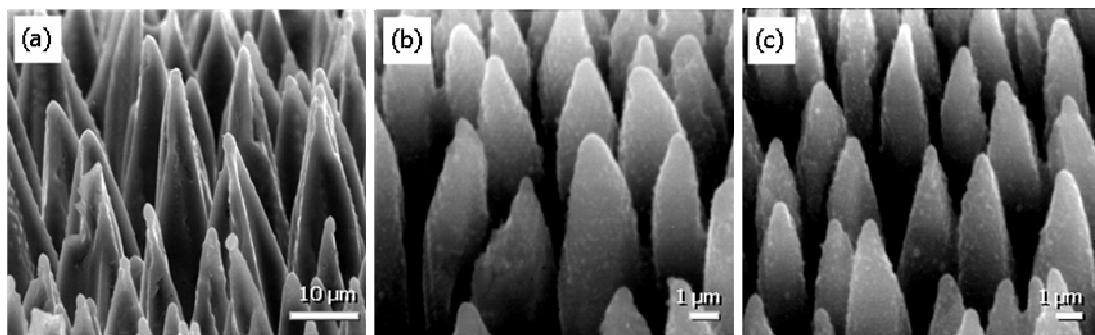


Figure 5.3 : Side SEM view of Si spikes formed on Si (100) using (a) a ns laser source (2.1 J/cm^2 , 3000 pulses @ 4 Hz, 500 Torr SF_6), (b) a ps laser source (980 mJ/cm^2 , 1000 pulses @ 4 Hz, 500 Torr SF_6) and (c) a sub-ps laser source (525 mJ/cm^2 , 750 pulses @ 4 Hz, 500 Torr SF_6).

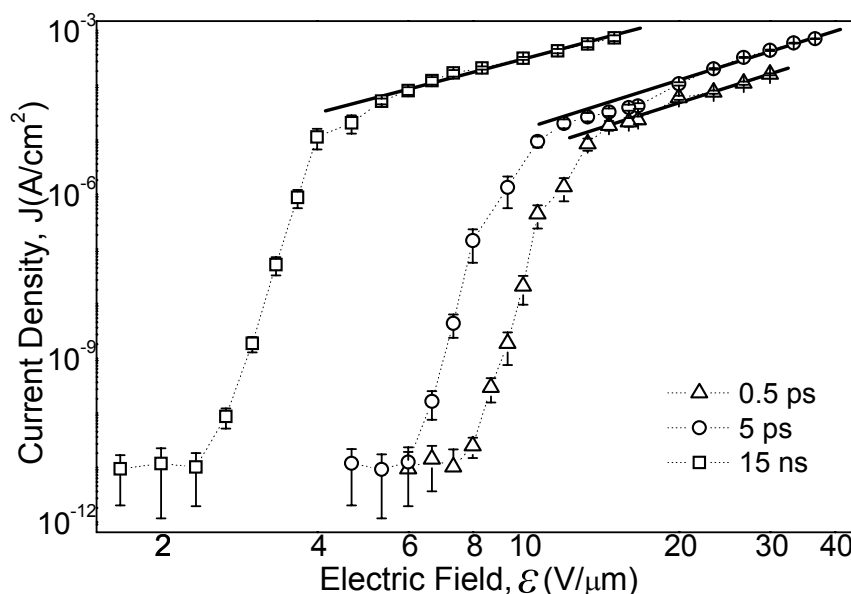


Figure 5.4 : Logarithmic plot of J - \mathcal{E} field emission characteristics for Si spikes formed using 15 ns ($\dots\Box\dots$), 5 ps ($\dots\Delta\dots$) and 500 fs ($\dots\circ\dots$) pulses. Error bars indicate current fluctuations after several conditioning runs. The solid lines denote best fits to the data within the high field saturation region.

Figure 5.4 shows a log-log plot of the current density – field (J - \mathcal{E}) emission characteristic curves of the samples as a function of the irradiating pulse duration at 248 nm. Error bars are a measure of the emission stability in each case. Current fluctuations are thought to be caused by ion bombardment and become more pronounced at increased background pressure.^[90] Three distinct regions are observed for all curves corresponding to the zero emission, field emission and current saturation regions respectively. Several emission cycles were taken in order for the J - \mathcal{E} curves to become relatively stable and reproducible.^[91] The first runs always exhibit a fast improvement effect to current emission, a phenomenon common for Si cathodes.^[91] The threshold field, which we define as the macroscopic average field where the emission current is 25 pA/cm², decreases as the irradiating pulse duration is increased. For the samples irradiated by 500 fs and 5 ps laser pulses the threshold field is ranging from 8 V/μm to 6 V/μm respectively. On the other hand, for the Si samples irradiated by 15 ns, 248 nm laser

pulses, the threshold field drops down to $2.5 \text{ V}/\mu\text{m}$, which is comparable to our previous results^[92] of $2 \text{ V}/\mu\text{m}$ using 50 fs , 800 nm laser pulses. This reveals that a lowest threshold could be achieved by a proper combination of laser wavelength and pulse duration. In any case the low threshold is a result of significant localized field enhancement attributed to the geometry of the spike tips.^[93] The increase of bias voltage above threshold dramatically increases the field emission current according to a Fowler-Nordheim (FN) tunneling process, until a saturation point is reached. In analyzing our field emission data we adopted the FN analysis,^[94] of field assisted tunneling (Eq.5.9).

Figure 5.5 shows FN plots of the field emission data for the samples irradiated by the 15 ns , 5 ps and 500 fs pulses. The solid lines represent linear fits of the data assuming a work function $\Phi = 4.1 \text{ eV}$ equal to the electron affinity of n-type c-Si.^[95] The corresponding enhancement factors β , determined from the slope of these lines, are also

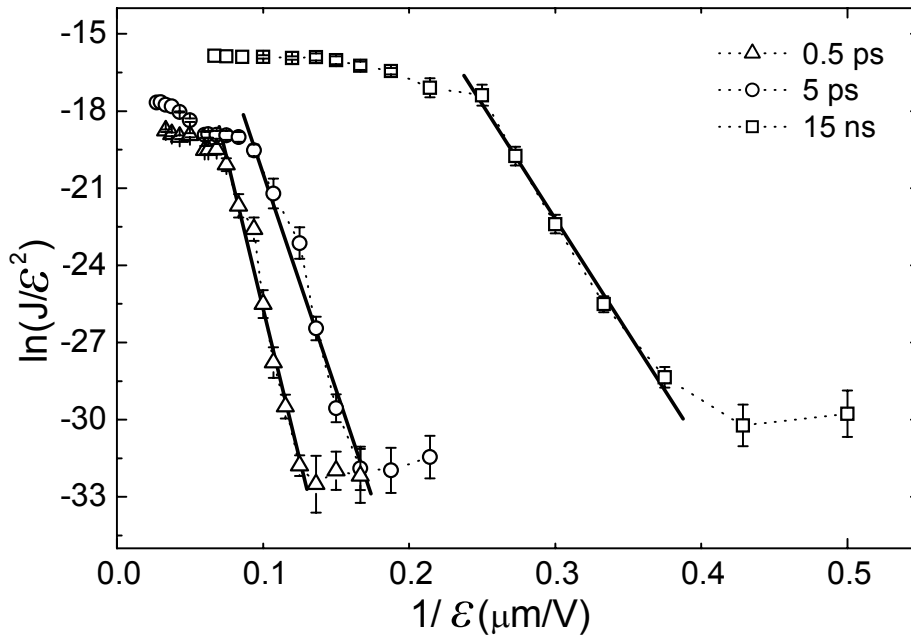


Figure 5.5 : The FN plots for the samples used in this study. (---□---) sample irradiated by 15 ns , (---○---) 5 ps , and (---△---) 500 fs pulses. The solid lines represent linear fits to the FN equation.

summarized in **Table 5.1**. It can be seen that the sample structured using 15 ns pulses has the highest enhancement factor which is compatible with the lower emission threshold observed. Therefore the lower the emission threshold the higher the enhancement factor obtained.

Pulse Duration ($\lambda=248$ nm)	typical tip radius (nm)	Spike height (μm)	Spike average period (μm)	Spike Density (spikes/ cm^2)	Thresh			
					old Field (V/ μm)	β	β_{single}	$\beta/\beta_{\text{single}}$
15 ns	670 ± 120	65 ± 5	11 ± 4	4.3×10^6	2.5	600	77 ± 15	8 ± 2
5 ps	470 ± 110	10 ± 2	5.5 ± 1.5	4.3×10^7	6.0	280	23 ± 7	12 ± 4
500 fs	530 ± 200	8 ± 1	5 ± 1.3	5.5×10^7	8.0	210	17 ± 7	12 ± 5

Table 5.1 : Morphological characteristics and field emission properties of the microstructured Si surfaces. The \pm values denote the standard deviation of each measured or estimated quantity.

For a single isolated spike the field enhancement factor β depends on the spike height, h and on the tip radius, r .^[93] According to a simple model^[96] the far field value of the enhancement factor of a single isolated spike can be fit as $\beta_{\text{single}} \approx 5.93 + 0.73(h/r)$ for $100 < h/r < 500$, and $\beta_{\text{single}} \approx 2 + h/r$ for $h/r < 40$. The corresponding theoretical values for the three types of samples, estimated using the mean spike height and tip radius, are listed in **Table 5.1**. Although, the theoretically estimated enhancement factor values (β_{single}) are considerably lower than the experimental (β) ones their ratio $\beta/\beta_{\text{single}}$ remains fairly constant. The difference between the experimental and the calculated values can be attributed to the presence of narrow, possibly nanometer sized, highly conducting channels within low conducting material at the apex. Scanning tunneling field emission (STFEM) maps of Si spikes have revealed emission from such nm sized channels suggested to be pure Si in an actual SiO_2 matrix.^[35,36] Likewise, the statistical variation of the morphological characteristics of the Si spikes inhibits the accurate estimation of the local field at one emitter. The latter may be considerably reduced^[97,98,99] due to the

presence of neighboring spikes especially for the case of denser arrangements exhibiting low average spatial periods. On the other hand, the theoretical model correctly predicts that the samples irradiated by the 15 ns laser pulses should be better field emitters than those irradiated by the 5 ps and 500 fs laser pulses respectively. The enhanced field emission in this case is mainly due to the fact that although the tip radius is slightly increased, the spike height is dramatically increased in the case of 15 ns pulses.

5.3.2 Continuous areas vs. spot arrays of Si emitters

Figure 5.6 shows SEM pictures of a regular array of spots fabricated using a Ti:Sapphire laser source (800nm, 180 fs) in a 500 Torr SF₆ atmosphere. Each spot has an elliptical shape with major and minor axes of 250 μm and 170 μm respectively. It contains Si microstructures with height up to 5 μm (at the center of the spot), and an average density of approximately $2.5 \times 10^7/\text{cm}^2$. The spatial period distribution of the spikes formed is shown in **Figure 5.6 (d)** in comparison with the corresponding distribution of a large area formed by overlapping exposures. The distribution in the spot is found to be wider than that of the large area due to the non-uniform (Gaussian) laser energy beam profile; **Figure 5.6 (b)** reveals that the density of the spikes increases from the center of the spot towards the perimeter in accordance to the decrease of the laser fluence. The average spike height is decreased in the direction of the density increase. The most probable value of the distance between neighboring spikes decreases to 1.4 μm, for the spots, compared to the 4.4 μm achieved with overlapping. A corresponding decrease of the most probable spike height is also anticipated.

The array shown in **Figure 5.6 (a)** is an alternative approach to the fabrication of functional Si cold cathodes based on the selective fabrication of spots of field emitters rather than a large continuous emitting area. This process is faster and very effective, since no rastering of the beam across the whole sample is required. It is also closer to the requirements of the field emission device industry, since each one of these spots could possibly operate as a pixel in a functional Si based field emission display (FED). The achieved pixel size corresponds to a spatial resolution compatible to the current standards

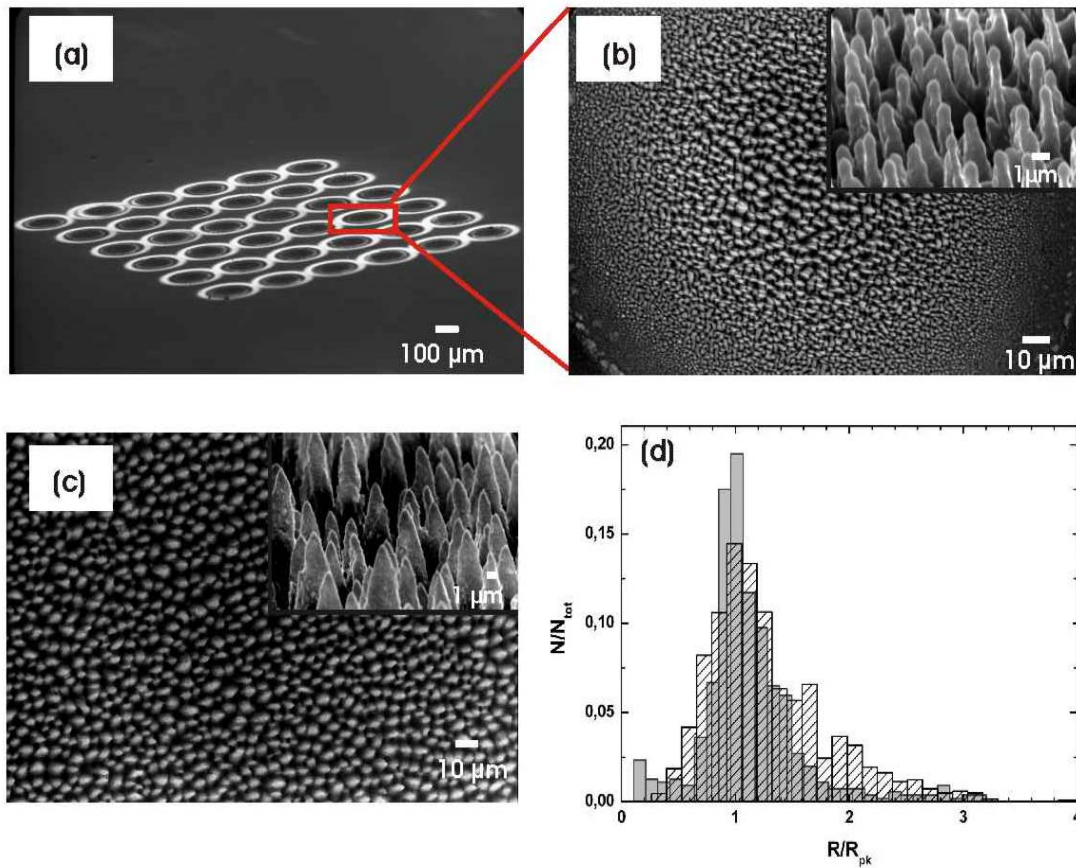


Figure 5.6 : (a): SEM image of a regular array of spike covered spots fabricated with 180 fs - 800 nm laser pulses in a 500 Torr SF_6 ambient. The laser fluence was always 0.6 J/cm^2 and the number of pulses was 1800 per spot. The laser repetition rate was 1kHz. (b): Top-view image of a spot. The spike morphology at the centre is shown in the inset. (c): Top-view and spike morphology images of the corresponding sample prepared under overlapping exposures and (d): Spatial period distribution of the Si spikes formed inside the spot (hatched bars), in comparison with the distribution observed in the overlapped sample (filled bars). The spikes population, N and the corresponding period values, R are normalized to the total number of spikes, N_{tot} and to the most probable average period, R_{pk} , respectively. R_{pk} is $1.4 \mu\text{m}$ and $4.4 \mu\text{m}$ for the spot and the overlapped sample respectively.

of the flat panel display industry, which is of the order of $100 \mu\text{m} / \text{pixel}$. (see following section).

Figure 5.7 shows a log-log plot of the current density – field (J - \mathcal{E}) emission characteristic curve of the regular array sample shown in Figure 5.6. The three regions

can again be distinguished. Error bars indicate the measured emission stability. Interestingly, both curves shown in **Figure 5.7** result in similar high field saturation current densities. Therefore effective emission is not limited by the size of the structured area. This is a particularly desirable feature in a wide range of relative applications.

Similar to the samples fabricated under 500 fs pulses at 248 nm, the array exhibits a threshold field of ~ 6.7 V/ μm . This value is higher than the threshold of ~ 5.3 V/ μm of the large area sample prepared under the same conditions. This is expected mainly by the higher average spike period and, to a smaller extent, by the smaller width of the corresponding distribution for the overlapped sample. Both these characteristics comply with a much more homogeneous arrangement of sharper and thus more field-effective

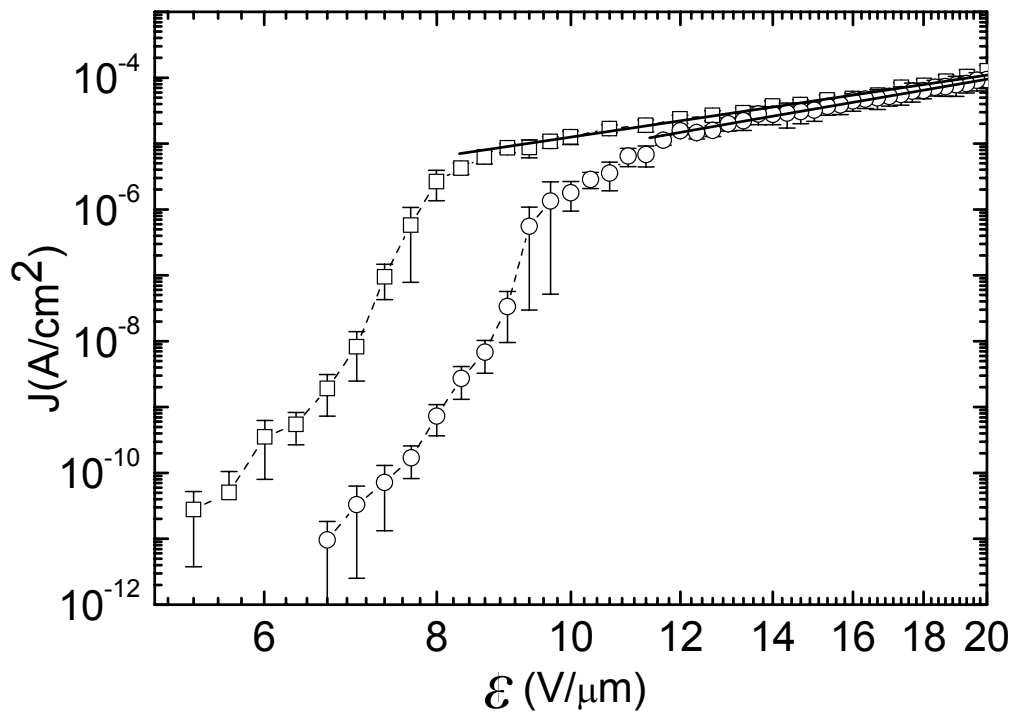


Figure 5.7 : Logarithmic plot of the J - E field emission characteristics for the Si spike array of Figure 5.6 (a) (open circles). The J - E curve of the corresponding large area sample, formed by overlapping laser exposures, is also shown for comparison (open squares). Both samples were prepared using 180fs - 800nm laser pulses. Error bars indicate current fluctuations after several conditioning runs.

spikes compared to the array spots. A low emission threshold is desirable for device applications.

Saturation of field emission of the Si spikes is observed in the current density after a certain macroscopic electric field as shown in both **Figure 5.4** and **Figure 5.7**. In this region of the J - \mathcal{E} curve the current density always follows a $J \propto \mathcal{E}^n$ law, with n varying from 3.0 to 3.5. This high exponent power-law dependence has been previously observed in Si needle structures and it has been suggested that only a space charge limitation can account for it.^[91] A charge trapping mechanism has been identified in field emission from diamond-like carbon films with scanning probe techniques^[100] and is characteristic of a trap-governed electron transport that occurs in some part of the solid and governs the observed current. This part may be the disordered layer known to exist below the surface of Si spikes [see **Chapter 3**]. An exponent greater than two can then originate either from some geometrical effect having to do with the 3-D geometry of the tips, or from a steep exponential trap distribution within the forbidden energy gap of the semiconductor.^[101]

5.4 Applications

Devices based on field emission feature many desirable characteristics. Field emitters can produce electron beams with high brightness and current density while operating at low voltages and consecutively consuming relatively little power. They can be integrated into small, lightweight devices and can be operated at high repetition rates due to their rapid on/off switching speed. Applications of field emission either from single tips or arrays include its use as an electron source in MEMS, electron microscopy and as previously mentioned in field emission displays.

Field emission displays are thin, flat cathode ray tubes consisting of two-dimensional matrix electron sources (the pixels), which illuminate a monochromic or full-colour screen. Each pixel has about a thousand tips (a density of $10^6/\text{cm}^2$). The first FED to work at television data rates was demonstrated by in 1991, while full colour version appeared two years later. In recent years they have received renewed attention,

with companies like Samsung^[102] and Canon actively researching. In fact, Sony plans to release in the market up to 30 inch FED televisions in the next couple of years.^[103]

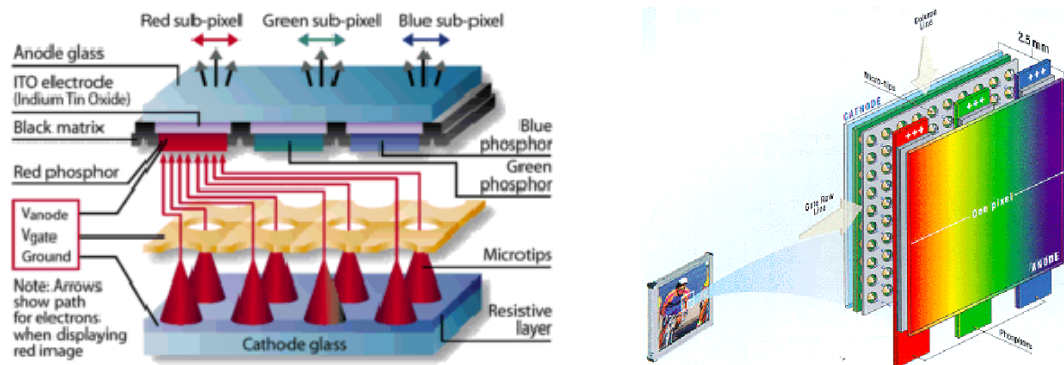


Figure 5.8 : The Field Emission Display principle of operation.

The advantage of this technology, apart from requiring less power, is that the displays are thin and light. Although it has the optical quality of a cathode ray tube, it does not produce X-rays, nor is it sensitive to magnetic fields or large temperature variations. For all of these reasons it can find wide range of applications in industrial and automobile applications or as monitor for scientific and medical instruments (such as mass spectrometers or oscilloscopes). Versions have also been developed for avionics and this technology could possibly be considered for manned space applications.

5.5 Conclusions

Laser structuring in the presence of a reactive gas is an efficient technique for fabricating Si based cold-cathode field-electron emitters. In particular, in this chapter:

- We have studied the effect of laser pulse duration on field emission of Si, irradiated by a UV laser in the presence of SF₆ reactive environment, to find that spikes fabricated under ns pulses outperform those fabricated with shorter pulse durations both in terms of geometry and of emission characteristics.

- Furthermore, we have demonstrated the feasibility of fabricating Si spike emitters for practical applications such as cold emission arrays, through a maskless process.

In each case, the resulting morphologies have electrical characteristics appropriate for cold cathode applications with a field emission threshold down to a few V/ μm , a value comparable to those observed in carbon nanotubes. Finally, of special interest from an application point of view, is the finding that effective emission is not limited by the size of the area of the emitters.

Chapter 6

Wetting Properties of Laser Structured Si

6.1 Introduction

The control of the wetting properties of surfaces, and particularly the possibility of inducing superhydrophilic and superhydrophobic behavior (the so-called “Lotus effect”^[104]) by micro-nanostructuring is arising an increasing interest for a wide range of applications, such as, self-cleaning surfaces, biological scaffolds, microfluidics, lab-on-chip devices, water proof coatings for automotive and aerospace vehicles, textiles.^[105,106,107] Nature has illustrated a wide variety of superhydrophobic surfaces. Insects like *Cicada orni*^[108] and *Rhinotermitidae*^[109] and plants such as the sacred lotus (*Nelumbo Nucifera*)^[104] exhibit unique wetting properties. In fact the lotus leaf surface has been considered as a “model” superhydrophobic, water repellent surface. The properties of the lotus leaf have been ascribed to the complex morphology present on its surface, consisting of hierarchical structuring, at two different lengthscales (see **Chapter 6.4**). As a consequence, the main strategy for the fabrication of any artificial superhydrophobic and water-repellent surface has been to mimic its surface topology. Simplified schemes of micro-nanomanufacturing, enabling the reproducible creation of such complex surface topologies with different lengthscales are therefore very desirable.

Several different physical and chemical patterning approaches have been employed for structuring surfaces, so as to tailor their wettability, including photolithography,^[110] templated electrochemical deposition,^[111] plasma treatments,^[112]

electron-beam lithography,^[113] and selective growth of carbon nanotubes.^[114] Microstructuring by lasers in specific ambient environments is particularly attractive, because it may result into structuring of solid substrates at two length scales through a simple one-step production, without a clean room facility and high-vacuum equipment requirements. The Si surface obtained^[115] consists of self-organized conical spike forests with characteristic size from a few to tens of μm , decorated by fine features between tens and a few hundreds of nm. Among the advantages of this technique, is that it can be applied in a wide range of materials, such as polymers^[18,116] ceramics,^[18] or metals^[23] in order to control surface topology, and thus open the way to controlling their wettability.

Recently the wetting properties of laser structured Si have been addressed.^[39, 115] Mazur et al.^[39] have studied the wetting properties of laser structured Si coated by fluoroalkylsilane molecules. This study however, was limited to static contact angle and some hysteresis measurements.

In the present work we systematically study the wetting response of Si surfaces structured using the Ti:Sapphire fs laser source ($\lambda=800$ nm, $\tau=180$ fs). In particular:

- Using fs laser structuring we are able to fabricate Si based surfaces exhibiting double-lengthscale roughness. Tuning of the wetting response of Si, from initially hydrophilic to hydrophobic, may be achieved through this process without any additional surface coating. These properties can be exploited for inducing spontaneous motion of liquids; we demonstrate that it is possible to drive drops to ascend a structured Si surface, tilted at any angle by fabricating a proper texture gradient on it.
- By incorporating a second step in the fabrication process, the deposition of chloroalkylsilane monolayers, we are able to fabricate superhydrophobic structured Si surfaces with both apparent contact angle and hysteresis comparable to that of the lotus leaf. Water droplets can move along the irradiated superhydrophobic surfaces, under the action of small gravitational forces, and experience subsequent immobilization, induced by surface tension gradients.
- We study the water repellence of the superhydrophobic structured Si samples and directly compare them to the lotus leaf, to find striking similarities in the overall

water repelling performance i.e. the velocity threshold for repulsion, the elasticity of the shocks and the wetting behaviour at high velocity regimes.

- We achieve dynamic control of the wetting behavior of liquid drops by using an electrowetting-on-dielectric system based on unstructured and structured Si. Significant contact angle changes can be observed on such surfaces, upon the application of small electric fields.
- Finally, we are able to dynamically tune the wetting response of the structured Si surfaces from an initially hydrophobic to hydrophilic state by exposure of the system to organic solvent vapours (chemically induced wetting).

6.2 Fundamentals

6.2.1 Young's Equation

A small droplet of a liquid deposited on a surface either forms a spherical cap shape with a well-defined equilibrium contact angle θ to the solid or it spreads across the surface until it forms a wetting film. The shape of the drop is described through the precise equilibrium that results from the balance between the surface tensions (γ) at the three-phase contact line formed along the solid–liquid, liquid–gas and solid–gas interfaces. The force balance leads to the well-known Young equation:

$$\gamma_{lg} \cos\theta_o = \gamma_{sg} - \gamma_{sl} \quad (Eq. 6.1)$$

where the subscripts (sg), (sl), and (lg) refer to solid-gas, solid-liquid, and liquid-gas interfaces respectively (**Figure 6.1**). The angle at which a liquid-gas interface meets the solid surface is called the equilibrium or Young contact angle (θ_o) and for this, the energy of the system reaches a local minimum. ^[117,118,119]

The contact angle is a measure of the wetting behavior of a given surface and depending on its value a surface can be characterized as hydrophilic ($<90^\circ$) [**Figure 6.1 (a)**] or hydrophobic ($>90^\circ$) [**Figure 6.1 (b)**]

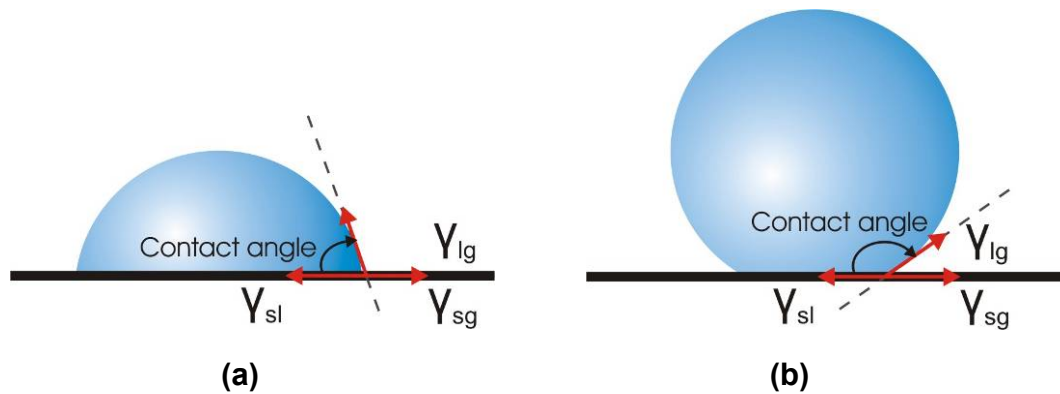


Figure 6.1 : A sessile liquid drop on (a) a hydrophilic and (b) a hydrophobic surface

Surface tension is a manifestation of the intermolecular forces at a surface (or interface) and is defined as the energy (W) needed to increase the surface area per increase in surface area (A):

$$\gamma = \frac{dW}{dA} \quad (\text{Eq.6.2})$$

High interfacial surface energy for the liquid-solid results in a large contact angle, i.e. the higher the surface tension of the liquid, or the lower the surface energy of the substrate, the larger the contact angle. With water, typically the most hydrophobic flat solids can achieve up to $\theta \sim 120^\circ$. In order to obtain an even more hydrophobic surface, structuring which will increase its overall roughness is required. The enhancement of the hydrophilic or hydrophobic character of a surface upon structuring is reviewed in the following section.

6.2.2 Wettability and Surface roughness: Wenzel and Cassie Baxter states

The effect of the macroscopic surface roughness on the wettability of surfaces has been theoretically approached by two different models. In the Wenzel model ^[120], the liquid is assumed to completely penetrate within the entire rough surface, described as

“homogeneous wetting regime” without leaving any air pockets underneath it (**Figure 6.2 (a)**). The apparent contact angle, θ_w , is then given by the following equation:

$$\cos\theta_w = r \cos\theta_o, \quad (\text{Eq.6.3})$$

where r is the ratio of the unfolded surface to the apparent area of contact under the droplet, and θ_o is the contact angle on a flat surface of the same nature as the rough (Young contact angle). Since r is always greater than unity, this model predicts that the contact angle will decrease / increase with surface roughness for an initially hydrophilic ($\theta_o < 90^\circ$) / hydrophobic ($\theta_o > 90^\circ$) surface.

In contrast, Cassie and Baxter (CB) assumed^[121] that the liquid does not completely permeate the rough surface because air gets trapped underneath it (“heterogeneous wetting regime”). As a result a droplet will form a composite solid-liquid / air –liquid interface with the sample in contact, and the effective surface energy of the scaffold below the water will be dominated by air. In this case, the apparent contact angle, θ_{CB} , is an average of the flat surface, θ_o , and the value for full hover over the flat surface (that is, 180°) and is given by^[121,122]:

$$\cos \theta_{CB} = -1 + f + r_f f \cos \theta_o \quad (\text{Eq.6.4})$$

In the above expression, θ_{CB} is the Cassie-Baxter contact angle, f is the fraction of the projected solid surface that is wet by the liquid, and r_f is the roughness ratio of the wet area.

When the liquid drop is lying on the top of the rough surface without sinking into the features at all (**Figure 6.2 (b)**), the roughness factor will equal one ($r_f=1$) and **Equation (6.4)** becomes the widely used simplified form of the Cassie-Baxter equation.

$$\cos \theta_{CB} = -1 + f(1 + \cos \theta_o) \quad (\text{Eq.6.5})$$

As f is always lower than unity, this model always predicts enhancement of hydrophobicity, independently of the value of the initial contact angle θ_o . The lower the value of f , the higher the contact angle measured.

In contrast, when $f=1$ and $r_f=r$, **Equation (6.4)** turns into the Wenzel equation.

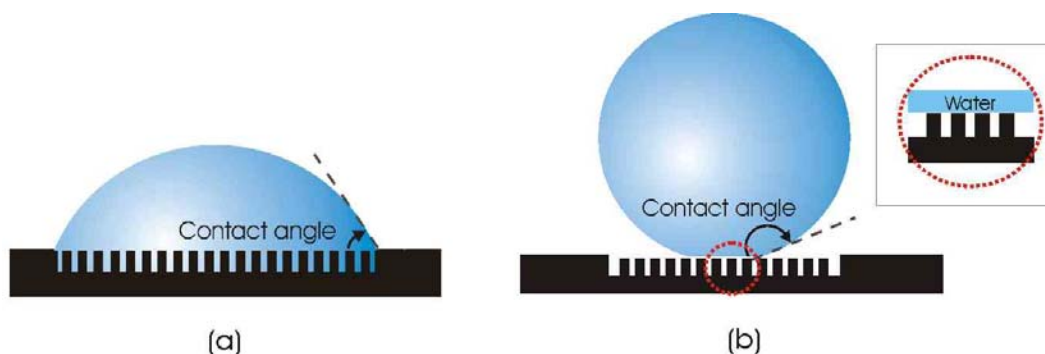


Figure 6.2: A liquid drop (a) in the Wenzel state, where the drop fills the recessed areas and (b) in the Cassie-Baxter state, where air pockets are trapped beneath it, minimizing the surface area of the solid in contact with the liquid.

6.3 Hydrophobic laser structured Si surfaces

Laser structuring of Si in a reactive gas (SF_6) atmosphere, can greatly enhance the overall roughness of its surface. This makes it possible for the initially hydrophilic Si surface to become hydrophobic upon laser structuring. **Figure 6.3 (a)** and **(b)** shows the static contact angles of $3\ \mu\text{l}$ nanopure water drops in contact with flat (66°) and structured Si ($>140^\circ$) surfaces respectively.

The structures were fabricated using the Ti:Sapphire laser source, with SF_6 used as the reactive gas. Prior to the wettability measurements shown in this section, all the samples were immersed in a 10% HF aqueous solution, in order to remove the oxide grown on the surface during the laser irradiation process.

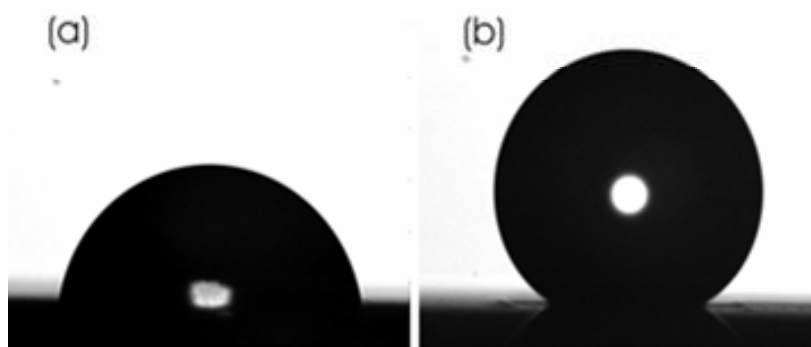


Figure 6.3: Apparent static contact angles of a $3\ \mu\text{l}$ nanopure water drop in contact with (a) an unstructured Si surface and (b) a fs laser structured Si surface in the presence of SF_6

6.3.1 Morphology and Static Contact Angle Measurements

In this part of our work we study the effect of different surface morphologies on the wettability of processed Si. Textured Si surfaces have been fabricated by employing the same number of laser pulses (an average of 500) at different fluences (**Figure 6.4**). Increasing the incident energy per unit area causes remarkable changes in the structures shape, dimension and density. At low irradiation fluences laser heating induces melting of the surface producing a rippled landscape, with structures not completely physically separated (**Figure 6.4 (a)**). Upon increasing the fluence (**Figure 6.4 (b) and (c)**), conical microstructuring is promoted on the Si surface, with structures becoming more pronounced and spatially separated. In this regime the average spikes spacing, base diameter and height increase with laser fluence. For larger fluence values (above $\sim 1.0 \text{ J/cm}^2$), the spikes growth reaches a plateau, where the base diameters stabilize around $8 \mu\text{m}$, while the height stabilizes around $15 \mu\text{m}$.

Besides directly affecting the micrometer-scale surface topology, increasing fluence is also crucial to induce a more pronounced sub-micrometer decoration on the spikes walls. In particular, the protrusions with size from tens to a few hundreds of

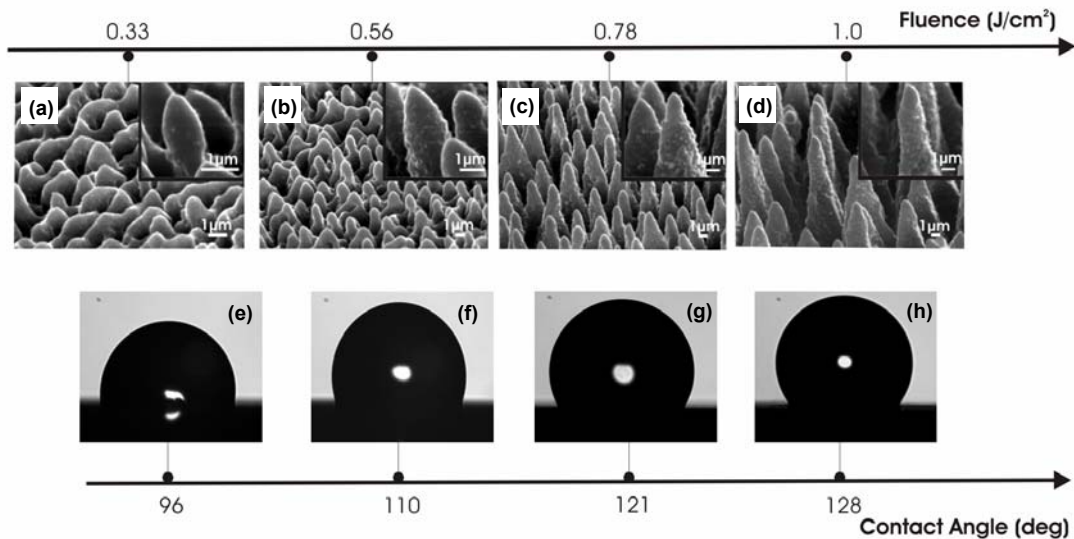


Figure 6.4 : (a)-(d) Side scanning electron microscope view of Si surfaces structured by fs-irradiation at different laser fluences. The insets are higher magnifications of the obtained structures. (e)-(h) Photographs of water droplets on the corresponding structured Si surfaces.

nanometers, which constitute the second length-scale pattern on the Si surface, become more evident as the laser fluence increases (insets of **Figure 6.4 (c)** and **(d)**). The micrometer-scale conical features together with the nano-scale features generated by the surface prongs on the cones result into a significant increase of the overall roughness. Some pictures of the water drops lying on the structured Si surfaces are shown in **Figure 6.4 (e)-(h)**. **Figure 6.5** presents the fluence dependence of both the spikes density on the textured surface and the sessile drop ($2\ \mu\text{l}$) contact angle resulting from the engraved topology. For fluence values ranging from 0.17 to $1.0\ \text{J}/\text{cm}^2$, the spikes density decreases fairly linearly, and then saturates at about $10^6/\text{cm}^2$. Correspondingly, the contact angle stabilizes around 131° , for irradiation fluence values greater than $1.0\ \text{J}/\text{cm}^2$. It is evident that the laser-assisted texturing of the Si surface induces a remarkable change in the wettability features of Si, as it affects the overall surface topography in a systematic manner. However, further investigation is required in order to clarify the relative contribution of the two-lengthscale roughness on the observed wetting behavior.

Changes in the observed wettability may be attributed to a synergy of surface chemistry and roughness. Chemical analysis of the Si microstructures produced by

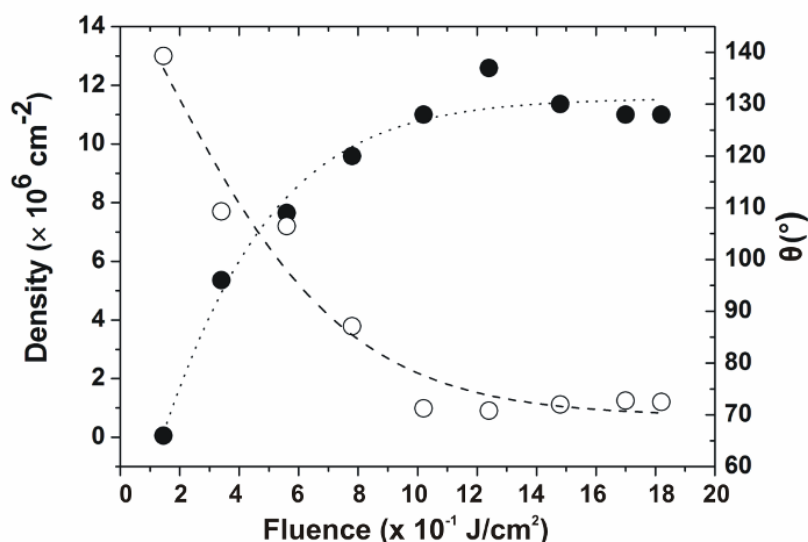


Figure 6.5: Experimental plot of spike density (empty dots) and the static water contact angle, θ (full dots) on the structured Si, versus fs laser irradiation fluence. The dotted and the dashed lines are guides for the eye.

irradiation with fs laser pulses under similar conditions to those employed in the present work has been reported by Crouch et.al.^[45,123] Following a detailed study of the structured Si composition and crystallinity, these authors have shown that the fabricated cones consist of a crystalline Si core covered by a disordered S doped Si layer, a few hundred nanometers thick, in agreement to our findings shown in **Chapter 3**, but for a different laser source. For the laser fluences they employed, which are similar to those used in the present experiments, the thickness of this disordered layer was found to remain almost unaltered. Also the dopant (S) concentration did not change significantly and was always less than 1%. Furthermore it is known that the formation of a native oxide layer is initiated on the Si surface immediately after the HF treatment.^[124,125] Its thickness changes very slowly in the first few hours (an increase of $\sim 2\text{\AA}$ in the first hour).^[124] Particular care was given in our experiments, in performing the contact angle measurements only a few minutes after the HF treatment, therefore ensuring the presence of similar native oxide thicknesses in all the samples. Based on the above findings, the structured Si surfaces are considered to maintain a similar chemical composition and the observed changes in the wettability may be attributed primarily to the morphological changes obtained at different laser fluences.

In order to further elucidate the contribution of the overall surface chemical composition on the wetting properties, we performed two different sets of contact angle measurements. First, we compared the water contact angles formed on flat c-Si surfaces with different levels of doping, after HF treatment. In the second set of experiments we compared the contact angles formed on flat heavily P doped (100 ppm) a-Si samples to that of c-Si, also after HF treatment. In all cases a similar contact angle of $\sim 70^\circ$ was measured. These results indicate that the surface composition has a minor contribution in the wetting properties we observe.

Previous studies in which initially hydrophilic surfaces became hydrophobic upon structuring, were based on the deposition of a hydrophobic coating on the top of the structure.^[126] On the contrary, the results of this work demonstrate that a Si surface upon patterning becomes hydrophobic, without any need for coating deposition. The results of this work clearly demonstrate that Si hydrophobicity increases upon laser structuring, and this behavior can be described assuming that air pockets are trapped underneath the

liquid. **Eq. 6.4**, which describes this behavior, can give quantitative information about the partial penetration of the water drop into the formed Si features. For the samples exhibiting the pronounced two-lengthscale surface roughness, namely those obtained by irradiation fluences larger than 1.0 J/cm^2 , the contact angle values reach a plateau around 131° (see **Figure 6.5**). Therefore, for these samples the liquid is in contact with a practically constant solid surface, and thus, the factors f and r_f in **Eq. 6.4** remain constant. Assuming that at these irradiation regimes the formed structures roughly resemble cones (the nanometer scale formed features are integrated into the cone structure), a simple geometric equation correlates the factor r_f with the angle of the formed cones, which is evaluated by the scanning electron microscopy pictures. Finally, by **Eq. 6.4** the factor f is calculated ~ 0.13 . Namely, the surface of the base of the wetted Si cone is about 13% of the total base of the formed Si cones (**see Appendix**).

In order to quantify the relative contribution of the second lengthscale structures to the wettability of structured Si, we have treated this type of roughness separately. An estimation of the density of the smaller scale structures per area unit was made, using high magnification SEM pictures combined with an image processing algorithm. The second-lengthscale structures which are observed under high magnification SEM images (insets of **Figure 6.4** (a)-(d)), and are expected to contribute to the overall roughness, have a radius of the order of $\sim 50\text{nm}$. By treating these smaller scale structures as hemispheres, we have found that the overall roughness ratio of the wet area increases with laser fluence, reaching up to $\sim 12\%$ at the plateau region, in comparison to the macroscopic cone roughness. By incorporating this value into the Cassie–Baxter equation we have found a decrease of the fraction of the projected solid surface that is wet by $\sim 7\%$ (**see Appendix**). This indicates that the second scale roughness contributes to some extent to the overall roughness and consequently to the wettability of the Si surface.

6.3.2 Manipulation of liquids by using surface tension gradients

It is known that a gradient in surface tension can induce a net motion of a liquid drop on a surface. Such flow arising from the action of a surface tension gradient can be created by several approaches, including thermal,^[127] chemical,^[128] electrochemical^[129] and light driven methods.^[130] The present results pave the way to the possibility of designing and fabricating specific textures on the Si surface, in order to induce anisotropic wetting and spontaneous motion of liquids, even uphill.

To achieve a surface tension gradient on the Si surface we have structured a series of successive regions at different laser fluences, which correspond to different morphologies, thus inducing a wettability gradient. A Si surface structured in this manner is shown in **Figure 6.6 (a)**. On this surface, which was fabricated by varying the fs irradiation fluence from 0.33 to 1.0 J/cm², we could observe a displacement of the center of mass of a water drop (4 μl) [**Figure 6.6b (i-v)**]. Upon resting the droplet on the area irradiated with the highest fluence (more hydrophobic), it spontaneously moves towards the regions irradiated with lower fluences (less hydrophobic). The advancing edge of the liquid contacts the adjacent area which is more hydrophilic (corresponding to irradiation fluences < 0.56 J/cm²), and the drop starts elongating in the direction of the motion. By tilting the same surface by 25°, we were able to observe a shift the center of mass of the drop upwards, as the drop ascends the structured regions with a direction from the most hydrophobic to the most hydrophilic region [**Figure 6.6c (i-v)**].

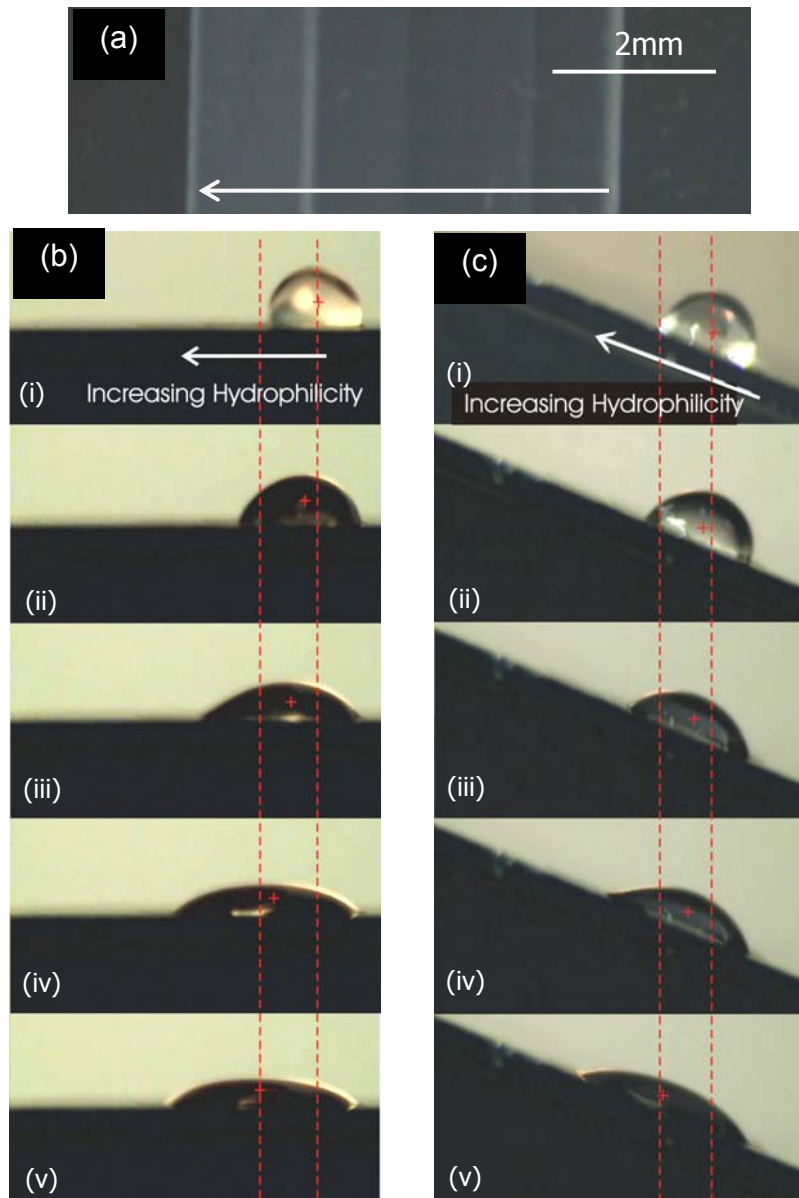


Figure 6.6: (a) Optical microscope picture of the Si surface structured with wettability gradient. The four laser fluences used were 1.1, 0.78, 0.56 and 0.33 J/cm² respectively. The arrow indicates the direction of increasing hydrophilicity (decreasing laser fluence). (b) Photographs of a water drop spreading on the same area, on a non-tilted surface. Time from the drop deposition: 0 (i), 2.5 (ii), 3.9 (iii), 4.4 (iv), and 5.7 s (v). (c) Photographs of a water drop ascending the same area tilted at 25°. Time from the drop deposition: 0 (i), 2.4 (ii), 5.0 (iii), 5.8 (iv), and 7.6 s (v). The shift of the center of mass from the initial to the final position is marked by the vertical red-dashed lines (b),(c).

The uphill velocity of the center of mass (M) is about 0.10 mm/s (the time variation of the coordinate, x_M , along the surface is plotted in **Figure 6.7**). In order to design surfaces with the suitable wettability gradient, for inducing uphill motion of liquids on substrates tilted at any angle, α , one has to take into account the regime of constant speed: $^{[131]}\dot{x}_M = v_0 - v_g$. In this expression, v_0 is the velocity of the drop on a horizontal plane, and v_g stands for the gravity contribution disfavoring the uphill motion of the liquid ($v_g \cong C \cdot g \cdot \sin \alpha$, where the coefficient C is expressed in time units, and g is the gravity acceleration). Since for our Si surfaces the measured speed of the drop on the 0° plane is of about 0.16 mm/s, we found that $\dot{x}_M > 0$ even for $\alpha = 90^\circ$. Therefore, the spontaneous uphill motion of the liquid may be also achieved on completely vertical surfaces.

In fact, we could observe water droplets climbing tilted planes at 90° (**Figure 6.8**). Such effective anisotropic wetting and spontaneous motion of liquids can be very useful for self-cleaning surfaces and microfluidic applications.

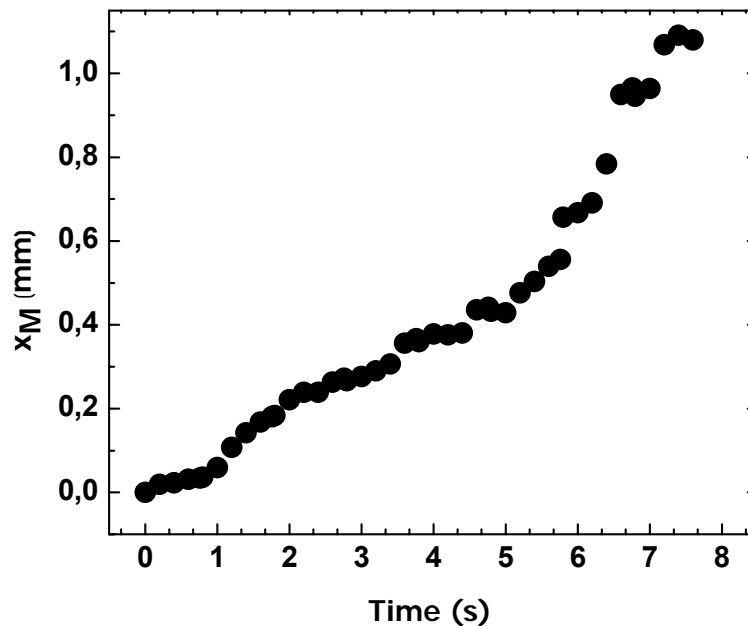


Figure 6.7 : Time dependence of the position of the drop center of mass on the structured Si surface, $x_M(t)$, when the sample was tilted by 25° .

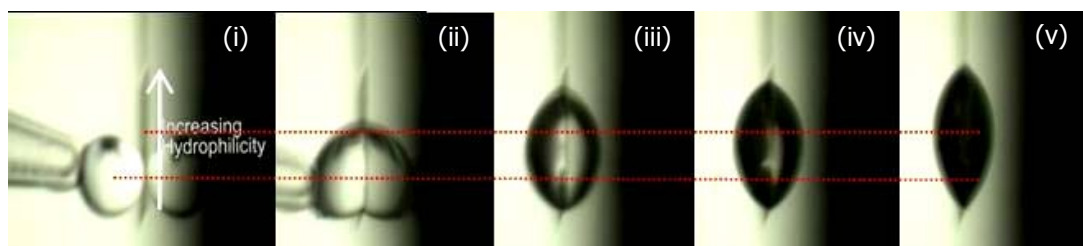


Figure 6.8 : Photographs of a water drop ascending the surface shown in Figure 7.6a tilted at 90°. Time from the drop deposition: 0 (i), 0.2 (ii), 0.5 (iii), 0.7 (iv), and 1.00 s (v). The shift of the center of mass from the initial to the final position is marked by the vertical red line at different times from drop deposition. The arrow indicates the direction of increasing hydrophilicity (decreasing laser fluence).

6.4 Superhydrophobic laser structured Si surfaces

Superhydrophobic surfaces can find use in self-cleaning, biological scaffolds, reduced flow resistance in microfluidic channels, lab-on-chip devices, liquid-based cooling of microelectronics, coatings e.t.c. A surface is called superhydrophobic when it exhibits a contact angle for water of more than 150° and negligible contact angle hysteresis (which is the difference between the advancing and receding contact angle), which means that only a slight tilt off the horizontal plane, is enough for a droplet to slide along it. Superhydrophobicity is achieved through a synergy of two important factors^[132]; surface energy, determined by chemical composition and surface topology.

The “model” superhydrophobic natural surface is that of the sacred lotus leaf (*Nelumbo Nucifera*). Barthlott and Neinhuis were the first to report the “lotus effect”; when water lands on the surface of a natural lotus leaf (**Figure 6.9 (a)**) it beads up to form nearly spherical drops (**Figure 6.9 (a)**-inset) that immediately roll off, removing dust particles and surface contaminants.^[104] **Figure 6.9 (b)** shows scanning electron microscopy (SEM) pictures of the sacred lotus leaf surface, comprising micrometer-sized papillae which have nanometre-sized branch like protrusions, while the whole structure is covered by epidermal cells of hydrophobic wax crystals.^[104] It has been demonstrated that the special hydrophobic and self-cleaning properties of certain natural surfaces are a

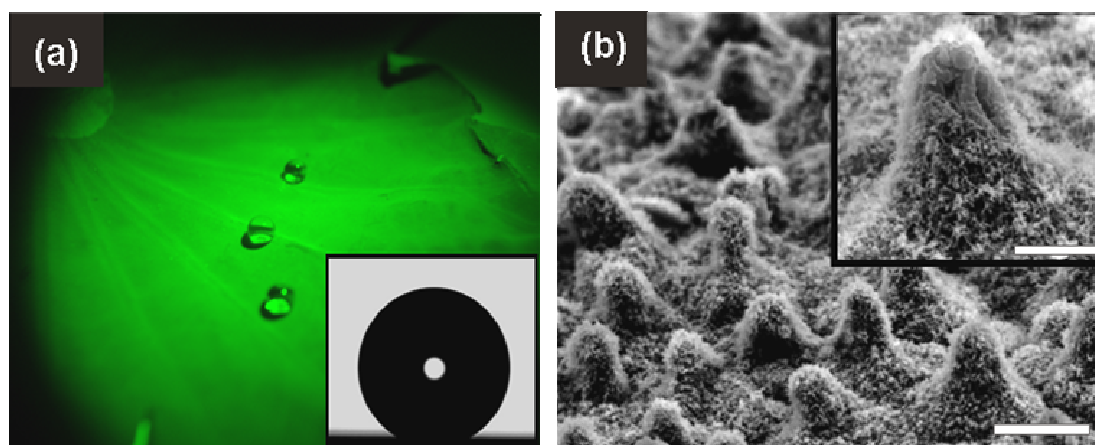


Figure 6.9 : Water droplets on a lotus leaf and scanning electron micrographs of its textured surface (a) picture of water droplets on a lotus leaf, inset: static contact angle (153° of a $2\ \mu\text{l}$ water droplet on the leaf) (b) SEM image of the leaf surface comprising micrometer-sized papillae (scale bar $10\ \mu\text{m}$) and inset: high magnification SEM image of a single papilla depicting nanometer-sized branch like protrusions (scale bar $5\ \mu\text{m}$).

direct consequence of hierarchical structuring at the micrometre and nanometre-scale. [132, 133]

As we have shown in the previous section, fs laser structuring of Si is an efficient way for producing hydrophobic surfaces. But even though these surfaces exhibit high contact angles, they exhibit high hysteresis as well, and are thus not superhydrophobic. In this section we demonstrate the fabrication of stable superhydrophobic surfaces by incorporating an additional step to laser patterning. This step involves coating of the structured surfaces with hydrophobic monolayers. In the following section we compare the wetting properties of the resulting surfaces with regard to the lotus leaf. We further demonstrate that these surfaces facilitate the motion of a liquid drop under minute gravitational impulses, while a surface tension gradient can be introduced to impede this motion.

6.4.1 Morphology and Static Contact Angle Measurements

Further reduction of the surface free energy of the laser structured surfaces and thus increase in hydrophobicity can be achieved by coating the patterned surfaces by

organosilane monolayers. DMDCS is chosen among other hydrophobic silanes due to its lower tendency to polymerise on Si surfaces, and its excellent stability, allowing it to maintain its hydrophobic properties for long time and wide temperature range.^[134] The contact angle measured on the DMDCS-coated flat Si was 104° , close to that reported for total monolayer coverage.^[42] Spectroscopic ellipsometry measurements on the flat region of the samples show that the average thickness of the silane coating is about 2.5 nm, in agreement to other studies on similar coatings.^[135] Atomic force microscopy (AFM) images of silane coated regions on the flat part of Si show a relatively homogeneous deposition of molecules over the entire area. The rms roughness is 1 nm indicating dense, void-free coverage (**Figure 6.10**).

Figure 6.11 (a) shows a water drop lying on the surface of DMDCS coated structured Si sample. The static contact angle formed is 156° (**Figure 6.11(a)**-inset). The morphology of the sample is shown in **Figure 6.11 (b)** while its inset is a high resolution image of the second-lengthscale roughness on a single microcone.

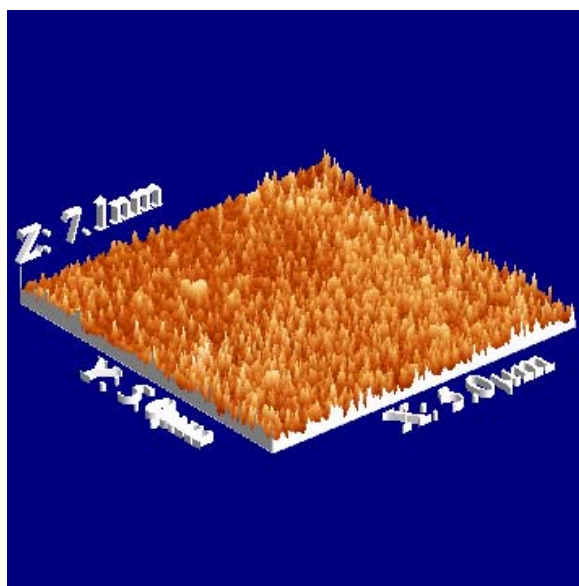


Figure 6.10 : Atomic Force Microscopy image of the surface morphology of the Dimethylchlorosilane coating. The scanned area was $5 \times 5 \mu\text{m}^2$.

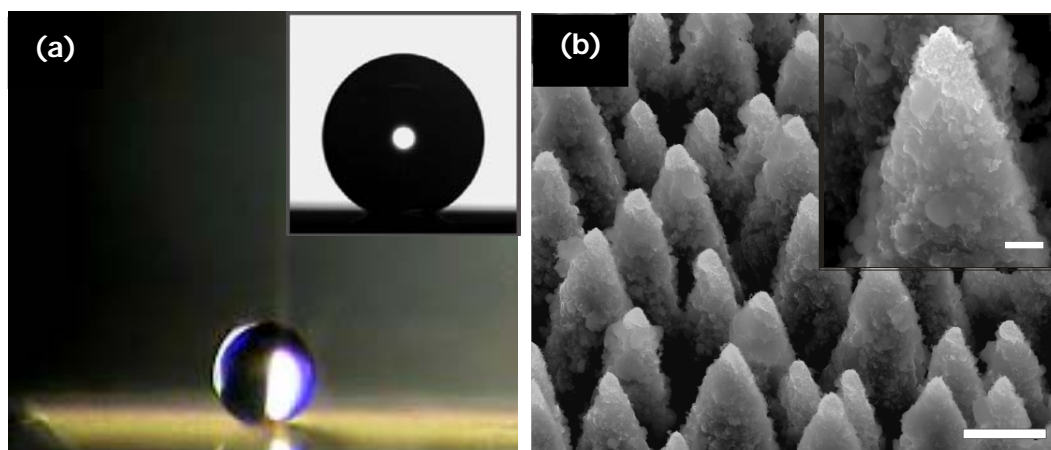


Figure 6.11 : (a) Picture of a water droplet on a silane coated Si surface (dark area), inset: static contact angle (156°) of a water droplet of 0.78mm radius on the surface (b) SEM image of the surface comprising micrometer-sized cones (scale bar $5\mu\text{m}$). The inset is high magnification SEM image of a single cone depicting nanometer-sized protrusions (scale bar $1\mu\text{m}$). The surface was structured in the presence of 500 Torr SF_6 at a laser fluence of 2.47 J/cm^2 with an average of 500 pulses. The hysteresis on this surface was $\sim 5^\circ$.

Figure 6.12 shows images of a water droplet lying on a DMDCS terminated flat and on a microstructured Si surface. The highest contact angle which was achieved on a patterned surface is 156° (**Figure 6.11 (a)**), corresponding to an increase of 52° with respect to the flat surface. This is close to the average contact angle measured on a lotus leaf of 153° (Inset of **Figure 6.9 (a)**). The corresponding fluence dependence is also plotted, indicating an abrupt transition to superhydrophobic angles at the lowest fluence utilised. At higher fluences the apparent contact angle remains fairly constant, although the nanometre scale morphology changes significantly. The wetting properties of these surfaces are very stable; contact angles remain unaltered after a month's exposure to ambient air.

6.4.2 Sliding Angle Experiments

As a rule, superhydrophobic surfaces should exhibit both high contact angle and little or no hysteresis. Hysteresis denotes the deviation between the advancing and receding contact angles ^[42] of the drop due to pinning of the contact line on surface

defects, and results in an increase of the inclination required for the droplet to slide along the surface. On the superhydrophobic lotus leaf, a tilt of only 3° is sufficient to initiate droplet motion. **Figure 6.12** shows the sliding angles of the laser structured surfaces, as a function of laser fluence (also summarized in **Table 6.1**). Water droplets leave the structured area at tilt angles lower than 10° for samples treated at fluences higher than $\sim 1.5 \text{ J/cm}^2$. Interestingly, these high-fluence samples exhibit the most pronounced second length-scale surface roughness. Samples in the mid fluence range ($0.7 - 1.5 \text{ J/cm}^2$) do not meet the criteria for superhydrophobicity; they exhibit high sliding angles although they show similar contact angle to their high-fluence counterparts. At fluences lower than 0.7 J/cm^2 , water drops remain pinned on these surfaces, at the highest sliding angles utilised.

Evidently, contact angle hysteresis is a very important parameter when droplet

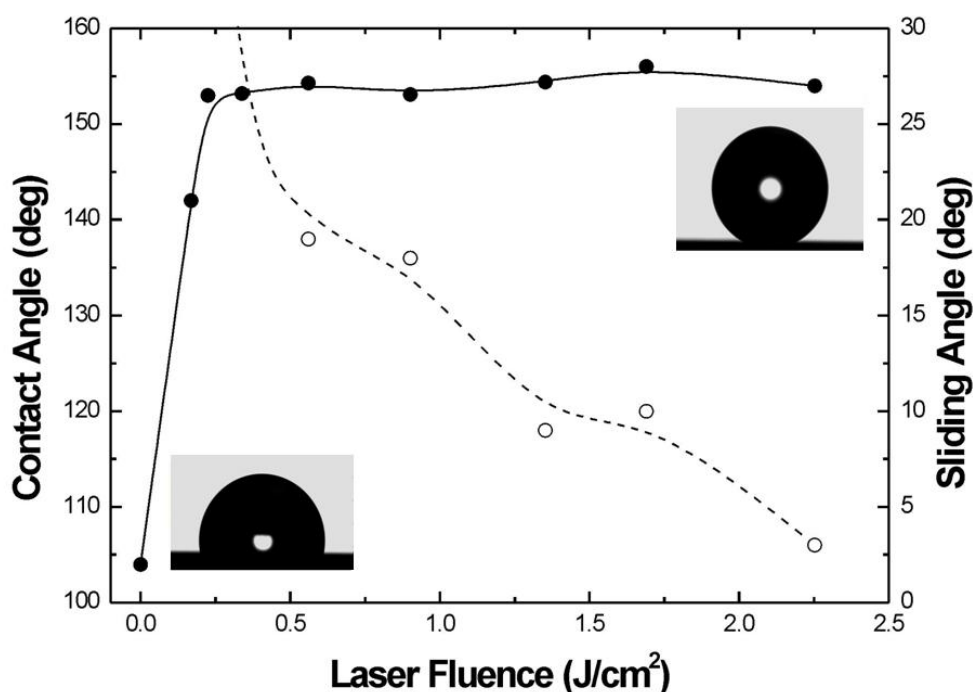


Figure 6.12 : Static contact angle (●) and sliding angle (○) measurements of a water drop on structured Si surfaces plotted as a function of laser fluence. For fluences below 0.5 J/cm^2 the sliding angles are higher than the 30° limit of our measurement setup. The lines are guides for the eye. Images of the droplet on the flat as well as on the structured Si surface are shown at the insets.

motion on a surface is considered. Motion initiation, at very low inclination angles (5°) on the high-fluence superhydrophobic surfaces, is translated into a small gravitational force required to initiate motion. In other words the friction between the droplet and structured surface is accordingly low. Low frictional motion is a key feature behind the unique lotus self-cleaning property and it is therefore desirable in any corresponding application, as it provides for efficient removal of dirt particles even when long travel distances are necessary.

Controllable manipulation of liquids has been the subject of considerable amount of scientific research for the development of micro-fluidics and lab-on-chip devices. In search of ways to efficiently drive a drop to specific sites in order to perform discrete functions such as mixing, analysis, reaction and storage, different approaches have been implemented, including thermal, ^[127] chemical, ^[136] electrochemical ^[137] and light-driven methods. ^[138] The possibility of selective laser structuring may give the ability to drive a drop under gravity along a patterned line and deliver it to a specific location where it can be immobilized and perform a desired operation; even though the water drop is highly mobile on the patterned areas (**Figure 6.12**) it shows high contact angle hysteresis on the flat regions of the sample. **Figure 6.13** shows the initial stages of the motion of a $4\mu\text{l}$ droplet close to the structured-unstructured area interface, upon the action of a gravitational force imposed by slightly tilting the sample (5°), in the case of a sample irradiated at the highest laser fluence. The drop starts slipping along the superhydrophobic surface (**Figure 6.13 (a)-(d)**), with a center of mass velocity of ~ 0.3 cm/s. The gravitational force required to initiate this motion is calculated to be $3.4 \mu\text{N}$. When the advancing front of the drop reaches the interface (**Figure 6.13 (d)**) it experiences a surface tension gradient (a result of surface morphology gradient) which forces it to escape the superhydrophobic surface and land on the flat region of the sample on which it is thereafter immobilized (**Figure 6.13 (e)**).

Assessment of the preferred state of the droplet in contact with a rough surface is not always a trivial task. On the other hand, the apparent contact angle of a drop in contact with a structured surface, is a result of surface energy minimization of the drop. It has been found ^[139] that the most energetically favourable state will be the CB one

when the contact angle of the flat surface, θ_o , is less than a critical value θ_c determined by:

$$\cos \theta_c = \frac{f-1}{r-f} \quad (\text{Eq. 6.6})$$

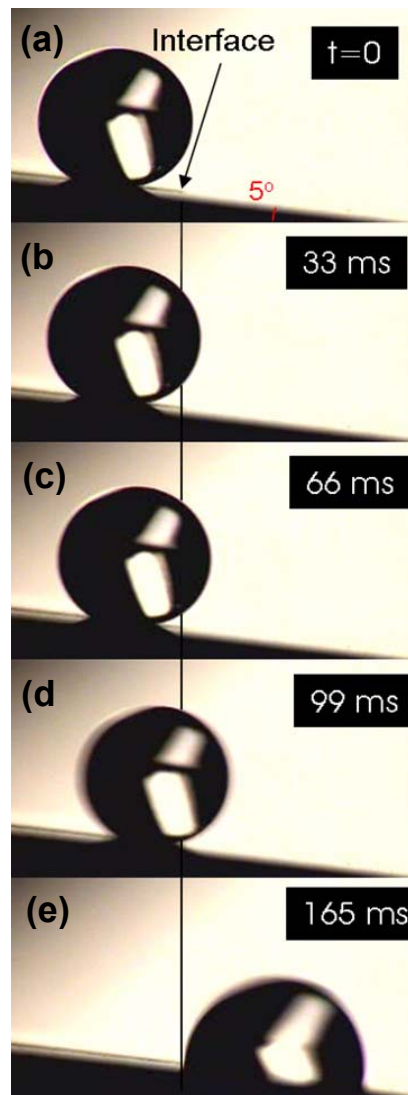


Figure 6.13 : (a)-(d); Snapshots of a 4 μ l water drop moving along on a 5° tilted superhydrophobic surface under the action of a gravitational component parallel to a superhydrophobic surface, as its advancing edge approaches the interface with the unstructured material. After this point (e) the drop experiences a surface tension gradient, imposed by the morphology change, forcing it to land on the unstructured part of the sample. The drop will thereafter stay pinned on that location independently of the sample inclination.

Equation 6.6 is deduced by equating θ_w of **Eq.(6.3)** with θ_{CB} of **Eq.(6.5)**. When $\theta_o > \theta_c$, then complete or partial wetting occurs as a result of the liquid penetration into the rough solid surface.

Contact angle hysteresis at the two states can be very different; ^[140] while it is extremely small in the CB state, it takes very large values in the Wenzel state. Accordingly a much smaller sliding angle is expected for the CB state when compared to the Wenzel. Hysteresis originates at the defects of the solid surface, whereby pinning of the liquid occurs. In the Wenzel state the number of such defects is high due to extended solid-liquid contact area. The opposite effect is observed in the CB state in which the droplet effectively sits on air. A Wenzel droplet is thus much more adhesive than a CB one, even when it exhibits a high contact angle. For the fabrication of superhydrophobic surfaces it is important to design textures for which the CB state is energetically more favourable than the Wenzel state.

Assuming that the Si structures formed roughly resemble truncated cones, the factors r and f can be deduced, for each sample, from the geometrical parameters obtained by image processing of the corresponding SEM pictures. The critical angle θ_c can then be calculated from **Eq. 6.6** and is listed in **Table 6.1**. Since the equilibrium contact angle of the flat Si silanized surface is $\theta_o = 104^\circ$, we observe that the above criterion $\theta_o < \theta_c$ is fulfilled only for the samples patterned at high laser fluences. Therefore the Cassie-Baxter state should be favored in those fluences. This is also consistent with the sliding angle results, indicating that superhydrophobicity and low frictional motion is always in accordance with a stable Cassie-Baxter state. On the other hand the preferred state of the low- fluence samples is the Wenzel one, which can explain their inferior wetting response.

<i>Sample</i>	<i>Laser fluence</i> (J/cm ²)	<i>Cone density</i> (cm ⁻²)	<i>r</i>	<i>f</i>	<i>Experimental results</i>		<i>θ_c</i> (deg)	<i>Stable state</i>
					<i>CA (deg)</i>	<i>SA (deg)</i>		
SP1	0.37	5.2 x 10 ⁷	2.71	0.10	142	> 30	110	W
SP2	0.45	2.2 x 10 ⁷	2.56	0.09	153	> 30	112	W
SP3	0.56	1.2 x 10 ⁷	3.40	0.05	153	> 30	109	W
SP4	0.78	4.0 x 10 ⁶	1.86	0.10	154	19	121	W
SP5	1.13	1.5 x 10 ⁶	1.32	0.20	153	18	135	W
SP6	1.56	1.5 x 10 ⁶	3.95	0.02	154	9	104	CB
SP7	1.91	1.5 x 10 ⁶	4.30	0.03	156	10	103	CB
SP8	2.47	1.5 x 10 ⁶	5.30	0.04	154	3	100	CB

Table 6.1: Morphological and wetting parameters of the laser structured Si samples prepared at various laser fluences. For each sample, the cone density, solid fraction f , roughness factor r , contact angle (CA) and sliding angle (SA) are shown (see text for definitions). In order to identify whether the stable state is the Cassie-Baxter (CB) or the Wenzel (W) one we compare the contact angle of the flat surface ($\theta=104^\circ$), with the critical angle, θ_c , as defined in the text.

6.5 Water repellence: laser structured Si vs. the lotus leaf

Water repellence is a desirable property in a wide variety of applications related to rain exposure (e.g. water-proof surfaces) as well as coating and deposition processes.^[141] A surface is called repellent when an incoming drop bounces away from the surface upon impact. Then the lowest velocity sufficient for a complete rebound gives a proper measure of repellence. Efficient water-proof surfaces must also exhibit a strong resistance against penetration by water drops impacting on them, even at large velocity regimes.^[142]

In this section we study the dynamic behaviour of water drops impinging patterned Si surfaces in comparison to that of the lotus leaf and the untreated Si surface. We show that laser processing followed by chloroalkylsilane monolayer coating leads to the production of one of the most water repellent surfaces ever reported. We quantify the repellence of this surface and we directly compare it, to that of the natural lotus leaf, to find a remarkable similarity in the overall performance.

Figure 6.14 shows a selected time sequence of snapshots depicting a 2.5 μl water drop free falling on (a) a structured Si surface with the lowest hysteresis and (b) on a lotus leaf surface. For both surfaces, the drops are released from a height of 10 mm at $t=0$ (i), they impact on each surface (ii), and then bounce back to a maximum height shown in (iii). The drops successively impact the surfaces (iv, vi, viii...) and bounce back (v, vii...), coming to rest only after several impacts. Clearly, both surfaces are highly water repellent, exhibiting similar behaviour with time (the temporal resolution of these

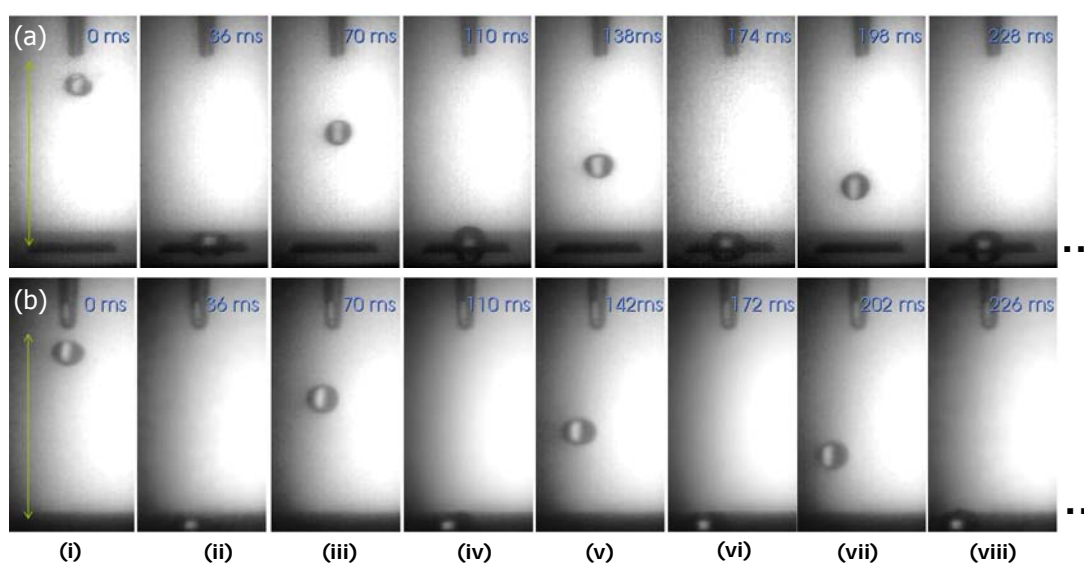


Figure 6.14 : (a) Impact of a 2.5 μl water drop on a laser structured Si surface with time. The drop comes to rest after several rebounds and only when it reaches the flat region of the sample and (b) impact of a 2.5 μl water drop on a lotus leaf surface. The drop comes to rest after several rebounds. In both cases the drops are released from a height of 10 mm. $t=0$ corresponds to the first frame for which the drop is detached from the pipette.

measurements was 2 ms). The drops moved away from the centre of the sample upon successive impacts due to a translational velocity component along the sample surface.

Figure 6.15 (a) and (b) presents a selected time sequence of snapshots depicting a 10 μl water drop free-falling on the structured surface with the lowest hysteresis, and on a lotus leaf respectively. The 10 μl drop (radius of $R=1.35$ mm) is released from a height of 10 mm so that the impact velocity is ~ 0.44 m/s. It is interesting that the behaviour of the falling droplet is quite similar in the two surfaces. In particular, we observe that the drop's shape changes significantly during impact, as its kinetic energy transforms into energy stored in surface deformation. In this case, the deformation is strong, because the Weber number, W_e , defined as the ratio of the arriving kinetic energy to the intrinsic surface energy,

$$W_e = \frac{\rho \cdot V^2 \cdot R}{\gamma} \quad (\text{Eq. 6.7})$$

is higher than unity. Here ρ is the liquid density, V the impact velocity, R the liquid drop radius and γ its surface tension.

Despite this deformation, both surfaces are so water-repellent that the drop bounces back numerous times [**Figure 6.14**]. **Figure 6.15 (c) and (d)** show similar series of video frames for the structured Si and the lotus leaf surface respectively, in the case of $W_e < 1$, where the drop is lightly deformed. On the other hand, as shown in **Figure 6.15 (e)**, no rebound is observed when the drop impacts on the silanized flat region of the Si sample. In this case the surface is not repellent and the drop has insufficient momentum to leave the sample. As a result it remains stuck to the surface.

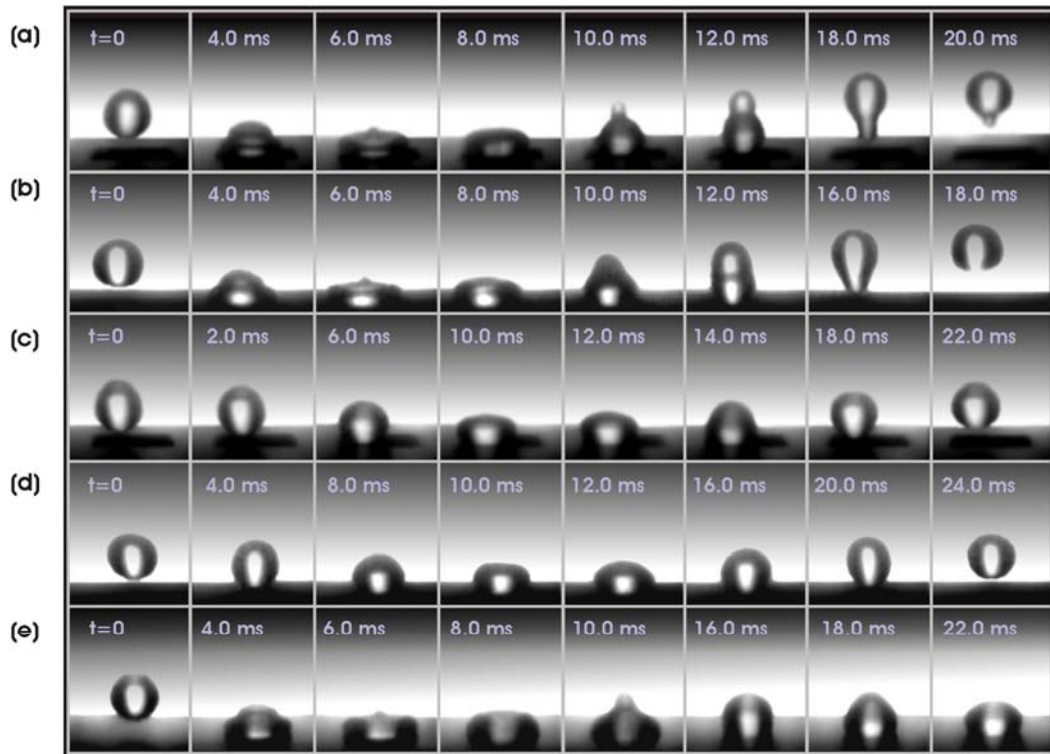


Figure 6.15 : Selected snapshots of a millimetric water drop impact on a lotus leaf, a flat and a laser structured Si surface. (a) on a laser structured Si surface with a Webber number, We , of 3.5, (b) on a lotus leaf surface with $We= 3.5$, (c) on a laser structured Si surface with $We= 0.7$ (d) on a lotus leaf surface with $We= 0.7$ and (e) on an unstructured Si surface with $We= 3.5$.

The elasticity of the collisions observed on both natural lotus and laser structured surfaces is remarkable, indicating a high degree of repellence. A direct measure of this elasticity is the restitution coefficient, $\varepsilon = V'/V$, defined as the ratio of the centre of mass velocity just after impact, V' , to that just before impact, V . This coefficient was deduced from the recorded video clips and is plotted in **Figure 6.16** as a function of V for a series of experiments, performed with drops of different volumes. The highest elasticity is observed at intermediate velocities, from ~ 0.15 m/sec to ~ 0.25 m/sec, where the restitution coefficient is found to exceed 0.90. Its value matches that of lotus and to our knowledge is among the highest ever reported.^[24] Elasticity arises from the efficient interchange between kinetic and surface potential energy during drop deformation.^[5,25] According to *Richard and Quere*^[24], even in the ideal case of zero energy loss during

collision there is a limit in elasticity, $\varepsilon < 1$, due to the transfer of a part of kinetic energy into drop vibrations.^[5] In all cases we observed that the drop vibrates after leaving the surface. Thus, part of the initial kinetic energy of the drop is transferred into vibrational energy after the impact, and subsequent damping of the bouncing motion occurs due to viscous dissipation.

Although full rebounds occur at moderate impact velocities, the situation is different at small and large V . For small velocities, ε decreases abruptly with decreasing V and reaches zero at some velocity that depends on the droplet volume. This is the threshold that quantifies the water repellence of the surface^[25]; the smaller this velocity, the more water repellent the surface. We find this velocity for our surface to be comparable to that of the lotus leaf (**Figure 6.16**). The bouncing to non-bouncing transition arises from the presence of surface defects that become the main source of kinetic energy dissipation.^[26] The contact line pins on such defects resulting in a difference between the advancing, θ_a and receding, θ_r contact angles (hysteresis). The bigger the droplet, the longer this line is, resulting to higher hysteresis and therefore to an increase of the threshold velocity anticipated. This is exactly what we observe in **Figure 6.16** for both surfaces examined. For a drop of radius R and density, ρ , the pinning force per unit length is^[27] $\gamma \Delta \cos \theta$, where $\Delta \cos \theta = \cos(\theta_a) - \cos(\theta_r)$, and γ is the liquid-air surface tension. The energy dissipated will scale as $\gamma R^2 \Delta \cos \theta$. The drop will bounce provided that its kinetic energy, which scales as $\rho R^3 V^2$, overcomes this dissipation. Equation of these two energies, gives an estimate of the velocity threshold for repellence. We have measured $\theta_a = 157^\circ$ and $\theta_r = 152^\circ$ for the laser structured surface and for the $2.5 \mu\text{l}$ drop we have calculated this velocity to be $\sim 6 \text{ cm/sec}$, a value close to the one observed experimentally.

Finally, in the high velocity regime, ε slowly decreases with V because of the large drop deformation followed by increased internal vibration after impact. It has been observed in other structured surfaces that there exists an upper velocity above which significant impalement of the drop occurs resulting in part of it getting captured to completely wet the surface.^[27,28] The value of the highest velocity for which the surface remains dry, has also been used as a measure of the surface resistance against wetting. In this context, we have examined the behavior of water droplets with impact velocities up to 5 m/s , a typical

value for the terminal velocity of millimetric raindrops.^[27] In this high velocity regime, the drop brakes apart into numerous smaller droplets. This behavior was never observed in the flat region of the Si sample, indicating that structuring favors the creation of tiny droplets in an effort to resist penetration by the falling drop. After each experiment, the surface was thoroughly examined, with a high resolution CCD optical system, for signs of water impalement. We found the lotus leaf as well as the laser structured surface to be impervious to water penetration over the entire range of attainable impact velocities (0.2 - 5 m/s). It should finally be emphasized that the low-adhesion and high repellence of the laser structured surfaces are maintained even after rinsing and complete immersion in water for long periods of time. Long-term endurance against wetting is a feature that is always desirable in relevant applications.

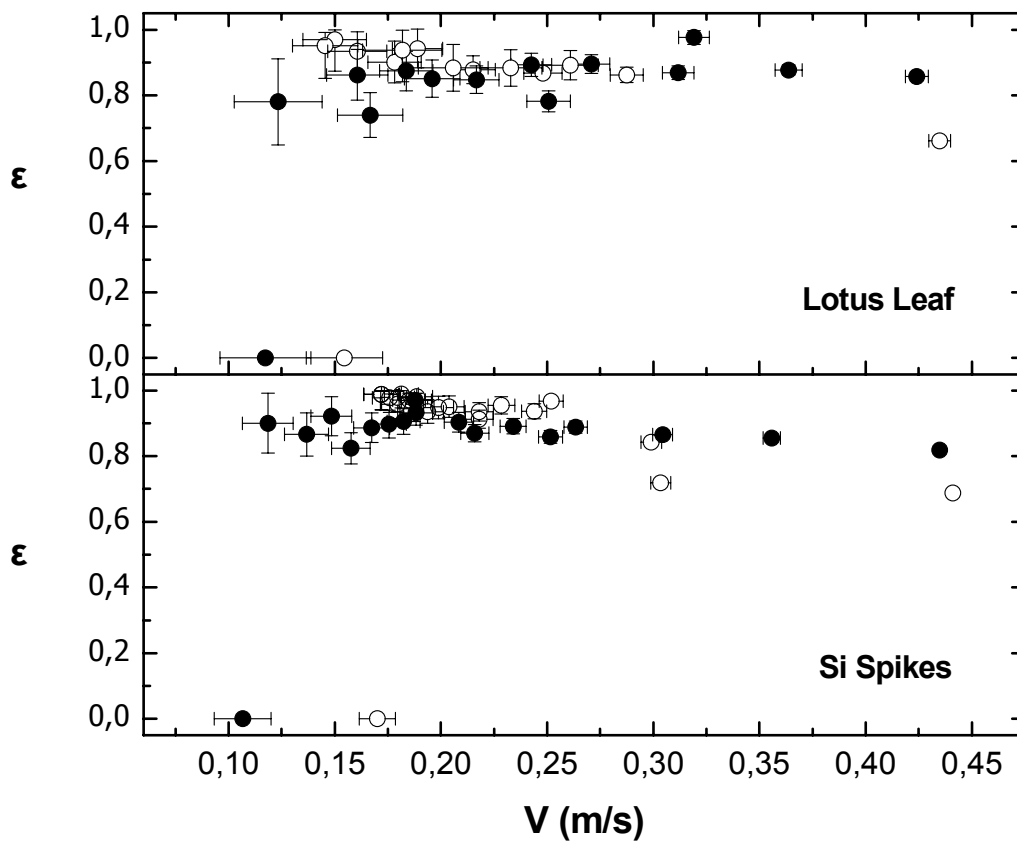


Figure 6.16 : Restitution coefficient ϵ as a function of the impact velocity V for a lotus leaf and a laser structured silanized Si surface. The solid (\bullet) and open symbols (\circ) represent data taken for water drops with a volume of 2.5 μl and 10 μl respectively.

6.6 Electrowetting on Dielectric (EWOD)

Liquid actuation and manipulation on solid substrates using electrowetting (the change in the wetting response of a surface, upon the application of an electric field) is a rapidly growing field of research and has generated considerable interest from both fundamental and applied view points.^[143] Electrowetting has been used to demonstrate droplet actuation^[144,145,146] and other microfluidic operations such as the formation, mixing, and splitting of droplets.^[147] Potential applications range from "lab-on-chip" devices^[148,149,150] to adjustable lenses,^[151] display technology,^[152] fiber optics,^[153] and microelectromechanical systems (MEMS).^[154]

In 1875 G. Lippmann^[155] explained the shape variations of a mercury droplet immersed in an electrolyte, when a voltage was applied across the liquid interface. Froumkine^[156] applied the same idea to *electrowetting*, i.e. how electric charges at an interface modify the contact angle of a drop of electrolyte on a metal surface. More recently, experiments on self-assembled monolayers on gold surfaces showed how the functionalization with electro-active alkane-thiol molecules could amplify such phenomena^[157,158]. Meanwhile, another configuration was investigated; instead of a simple metallic substrate, a layered structure made of a conductor covered by an insulating film of macroscopic thickness could produce large wettability changes^[159]. This new effect was called electrowetting-on-dielectric (EWOD). This configuration could make it possible to circumvent the main shortcoming of typical electrowetting which inhibited its use in broader applications; the electrolytic decomposition of liquids upon applying voltages beyond a few hundred millivolts. Furthermore, the variation of wettability for flat surfaces in EWOD could be reversible in a very large range of contact angles^[159, 160,161,162]. The robustness, reversibility, simplicity and low-cost of this new process facilitated various applications and the development of new devices.

In a common electrowetting on dielectric set up, the insulating layer is composed of an inorganic material such as SiO₂ or Si₃N₄ or organic polymers, and the hydrophobicity is induced through coating with a hydrophobic layer such as fluoropolymers or resists.^[143] A potential is applied between a conducting liquid on an insulating layer and a counter electrode positioned below the insulating layer. Charge

accumulates at the solid-liquid interface, leading to a change in contact angle from hydrophobic to more hydrophilic.

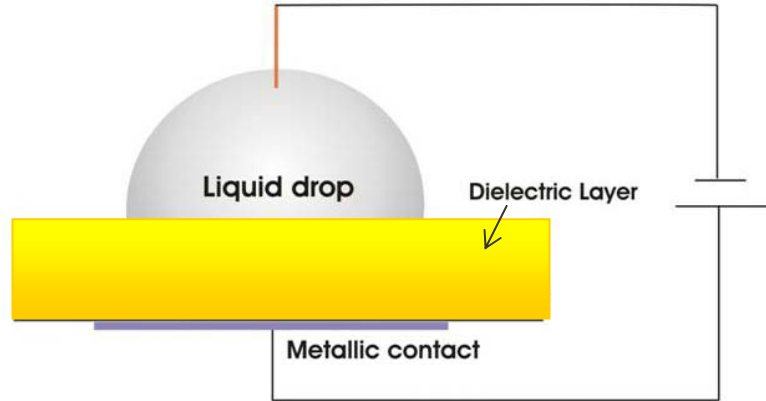


Figure 6.17 : Typical Electrowetting on Dielectric Setup

When the potential is applied at the solid-liquid interface, V_{sv} and V_{lv} are assumed to be potential independent and V_{sl} varies with the potential according to the Lippmann equation.^[162]

$$\gamma_{sl}^q = \gamma_{sl} - \int_{V_{sl}^0}^{V_{sl}} \sigma_{sl} \cdot dV_{sl} \quad (\text{Eq.6.8})$$

where

$$\sigma_{sl} = \int_{V_{sl}^0}^{V_{sl}} C_{sl} \cdot dV_{sl} \quad (\text{Eq.6.9})$$

Here γ_{sl} is the solid-vapor interface tension at the potential of zero charge V_{sl}^0 , V_{sl} is the potential on the solid-liquid interface, σ_{sl} is the surface charge density and C_{sl} is the differential capacitance of the interface. Substitution of **Eq 6.8** and **Eq.6.9** in **Eq.6.1** gives:^[162]

$$\cos \theta_q = \cos \theta + \frac{1}{\gamma_{lv}} \int_{V_{sl}^0}^{V_{sl}^o} \int C_{sl} \cdot [dV_{sl}]^2, \quad (Eq.6.10)$$

where $\cos \theta$ is the cosine of the contact angle in the absence of charges. Assuming further $C_{sl} = \epsilon_0 \epsilon / d$ (ϵ being the dielectric constant of the layer, ϵ_0 the dielectric constant of air and d its thickness) to be potential independent and performing double integration with respect to V_{sl} , results in the relationship between cosine of the contact angle and potential,^[162, 163] otherwise known as the Lippman-Young Equation:

$$\cos \theta_q = \cos \theta + \frac{\epsilon_0 \cdot \epsilon \cdot (V_{sl} - V_{sl}^0)^2}{2 \cdot d \cdot \gamma_{lv}} \quad (Eq.6.11)$$

It should be noted that in such an EWOD configuration, an electric double layer builds up (thickness d_H is usually a few nm) at the insulator–droplet interface. Since the insulator thickness d is usually much larger than d_H , the total capacitance of the system is reduced tremendously. The system may be described as two capacitors in series,^[158, 162] namely the double at the solid–insulator interface (capacitance c_H) and the dielectric layer with $c_d = \epsilon_0 \epsilon_d / d$ (ϵ_d is the dielectric constant of the insulator). Since $c_d \ll c_H$, the total capacitance per unit area $c \approx c_d$. With this approximation, we may neglect the finite penetration of the electric field into the liquid, i.e. we treat the latter as a perfect conductor. As a result, we find that the voltage drop occurs within the dielectric layer.

▪ Requirements for efficient EWOD

According to **Eq. 6.11**, the smaller the thickness d or the larger the dielectric constant ϵ , the larger the contact angle change at a given applied voltage. Or a smaller potential is needed for obtaining the desired contact angle change. In order to reduce these voltage requirements, the basic strategy is to use a thinner dielectric film with a higher dielectric constant. But also very important aspects are for the dielectric layer to have sufficiently high initial contact angle, low contact angle hysteresis, high dielectric strength, and to exhibit the possibility of uniform, conformal coating.

On the other hand surface roughness can significantly alter the contact angle of a droplet and change its effective contact area with the surface. Since electrowetting also acts to change the droplet contact angle, surface design can be used in conjunction with electrowetting to enhance control over droplet contact angles.^[164] Nevertheless very few attempts to address this issue have been made.^[164,165,166] The main problem stems from the high degree of roughness exhibited by superhydrophobic surfaces, which causes substantial spatial separation between the liquid and the underlying electrode, strongly impeding the electrowetting effect.^[165]

Droplet-based microfluidics, fluidic drag reduction, liquid-based cooling of microelectronics, microbatteries, and chemical microreactors are some of the areas that can potentially benefit from such technology.^[170]

▪ **EWOD on unstructured and on laser structured Si surfaces**

We use the experimental setup shown in **Figure 6.18** to study and compare EWOD on flat and on structured n-type Si surfaces. For the EWOD experiments, a Si oxide layer was grown on the surface of flat and structured Si; this would serve as the dielectric. The oxide was thermally grown in a tube furnace in ambient conditions. Heating up to 1000 °C, made possible the fabrication of Si oxide layers with different thicknesses, depending on the heating time employed. The thicknesses of the grown Si oxide layers were measured using ellipsometry.

However, since the Si oxide surface is hydrophilic, a DMDCS monolayer had to be deposited on top of the Si oxide surface using the methodology described in **Chapter 2**, in order to ensure hydrophobicity at the initial state (without any voltage applied). This would allow the contact angle change to be higher and thus the phenomenon to be amplified.

In this section, we have performed experiments on flat and on structured samples with different dielectric layer thicknesses in order to quantify the optimum conditions (layer thickness, roughness of structures) for inducing more efficient electrowetting on dielectric for low applied voltages. In order to avoid phenomena related to electrolysis,

the current was recorded for different applied voltages. A detailed description of the experimental setup used can be found in **Chapter 2**.

The liquids tested were nanopure water (surface tension: 72.8 mN/m, conductivity: 0.064 $\mu\text{S}/\text{cm}$) and glycerol 85% (surface tension: 65.7 mN/m, conductivity: 0.040 $\mu\text{S}/\text{cm}$) with volumes of 1-3 μl in order to identify the optimum in terms of surface tension and conductivity. All the experiments were performed in air and at room temperature. The samples tested had different dielectric layer thicknesses, from 25nm up to 200 nm.

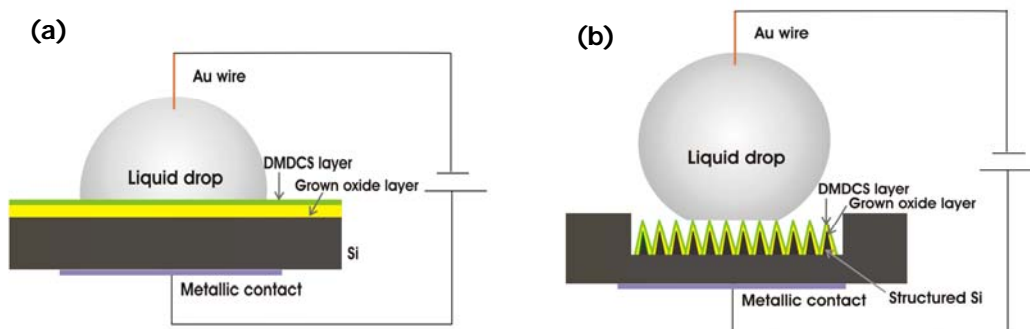


Figure 6.18 : The Electrowetting-on-Dielectric system for (a) flat Si and (b) structured Si.

We have found, as expected, that the smaller the thickness of the dielectric layer, the lower the voltage required to induce contact angle changes. However a competitive phenomenon related to breakdown of the dielectric layer starts taking place when its thickness is very low. Dielectric breakdown can make electrolysis at low applied voltages possible. Electrolysis is followed by an increase of the current flow recorded, and the optical observation of bubbles inside the liquid drop. As a consequence, after this point the contact angle behavior as a function of applied voltage strongly deviates from the one predicted by the Lippmann-Young equation. It is evident that an efficient EWOD setup can be achieved through a compromise between two factors; the dielectric layer thickness and the voltage requirements minimization.

Figure 6.19 shows the EWOD for (a) an unstructured and (b) a structured Si. The liquid drop was a 2 μl , 85% glycerol in water solution. The insets show the increase of the absolute value of the applied voltage in Volts (yellow panel) as well as the induced current fluctuations in nA (black panel). In the specific experiment currents up to a few tens of nA were recorded, indicating that no electrolysis related phenomena took place.

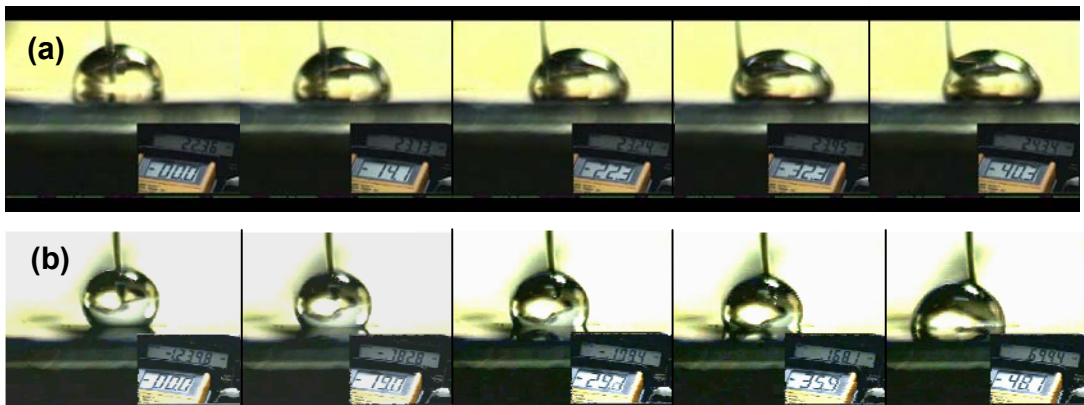


Figure 6.19 : Electrowetting-on-Dielectric for (a) Flat Si and (b) Structured Si. The Si oxide thickness was 110 nm, coated with dimethyl-dichloro-silane. The insets show the increase of the absolute value of the applied voltage in Volts (yellow panel) as well as the induced current fluctuations in nA (black panel).

The plots of **Figure 6.20** show the decrease of the apparent contact angle with increasing applied voltage for (a) the unstructured and (b) the structured Si samples. The insets show the cosine of the contact angle as a function of the square of the given applied voltage, for each surface. The red line is a fit to the data according to the linear behaviour predicted by the Lippmann-Young equation (**Eq. 6.11**). For both the unstructured and the structured surfaces we find the experimentally observed behavior to be in good agreement to the one predicted (insets of **Figure 6.20**).

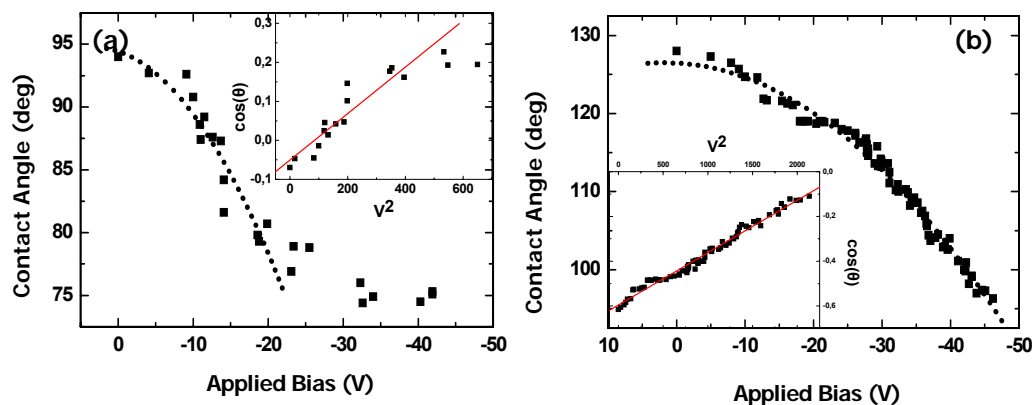


Figure 6.20 : Contact angle of a 85% glycerol drop as a function of applied voltage for (a) the flat Si surface and (b) the structured Si surface. The black line is a guide to the eye. Insets: The cosine of the contact angle as a function of the applied voltage is shown. The red line is a fit of the experimental data to the Lippmann-Young equation.

The change in the contact angle is more pronounced in the case of the structured surface (**Figure 6.20 (b)**). By increasing the absolute value of the applied voltage, and thus changing the energy of the surface, the drop is free to slowly sink inside the larger surface area defined by high roughness of the structures, leading to a more pronounced contact angle change. It is possible that even lower contact angles could have been observed for the structured surface, however these observations are limited by the size of the structured region as compared to the size of the highly mobile drop.^[iii] By increasing the applied voltage and thus decreasing contact angle, the droplet's advancing edge reaches the more hydrophilic flat Si surface, and starts spreading towards it. No reliable measurements can be made from this point and on.

Another interesting observation, is the saturation of the value of the contact angle after a certain applied voltage, at the flat Si surface (**Figure 6.20 (a)**). This phenomenon is not uncommon in EWOD systems, however its origin is still undetermined. There have been cases where the origin of the contact angle saturation has been attributed to trapped charges in the dielectric layer,^[167] material deficiency,^[168] or that contact angle saturation occurs at the voltage corresponding to the onset of air ionization.^[169] It is clear though

^[iii] The high mobility of the drop may be associated with minor variations in the homogeneity of the dielectric layer.

that the effect is still poorly understood. On the other hand, no saturation region can be recorded for the structured sample (**Figure 6.20 (b)**) since after a certain point the drop comes in contact with the unstructured part of the sample, as explained in the previous paragraph.

Finally vivid oscillations (contraction and retraction phenomena) of the liquid drops with a period of less than 1 sec are observed, especially in the unstructured samples. This is observed for dielectric layer thicknesses higher than 25 nm and becomes more pronounced at higher thicknesses. The origin of this phenomenon is subject to further investigation.

- **Reversibility of the process**

Partial reversibility is observed on flat surfaces and also on structured ones, even though in the second case it is a lot less pronounced. For example, **Figure 6.21 (a)** shows the contact angle of a glycerol drop on a flat Si surface, before the application of an electric field (0 Volt) and **(b)** after the application of a field (40.3 Volt). By reducing the absolute value of the applied voltage, the drop reaches maximum contact angle values close to its initial one, even though this happens at higher voltages (18 Volt) **Figure 6.21 (c)** and not at 0 Volt.

On the other hand, only few recent reports refer to the possibility of inducing reversible contact angle changes on rough surfaces ^[166,170] with specific geometry. This is because the transition involves sizable energy dissipation associated with the propagation of the liquid front through the structured layer during the wetting process. As a result, the transition becomes irreversible, since the system lacks the energy required to return to the initial state when the voltage is removed. In order to overcome this obstacle, two main strategies have been proposed: ^[171]

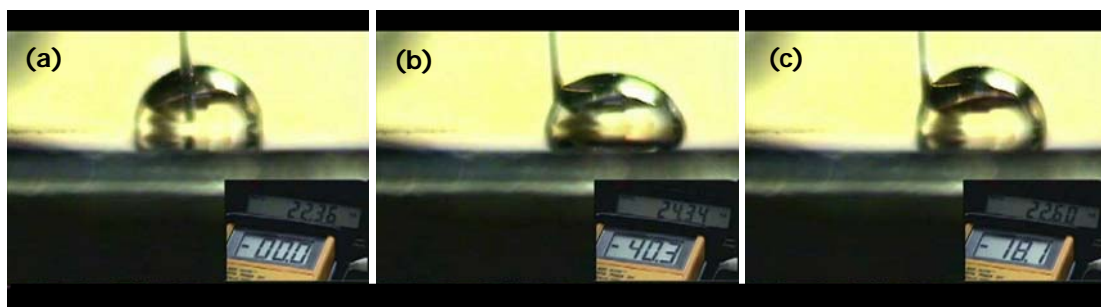


Figure 6.21 : Reversibility in an Electrowetting-on-Dielectric system on flat Si (a) before the application of voltage (0 V), (b) maximum contact angle change upon the application of 40.3 V and (c) decrease of the voltage to 18.1 V, where the system reaches contact angles close to the initial one (a). The insets show the increase of the absolute value of the applied voltage in Volts (yellow panel) as well as the induced current fluctuations in nA (black panel).

- (a) To implement very special morphologies, an approach that is restricting, or
- (b) To momentarily increase the temperature of the substrate surface in such a system. Then the pressure of the gas and the vapour will temporarily increase and thus initiate the reverse transition. Even in the case of complete wetting where no air is trapped underneath the drop, all the vapour would be produced directly at the liquid-substrate interface during the temperature increase. The potential drawback in this case is the effectiveness of the energy transfer, which might lead to a high energy cost in the reverse transition.

6.7 Chemically induced wetting

An alternative way to dynamically tune the wetting response of a surface is related to the incorporation of organic solvent vapors. Controllable switching from an initially hydrophobic to a super-hydrophilic state leading to complete wetting can be achieved when the sample-liquid droplet system is exposed to the vapor of organic solvents. This dynamic control from one state to the other is desirable in many applications related to spreading of liquids on solid surfaces as well as chemical sensor applications

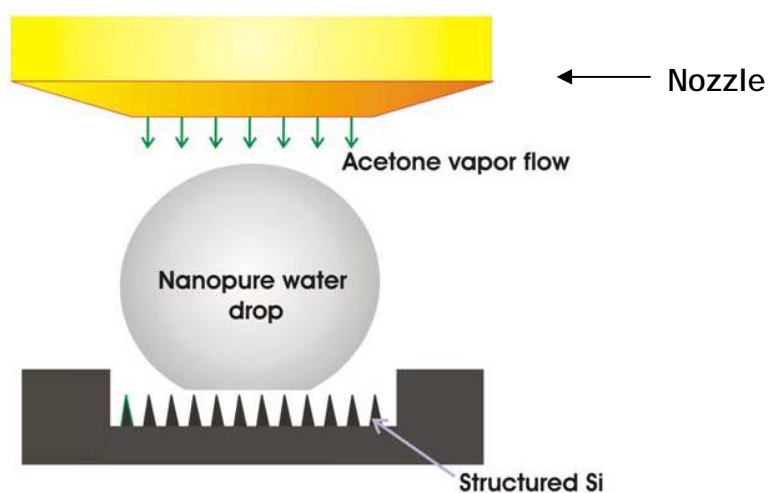


Figure 6.22 : Chemically induced wetting setup.

The dynamic response of the samples when exposed to different solvents and different flow rates was examined, with nitrogen used as the carrier gas. **Figure 6.22** shows the basic experimental setup used for the purposes of this work (a more detailed description can be found in **Chapter 2**). Prior to each measurement, the structured and unstructured Si samples were immersed in a HF 10% solution, rinsed with copious amounts of water, and subsequently dried with nitrogen. 2 and 3 μl drops (nanopure water or glycerol 85%) were gently deposited on the sample surfaces. The organic solvents used were: Acetone (99.8%), Methanol (99.8%), Ethanol (99.9%), 2-Propanol (99.8%), 1-Butanol (99.5%) at flow rates of 0.1-2 lt/min. Due to the high vapor pressure of most of the organic solvents used, heating of the solvents was not necessary, and therefore the experiments shown here were performed at room temperature. The vapor flow over the sample-liquid system is initiated at $t=0$, which is defined as the time that the nozzle valve opens, after the vapor flow has been stabilized.

Figure 6.23 shows the decrease in the apparent contact angle of a 2 μl water drop in the presence of acetone vapor. Under the action of acetone vapor flow, the drop sinks inside the recessed areas, to completely wet the surface.

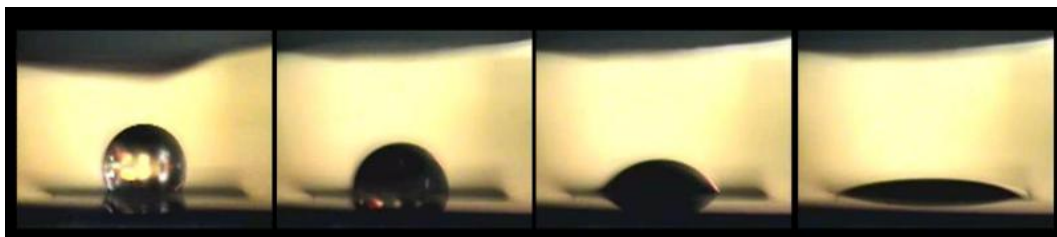


Figure 6.23 : Image sequence of the decrease in the contact angle of a 2 μl water drop on a structured Si surface in the presence of acetone vapor, at a flow rate of 2 lt/min.

We find that the higher the vapour flow for the specific organic solvent, the faster the decrease in the contact angle (**Figure 6.24**) on a structured surface. In this way, the slope of the contact angle as a function of time is steeper. For flow rates higher than 0.5 lt/min the contact angle change as a function of time reaches saturation, since its slope remains practically unaltered. For both the nanopure water and the glycerol drop the hydrophobic to hydrophilic transition on the structured surfaces takes place in the presence of acetone vapor, although the transitions for the glycerol drop are slower.

Apparently, the phenomenon of the change in the contact angle of a water drop in the presence of acetone vapour is negligible for the unstructured Si sample, even when high flow rates were tested (black line-**Figure 6.24**). In fact the effect is very limited on the flat surface of the sample for all the organic vapors used.

Similar transitions, from hydrophobic to complete wetting states, were also observed for the other organic solvent vapors tested on structured Si surfaces (Methanol, Ethanol, 2-Propanol and 1-Butanol). The only differentiation between them was the steepness of the contact angle vs. time slope, i.e. the decay time. It should be noted that the same experiments were performed with other organic vapors as well, which did not lead to similar wetting phenomena in the examined flow ranges; 4-Methyl-2-Pentanone lead to a small contact angle decrease, while for Toluene and Dichloromethane the change was negligible.

We have found the vapor pressure of the solvent used as well as its solubility to water (related to how polar the molecule is) to be very important parameters. The transition from an initially hydrophobic surface to complete wetting among the organic vapour molecules tested occurs only for the ones that are polar, showing that sensing is

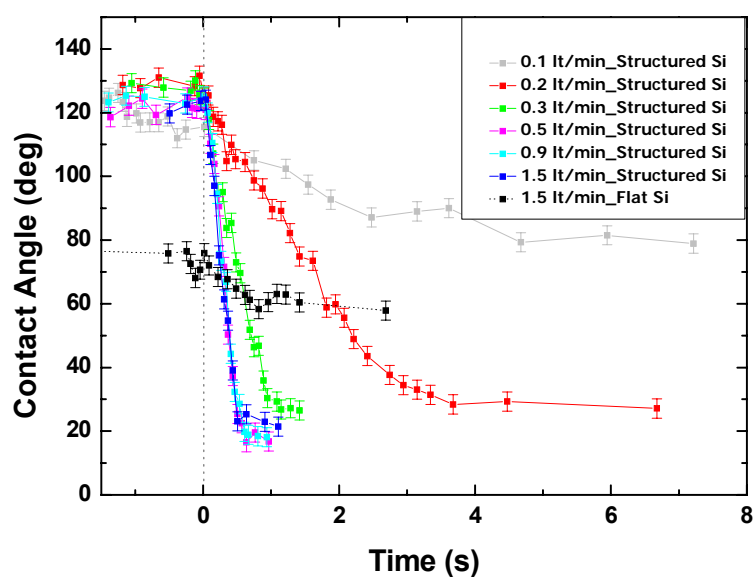


Figure 6.24 : Apparent contact angle as a function of the decay time for different flow rates of acetone vapor on a structured Si surface. The decay time of a flat sample at the highest flow rate is also shown for comparison. The experiments were performed at room temperature. The drop was 3 μ l nanopure water

selective. Furthermore the contact angle of a liquid exhibits a characteristic decay time for each one of the different organic molecules tested, under the same flow.

Interpretation of the origin of this phenomenon is not a trivial task. In order for such switching to occur, either the energy of the surface or the energy of the drop has to change, when in contact with the organic vapor. On the other hand it is important to keep in mind that the structured Si surface is not in fact the same as that of the unstructured surface. As we have shown in **Chapter 3**, the surfaces of the structured Si samples consist of highly S doped nanocrystalline Si layers, with a specific porosity. Numerous reports in literature ^[172,173,174] show the possibility of using porous Si as a chemical sensor, since it is a highly chemically active surface. For example thin films of porous Si have been extensively used to detect vapours, based on changes in their refractive index. If a phenomenon similar to this is to take place in our experiments, it is possible for the macroscopic roughness of the structured surface could contribute drastically in the fast sinking of the liquid drop within the recessed area, since due to the high roughness of the structures the overall unfolded area is significantly increased. However, more

experiments are required in order to elucidate the mechanisms and interpret the phenomenon.

6.8 Conclusions and Future Prospects

In this chapter we have demonstrated the use of laser structuring for tailoring the wetting response of Si surfaces. In particular we have found:

- fs-laser irradiation may be employed to render Si hydrophobic without any additional surface coating. The resulting structures consist of double-lengthscale roughness, and we achieved an enhancement of the water contact angle from 66° to greater than 130° . This process can be employed for fabricating controlled gradients of wettability, that drive the anisotropic wetting and the spontaneous motion of water droplets, both on horizontal surfaces and on planes tilted at any angle.
- By incorporating an additional step to the laser fabrication process, which is related to the coating of the structures with chloroalkylsilane monolayers, we have been able to fabricate stable, superhydrophobic surfaces on Si. Both the contact angles obtained as well as the hysteresis are comparable to those of the “model” superhydrophobic surface of the lotus leaf. We have further used selective surface patterning so as to control droplet motion, slippage or immobilization.
- We have performed experiments with free-falling water droplets bouncing onto superhydrophobic structured Si surfaces, quantified their behavior at different impact velocities and made a direct comparison to lotus leaf. It is found that the water repellence of this surface is comparable to that of lotus in terms of a) the lowest velocity sufficient to avoid sticking of the droplets, b) collisional energy loss and c) remnant wetting at high velocities.
- Dynamic control of the wetting behaviour of liquid drops have been achieved by using electrowetting-on-dielectric system based on unstructured and structured Si. Contact angle changes of more than 30° , reversible under certain conditions, have been achieved on such surfaces, upon the application of small electric fields.

- Controllable switching from an initially hydrophobic to a superhydrophilic wetting state has been achieved by chemically induced wetting. Contact of the structured sample-liquid droplet system with vapors of an organic solvent causes abrupt change of the contact angle with time, which may reach up to 90°. Furthermore this process exhibits selectivity, since the system is responsive only for certain organic solvents with specific chemical and physical properties.

Among the advantages of using laser processing for the formation of self-organized surface features, is that it can be applied in a wide range of materials, such as polymers,^[18,175] ceramics,^[18] or metals^[23] in order to control surface topology, and thus open the way to controlling their wettability. Furthermore the possibility of using these Si surfaces as masters for replication of the surface morphology on different materials^[176] as has been shown in **Chapter 3**, makes possible for the combination of laser based techniques and standard replication processes to lead to the manipulation of the wetting response of materials. Materials with tailored wetting response can find use in self cleaning, microfluidics, lab-on-chip devices, chemical sensors, water-proof surfaces etc.

Concluding Remarks

This dissertation has presented a method for inducing morphological, structural and compositional alterations on the surface of Si by combining laser irradiation and chemically induced etching. We have optimized the laser (wavelength, pulse duration, laser fluence, number of pulses) and reactive gas parameters in order to improve each one of the studied properties, as well as for replication purposes.

The main findings of this thesis are summarized below.

a) Increased optical absorptance

The use of laser microstructuring in SF₆ is a promising technique for improving the optical absorptance of Si. We have found that laser structuring improves the optical absorption substantially not only by increasing the absorptance in the wavelengths above the Si band-gap, but also at below-bandgap wavelengths (>1100 nm), where crystalline Si does not normally absorb. Increasing the absorptance of Si up to more than 90% in the wavelength range of 250 nm < λ < 2500 nm, gives the ability of using Si for applications related to detection of NIR wavelengths, which are specifically interesting for telecommunication applications and infrared imaging.

b) Low-threshold field-electron emission

We have found laser structuring of the Si surface in a SF₆ atmosphere to lead to the formation of structures which exhibit low-threshold field electron emission, in both

continuous area and spot array geometries. The field emission threshold can be as low as $2.5 \text{ V}/\mu\text{m}$, in accordance to the optimized standards of current vacuum microelectronics technology. Furthermore, we have demonstrated the feasibility of fabricating Si spike emitters for practical applications, such as cold emission arrays, through a fast and efficient maskless process. These results pave the way for the implementation of laser fabricated Si microstructures in applications such as field emission displays and microwave amplifiers.

c) Wetting response

Finally, we found that laser structuring in a reactive gas atmosphere can be used for rendering the initially hydrophilic Si surface hydrophobic. We were able to manipulate liquid motion on the structured Si surfaces, inducing even uphill motion. By combining laser structuring with the deposition of hydrophobic monolayers, we were able to observe superhydrophobic behavior, comparable to that of the “model” natural superhydrophobic surface, the lotus leaf, and manipulate motion induced by minor gravitational impulses. Furthermore, we performed dynamic measurements to study the water repellency of these Si based structures in direct comparison to the lotus leaf, to find striking similarities. Additionally dynamic manipulation of the wetting response of Si based surfaces could be achieved through electrowetting and chemically induced wetting. Self-cleaning, fabrication of water proof surfaces, low-friction motion in microfluidic and lab-on-chip devices are only a few of the possible applications.

In summary, this thesis has shown that pulsed laser structuring in a reactive gas environment is an efficient technique for improving the properties of Si, and extending its use into new types of application. Even though there are several aspects yet to be interpreted, we believe that we have provided insight to the possible use of Si as a key substrate in interdisciplinary applications. Future research could significantly contribute towards the solution of a puzzle with an already visible motif.

Appendix

Estimation percentage of the cone wet by the liquid.

A1. Macroscopic consideration:

At irradiation regimes ($F_{laser} > 1.0 \text{ J/cm}^2$), we assume that the formed structures resemble cones as seen in Figure 1A:

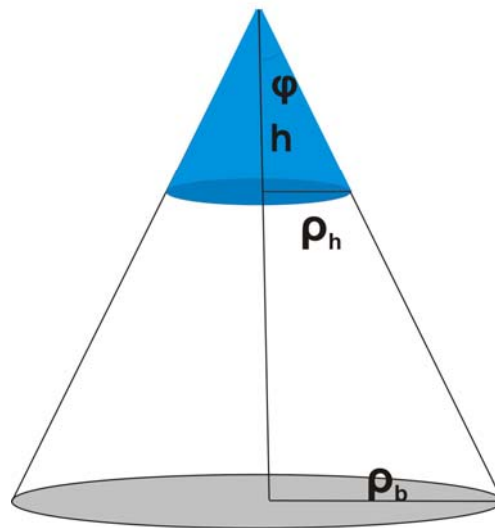


Figure 1A: Conical structure of the silicon spikes formed

$$\cos \theta_{CB} = r_f \cdot f \cdot \cos \theta_Y + f - 1 \quad (1A)$$

$$r_f = \frac{\pi \cdot \rho_h \cdot \sqrt{\rho_h^2 + h^2}}{\pi \cdot \rho_h^2} \quad (2A)$$

$$\tan \varphi = \frac{\rho_h}{h} \Rightarrow h = \frac{\rho_h}{\tan \varphi} \quad (3A)$$

$$(2s)+(3s) \Rightarrow r_f = \frac{\sqrt{\rho_h^2 + \left(\frac{\rho_h}{\tan \varphi}\right)^2}}{\rho_h} \Rightarrow r_f = \sqrt{1 + \frac{1}{(\tan \varphi)^2}} \quad (4A)$$

$$(1s)+(4s) \Rightarrow \cos \theta_{CB} = f \left[\cos \theta_Y \cdot \sqrt{1 + \frac{1}{(\tan \varphi)^2}} + 1 \right] - 1 \quad (5A)$$

*For the samples obtained by irradiation fluences larger than 1.0 J/cm², the contact angle values, and thus, the **solid surface in contact with the liquid are practically constant. For this regime: $\theta_{CB}=131^\circ$, $\theta_Y=66^\circ$, $\varphi=15^\circ$, equation (5A) gives $f=0.13$***

A2. Second lengthscale roughness contribution

We consider the second lengthscale roughness to contribute to the overall roughness of the cones.

The new roughness ratio will then be given by

$$r_f' = \sqrt{1 + \frac{1}{(\tan \varphi)^2}} \cdot (1 + D) \quad (6A)$$

where D represents the second lengthscale roughness contribution to the overall roughness.

We treat the second lengthscale roughness as hemispherical, with a radius of ~50 nm.

$$\text{Then, } D = (2\pi \cdot r_D^2 - \pi \cdot r_D^2) \cdot n, \quad (7A)$$

n being the small scale roughness density per area unit.

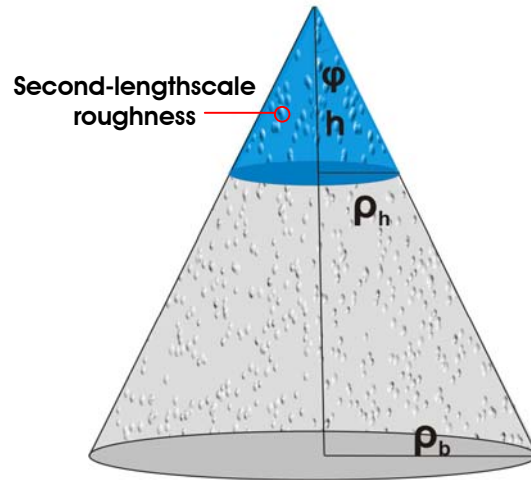


Figure 2A: Conical structure of the formed silicon spikes with the second lengthscale roughness incorporated.

$$(6A)+(7A) \Rightarrow r_f' = \sqrt{1 + \frac{1}{(\tan \varphi)^2} \cdot (1 + \pi \cdot r_D^2 \cdot n)} \quad (8A)$$

For the samples obtained by irradiation fluences larger than 1.0 J/cm^2 , the contact angle values, and thus, the solid surface in contact with the liquid are practically constant. For this regime:

$$\theta_{CB}=131^\circ, \theta_V=66^\circ, \varphi=15^\circ \text{ and } n \sim 16/\mu\text{m}^2$$

$$(8A) \Rightarrow r_f' = 4.5 \quad (9A)$$

The roughness increase due to the second lengthscale roughness is:

$$\% \text{roughness increase} = \frac{r_f' - r_f}{r_f} = 12.5\% \quad (10A)$$

By substituting (9A) in (1A), we find the new fraction f' of the projected solid surface that is wet by the liquid. Comparing this to f (Section A1) we find a decrease of $\sim 7\%$

$$\% \text{ decrease of projected wet area} = \frac{f' - f}{f} = 7\% \quad (11A)$$

Relevant Publications

1. **V. Zorba**, I. Alexandrou, I. Zergioti, A. Neumeister, A. Manousaki, C. Fotakis, C. Ducati, and G.A.J. Amaratunga, “*Laser microstructuring of Si surfaces for low-threshold field-electron emission*”, Thin Solid Films 453, 492 (2004).
2. **V. Zorba**, L. Persano, D. Pisignano, A. Athanassiou, E. Stratakis, R. Cingolani, P. Tzanetakis, C. Fotakis, “*Making silicon hydrophobic: wettability control by two-lengthscale simultaneous patterning with fs-laser irradiation*”, Nanotechnology 17, 3234 (2006).
3. **V. Zorba**, P. Tzanetakis, C. Fotakis, E. Spanakis, E. Stratakis, D. G. Papazoglou, I. Zergioti, “*Silicon electron emitters fabricated by UV laser pulses*”, Appl. Phys.Lett. 88, 081103 (2006).
4. E. Skantzakis, **V. Zorba**, D.G. Papazoglou, I. Zergioti, C. Fotakis “*Ultraviolet laser microstructuring of silicon and the effect of laser pulse duration on the surface morphology*”, Appl. Surf. Science 252, 4462 (2006).
5. **V. Zorba**, E. Stratakis, E. Spanakis, D.G. Papazoglou, I. Zergioti, P.Tzanetakis and C.Fotakis, “*Field Emission properties of arrayed and continuous areas of laser fabricated silicon microstructures*”, J. Nanoengineering and Nanosystems 220, 143 (2006).
6. C. Fotakis, **V. Zorba**, E. Stratakis, A. Athanassiou, P. Tzanetakis, I. Zergioti, D. G. Papagoglou, K. Sambani, G. Filippidis, M. Farsari, V. Pouli, G. Bounos, S. Georgiou, “*Novel Aspects of Materials Processing by Ultrafast Lasers: From Electronic to Biological and Cultural Heritage Applications*”, Journal of Physics: Conference series 59, 266 (2007).
7. **V. Zorba**, “*Tailoring the Optical, Electronic and Wetting properties of Si surfaces by ultrafast laser microstructuring*”, Proc. of the 4th International WLT-Conference on Lasers in Manufacturing 2007, p.769.
8. C. Reinhardt, S. Passinger, **V.Zorba**, B. N. Chichkov, and C.Fotakis, “*Replica molding of picosecond laser fabricated Si microstructures*”, Appl. Phys. A 87, 673 (2007).
9. **V. Zorba**, E. Stratakis, M. Barberoglou, E. Spanakis, P. Tzanetakis and C. Fotakis, “*Tailoring the wetting response of silicon surfaces via fs laser structuring*”, accepted for publication in Appl. Phys.A.
10. E. Spanakis, J. Dialektos, E. Stratakis, **V. Zorba**, P. Tzanetakis and C. Fotakis “*Ultraviolet laser structuring of SiC for cold cathode applications*”, accepted for publication in Phys. Status Solidi (a).
11. **V. Zorba**, N. Boukos, I. Zergioti, C. Fotakis, “*Ultraviolet femtosecond, picosecond and nanosecond laser microstructuring of silicon: structural and optical properties*”, Submitted.
12. **V. Zorba**, E. Stratakis, M. Barberoglou, E. Spanakis, P. Tzanetakis, S. H. Anastasiadis and C. Fotakis “*A laser structured silicon-based surface meets the water repelling performance of the lotus leaf*”, to be Submitted.

References

- [1] E.Jansen, R. Stedman, G.Grossman, H.G. Grimmeiss, *Phys. Rev. B* **29**, 1907 (1984).
- [2] S.Nolte, C.Momma, H.Jacobs, A.Tunnermann, B.N. Chikov, B. Wellegehausen, H.Welling, *J.Opt.Soc. Am. B* **14**, 2716 (1997).
- [3] A.K.Jain, V.N.Kulkarni, D.K.Sood, J.S.Uppol, *J.Appl.Phys* **52**, 4882 (1981).
- [4] J.F.Young, J.E. Sipe, H.M. van Driel, *Phys. Rev. B* **30**(4) , 2001 (1984).
- [5] J.F.Young, J.S. Preston, H.M. van Driel, J.E. Sipe, *Phys. Rev. B* **27**, 1155 (1983).
- [6] M. Henyk, N. Vogel, D. Wolfframm, A. Tempel, J. Reif, *Appl. Phys. A* **69**, S-355 (1999).
- [7] D.von der Linde, K.Sokolowski-Tinten, J. Bialkowski, *Appl. Surf. Sci.* **109/110**, 1 (1997).
- [8] A.C. Tien, S. Backus, H. Kapteyn, M. Mourane, G. Mourou, *Phys. Rev. Lett.* **82**, 3883 (1999).
- [9] P.C.Becker, H.L.Fragrito, C.H.Brito Cruz, R.L. Fork, J.E. Cunningham, J.E.Henry, C.V.Shank, *Phys. Rev. Lett.* **61**, 1647 (1988).
- [10] M. Birnbaum, *J. Appl. Phys.* **36**, 3688 (1965).
- [11] H.J. Leamy, G.A. Rozgonyi, T.T. Sheng, G.K. Celler, *Appl. Phys. Lett.* **32**, 535 (1978).
- [12] G.N. Maracas, G.L. Harris, C.A. Lee, R.A. McFarlane, *Appl. Phys. Lett.* **33**, 453 (1978).
- [13] N.R. Isenor, *Appl. Phys. Lett.* **31**, 148 (1977).
- [14] A. K. Jain, V.N. Kulkarni, D.K. Sood, J.S. Uppol, *J. Appl. Phys.* **52**, 4882 (1981).
- [15] J. Reif, F. Costache, M. Henyk, S.V. Pandelov, *Appl. Surf. Sci.* **197**, 891 (2002).
- [16] F. Costache, M. Henyk, J. Reif, *Appl. Surf. Sci.* **208**, 486 (2003).
- [17] F. Keliman, *Phys. Rev. Lett.* **51**, 2079 (1983).
- [18] D. Bäuerle, *Laser Processing and Chemistry*, Third Edition, Springer-Verlag Berlin Heidelberg New York (2000).
- [19] S. Clark, D.C. Emmony, *Phys. Rev. B* **40**, 2031 (1989).
- [20] M.Y. Shen, C.H. Crouch, J.E. Carey, R. Younkin, E. Mazur, M. Sheehy, C.M. Friend, *Appl. Phys.Lett.* **82**(11), 1715 (2003).
- [21] L.D. Landau and E.M.Lifshitz, *Fluid Mechanics* (Pergamon, London, 1959).
- [22] Q. Wang, A. Feder, E. Mazur, *J.Phys. Chem.* **98**, 12720 (1994).

-
- [23] S.I Dolgaev, S.V. Lavrishev, A.A. Lyalin, A.V. Simakin, V.V. Voronov, G.A. Shafeev, *Appl. Phys. A* **73**, 177 (2001).
- [24] J.E.Carey, C.H.Crouch, E.Mazur, *Optics and Photonics News*, 32, 2/2003.
- [25] K. Seeger and R.E. Palmer, *Appl. Phys. Lett.* **74**,1627 (1999).
- [26] R. Ortega Martinez,T .R. Verhey, P.K. Boyer, and J.J. Rocca, *J. Vac. Sci. Technol.B* **6**,1581 (1988).
- [27] T.J. Chuang, *J. Chem. Phys.* **74**, 1453 (1981).
- [28] F. Raksi, K. Wilson, Z. Jiang, A. Ikhlef, C.Y Cote, J. Kieffer, *J. Chem. Phys.***104**, 6066 (1996).
- [29] J.D.Fowlkes, A.J.Pedraza, D.H.Lowndes, *Appl. Phys. Lett.* **77**, 1629 (2000).
- [30] F.Sanchez, J.L.Morenza, R.Aguiar, J.C.Delgado, M.Varela, *Appl. Phys. Lett.* **69**, 620 (1996).
- [31] F.Sanchez, J.L.Morenza, R.Aguiar, J.C.Delgado, M.Varela, *Appl. Phys. A* **66**, 83 (1996).
- [32] A.J.Pedraza, J.D.Fowlkes, D.H.Lowndes, *Appl. Phys. Lett.* **74**, 2322 (1999).
- [33] J.D.Fowlkes, A.J.Pedraza, D.H.Lowndes, *Appl. Phys. Lett.* **77**, 1629 (2000).
- [34] A.A. Evtukh, E.B. Kaganovich, V. G. Litovchenko, Yu.M. Litvin, D.V. Fedin, E.G. Manoilov, S.V. Svechnikov, *Semiconductor Physics, Quantum Electronics & Optoelectronics*, **3(4)**, 474 (2000).
- [35] A.V. Karabutov, V.D. Frolov, E.N. Loubnin, A.V. Simakin, G.A. Shafeev, *Appl. Phys. A* **76**, 413 (2003) .
- [36] A. V. Karabutov, V. D. Frolov, A. V. Simakin, G. A. Shafeev, *J. Vac. Sci. Technol. B* **21**, 449 (2003).
- [37] T-H.Her, R.J.Finlay, C.Wu, S.Deliwala, E.Mazur, *Appl. Phys. Lett.* **73** 1673 (1998).
- [38] T-H.Her, R.J.Finlay, C.Wu, E.Mazur, *Appl. Phys. A* **70** 383 (2000).
- [39] T. Baldacchini, J. E. Carey, M. Zhou, E. Mazur, *Langmuir* **22**, 4917 (2006).
- [40] S. Szatmári and F. P. Schäfer, *Optics Communications* **68**, 196 (1988).
- [41] P. Simon, H. Gerhardt, S. Szatmári, *Optics Communications* **71**, 305 (1989).
- [42] D. Oner, T. J. McCarthy, *Langmuir* **16**, 7777 (2000).
- [43] R. C. Smith, D. C. Cox, and S. R. P. Silva, *Appl. Phys. Lett.* **87**, 1031121 (2005)
- [44] C. H. Crouch, J. E. Carey, J. M. Warrender, M. J. Aziz, E. Mazur and F. Y. Genin *Appl. Phys. Lett.* **84** 1850 (2004).
- [45] C. H. Crouch, J. E. Carey, M.Y Shen, E. Mazur and F. Y. Genin *Appl. Phys. A* **79** 1635 (2004).

-
- [46] R.F. Egerton, *Electron Energy-Loss Spectroscopy in the Electron Microscope*, (Plenum Press, New York, 1996).
- [47] W. M. Skiff, R. W. Carpenter and S. H. Lin, *J. Appl. Phys.* **62** 2439 (1987).
- [48] M. Worchl, H.J. Engelmann, W. Blum, E. Zschech, *Thin Solid Films* **405**, 198 (2002).
- [49] G.A. Botton, M.W. Phaneuf, *Micron* **30** 109 (1999).
- [50] G. Duscher, R. Buczko, S. J. Pennycook, S. T. Pantelides, *Ultramicroscopy* **86**, 355 (2001).
- [51] K. Hayakawa, T. Fujikawa, S. Muto, *Chem. Phys. Lett.* **371**, 498 (2003).
- [52] D.H.Lowndes, J.D.Fowlkes, A.J.Pedraza, *Appl. Surf. Sci.* 154-155 647 (2000).
- [53] X. Zeng, X. Mao, R. Greif, R.E. Russo, *Proc. SPIE* **5448**, 1150 (2004).
- [54] E. Skantzakis, V.Zorba, D.G. Papazoglou, I. Zergioti, C.Fotakis, *Appl. Surf.Sci.* **252**, 4462 (2006).
- [55] M. Born, E. Wolf, *Principles of Optics*, Cambridge University Press, Cambridge, UK, 2003.
- [56] H.R. Philipp, E.A. Taft, *Phys. Rev.* **120** (1) (1960) 37.
- [57] J.R. Chelikowsky, M.L. Cohen, *Phys. Rev. B* **14** (2) (1976) 556.
- [58] C.Wu, PhD thesis-Harvard (2001).
- [59] J. Serbin, A. Egbert, A. Ostendorf, B.N. Chichkov, R. Houbertz, G. Domann, J. Schulz, C. Cronauer, L. Fröhlich, M.Popall, *Opt. Lett.* **28**, 301 (2003).
- [60] J. Serbin, A. Ovsianikov, B.N. Chichkov, *Opt. Express* **12**, 5221 (2004).
- [61] A. Ostendorf and B. N. Chichkov, *Photonics Spectra*, October, 72 (2006).
- [62] Ying Zhang, Chi-Wei Lo, J. Ashley Taylor, S.Yang, *Langmuir* **22**, 8595 (2006).
- [63] P. Holgerson , D.S. Sutherland, B. Kasemo, D. Chakarov, *Appl. Phys. A* **81**, 51 (2005).
- [64] J. Oh, J. C. Campbell, S. G. Thomas, S. Bharatan, R. Thoma, C. Jasper, R. E. Jones, T. E. Zirkle, *IEEE Photonics Technol. Lett.* **38**, 1238 (2002).
- [65] Z. Huang, J. Oh, and J. C. Campbell, *Appl. Phys. Lett.* **85**, 2386 (2004).
- [66] J. M. Palmer, *Handbook of Optics* (McGraw-Hill,1995).
- [67] R. Menzel, *Photonics: Linear and Nonlinear Interactions of Laser Light and Matter*, .Springer-Verlag Berlin Heidelberg (2001).
- [68] C.H. Seager,P .M. Lenahan, K. L. Brower, and R.E. Mikawa, *J. Appl. Phys.* **58**, 2704(1985).
- [69] W.B. Jackson,N .M. Johnson, D.K. Biegelsen, *Appl. Phys. Lett.* **43**, 195 (1983).
- [70] W.B. Jackson and N.M. Amer. *Phys. Rev. B* **25**, 5559 (1982).

-
- [71] J.I. Pankove, *Optical Processes In Semiconductors* (New York: Dover Publications, Inc. 1971)
- [72] Z.Huang, J. E. Carey, M. Liu, X. Guo, E. Mazur, J. C. Campbell, *Appl. Phys.Lett.* **89**, 033506 (2006).
- [73] J. E. Carey, C. H. Crouch, M. Shen, E. Mazur, *Optics Letters* **30**, 1773 (2005).
- [74] K. Okano, T. Yamada, A. Sawabe, S. Koizumi, J. Itoh, G. A. J. Amaratunga, *Appl. Phys. Letters* **79**, 275 (2001).
- [75] R. E. Mitchell, J. B. A. Mitchell, J. W. McGowan, *J. Phys. E: Sci. Instrum.* **18**, 1031 (1985).
- [76] N. A. Fox, W. N. Wang, T. J. Davis, J. W. Steeds, P. W. May, *Appl. Phys. Lett.* **71**, 2337 (1997).
- [77] A.Y. Tcherepanov, A.G. Chakhovskol, V.B. Sharov, *J. Vac. Sci. Technol. B* **13**, 482 (1995).
- [78] T. Asano, E. Shibata, D. Sasaguri, K. Makihira, and K. Higa, *Jpn. J. Appl. Phys.* **36**, 818 (1997).
- [79] A. Baba, K. Higa, and T. Asano, *Proc. Inter. Displ. Workshop.* **4**, 703 (1998).
- [80] C. Lea, *Journal of Physics D: Applied Physics* **6**, 1105 (1973).
- [81] Q.H. Wang, T.D. Corrigan, J.Y. Dai, R.P.H. Chang, A. R. Krauss, *Appl. Phys. Lett.* **70**, 3308 (1997).
- [82] Y. Saito, S. Uemura, *Carbon* **38**, 169 (2000).
- [83] M. C.-C. Lin, H. J. Lai, M.S. Lai, M. H. Yang, A. K. Li, *Mater.Phys.Mech.* **4**, 138 (2001)
- [84] C. A. Spindt, *J.Appl.Phys* **39**, 3504 (1968).
- [85] D. Nicolaescu, *Romanian Journal of Information Science and Technology* **3**, 129 (2000).
- [86] R. Gomer, *Field Emission and Field Ionization* (Harvard University Press, Massachusetts, US, 1961)
- [87] H.H.Busta, *J.Micromech.Microeng.* **2**, 43 (1992).
- [88] D. W. Tuggle, J. Z. Li, L. W. Swanson, *J. Microscopy* **140**, 293 (1985).
- [89] RH Fowler, LW Nordheim, *Proc. R. Soc. London, Ser. A* **119**,173 (1928).
- [90] Y. Endo, I. Honjo, S. Goto, *J. Vac. Sci. Technol. B* **16**, 3082 (1998).
- [91] S. Johnson, A. Markwitz, M. Rudolphi, H. Baumann, S.P.Oei, K. B. K. Teo, W. I. Milne, *Appl. Phys. Lett.* **85**, 3277 (2004).
- [92] V. Zorba, I. Alexandrou, I. Zergioti, A. Manousaki, C. Ducati, A. Neumeister, C. Fotakis, G.A.J. Amaratunga, *Thin Solid Films* **453**, 492 (2004).
- [93] T. Utsumi, *IEEE Trans. Electron Devices* **38**, 2276 (1991).

-
- [94] A. Modinos, "Field, Thermionic, and Secondary Electron Emission Spectroscopy", Plenum Press, New York (1984).
- [95] M. Ding, H. Kim, A. Akinwande, *Appl. Phys. Lett.* **75**, 823 (1999).
- [96] G. C. Kokkorakis, A. Modinos, J. P. Xanthakis, *J. Appl. Phys.*, **91**, 7 4580 (2002).
- [97] L. Nilsson, O. Groening, C. Emmenegger, O. Kuettel, E. Schaller, L. Schlapbach, H. Kind, J-M. Bonard, K. Kern, *Appl. Phys. Lett.* **76**, 2071 (2000).
- [98] Q. Zhao, H. Z. Zhang, Y. W. Zhu, S. Q. Feng, X. C. Sun, J. Xu, D. P. Yu, *Appl. Phys. Lett.* **86**, 2031151 (2005).
- [99] F. H. Read, N. J. Bowring, *Nucl. Instr. Meth. Phys. Res. A* **519**, 305, (2004).
- [100] T. Inoue, F. Ogletree, M. Salmeron, *Appl. Phys. Lett.* **76**, 2961 (2000).
- [101] K.C. Kao, W. Hwang, *Electrical Transport in Solids* Pergamon, Oxford (1981).
- [102] W. B. Choi, D. S. Chung, J. H. Kang, H. Y. Kim, Y. W. Jin, I. T. Han, Y. H. Lee, J. E. Jung, N. S. Lee, G. S. Park, J. M. Kim, *Appl. Phys. Lett.* **75**, 3129 (1999).
- [103] <http://www.digitaltvdesignline.com/news/199100133>
- [104] W. Barthlott, C. Neinhuis, *Planta* **202**, 1 (1997).
- [105] A. Nakajima, A. Fujishima, K. Hashimoto, T. Watanabe, *Adv. Mater.* **11**, 1365 (1999).
- [106] Z. Yoshimitsu, A. Nanajima, T. Watanabe, K. Hashimoto, *Langmuir* **18**, 5818 (2002).
- [107] N. A. Patankar *Langmuir* **19**, 1249 (2003).
- [108] W. Lee, M. K. Jin, W. C. Yoo, J. K. Lee, *Langmuir* **20**, 7665 (2004).
- [109] G. S. Watson, J.A. Watson: *Appl. Surf. Sci.* **235**, 139 (2004).
- [110] J.-Y. Shiu, C.-W. Kuo, P. Chen C.-Y. Mou : *Chem. Mater.* **16**, 561 (2004).
- [111] P. N. Bartlett, J. J. Baumberg, P. R. Birkin, M. A. Ghanem, M. C. Netti: *Chem. Mater.* **14**, 2199 (2002).
- [112] I. Woodward, W. C. E. Schofield, V. Roucoules, J. P. S. Badyal: *Langmuir* **19**, 3432 (2003).
- [113] E. Martines, K. Seunarine, H. Morgan, N. Gadegaard, C. D. W. Wilkinson, M. O. Riehle: *Nano Lett.* **5**, 2097 (2005).
- [114] K. K. S. Lau, J. Bico, K. B. K. Teo, M. Chhowalla, G. A. J. Amaratunga, W. I. Milne, G. H. McKinley, K. K. Gleason: *Nano Lett.* **3**, 1701 (2003).
- [115] V. Zorba, L. Persano, D. Pisignano, A. Athanassiou, E. Stratakis, R. Cingolani, P. Tzanetakis, C. Fotakis: *Nanotechnology* **17**, 3234 (2006).
- [116] N. S. Murthy, R. D. Prabhu, J. J. Martin, L. Zhou, , R. L Headrick.: *J. Appl. Phys.* **100**, 023528 (2006).

-
- [117] P.G. De Gennes, *Rev. Mod. Phys.* **57**, 827 (1985).
- [118] L. Leger, J.F. Joanny, *Rep. Prog. Phys.* **55**, 431 (1992).
- [119] G. McHale, N.J. Shirtcliffe, M.I. Newton, *Langmuir* **20**, 10146 (2004)
- [120] R. N. Wenzel, *Ind. Eng. Chem.* **28**, 988 (1936).
- [121] A. B. D. Cassie, S. Baxter, *Trans. Faraday. Soc.*, **40**, 546 (1944).
- [122] A. Marmur, *Langmuir* **19**, 8343 (2003).
- [123] R. Younkin, J. E. Carey, E. Mazur, J. A. Levinson, C. M. Friend, *J.Appl.Phys.* **93**, 2626 (2003).
- [124] M. Morita, T. Ohmi, E. Hasegawa, M. Kawakami, K. Suma, *Appl.Phys.Lett.* **55**, 562 (1989).
- [125] H. Shimizu, C. Munakata, *Semicond.Sci.Technol.* **5**, 842 (1990).
- [126] N. J. Shirtcliffe, G. McHale, M. I. Newton, C. C. Perry, *Langmuir* **21** 937 (2005).
- [127] A.M. Cazabat, F. Heslot, S. M. Troian, P. Carles, *Nature* **346** 842 (1990).
- [128] M. K. Chaudhury, M. Whitesides, *Science* **256**, 1539 (1992).
- [129] B. S. Gallardo, V. K. Gupta, F. D. Eagerton, L. I. Jong, V. S. Craig, R. R. Shah, N. L. Abbott, *Science* **283**, 57 (1999).
- [130] K. Ichimura, S. K. Oh, M. Nakagawa *Science* **288**, 1624 (2000).
- [131] G. C. H. Mo, W. Liu, D. Y. Kwok, *Langmuir* **21**, 5777 (2005).
- [132] T. Sun, L. Feng, X. Gao, L. Jiang, *Acc. Chem. Res.* **38**, 644 (2005).
- [133] Z. Gao, J. Lei, *Nature* **432**, 36 (2004).
- [134] W. R. Ashurst, C. Carraro, R. Maboudian: *IEEE Transactions on device and materials reliability* **3**, 173 (2003).
- [135] S. R. Wasserman, Y.-T. Tao, G. M. Whitesides, *Langmuir* **5**, 1074 (1989).
- [136] M. K. Chaudhury, M. Whitesides, *Science* **256**, 1539 (1992).
- [137] B. S. Gallardo, V. K. Gupta, F. D. Eagerton, L. I. Jong, V. S. Craig, R. R. Shah, N. L. Abbott, *Science* **283**, 57 (1999).
- [138] K. Ichimura, S. K. Oh, M. Nakagawa, *Science* **288**, 1624 (2000).
- [139] A. Lafuma, D. Quere, *Nature Materials*, **2**, 457 (2003).
- [140] D. Quere, A. Lafuma, J. Bico, *Nanotechnology* **14**, 1109 (2003).
- [141] V. Bergeron, D. Bonn, J. Y. Martin, L. Vovelle, *Nature* **405**, 772 (2000).
- [142] D. Bartolo, F. Bouamrine, E. Verneuil, A. Buguin, P. Silberzan, S. Moulinet, *Europhys. Lett.* **74** 299 (2006).
- [143] F. Mugele, J.-C. Baret, *J. Phys.: Condens. Matter* **17**, R705 (2005).
- [144] M. G. Pollack, A. D. Shenderov, R. B. Fair, *Lab Chip* **2**, 96 (2002).

-
- [145] K. Mohseni, A. Dolatabadi *Proc. 43rd AIAA Aerospace Sci. Meet. Exhib.*, 0677 (2005).
- [146] J. S. Kuo, P. Spicar-Mihalic, I. Rodriguez, D. T. Chiu, *Langmuir* **19**, 250 (2003).
- [147] R. B. Fair, V. Srinivasan, H. Ren, P. Paik, V. K. Pamula, M. G. Pollack, *Technical Digest IEEE International Electron Dev. Meeting*, 779 (2003).
- [148] V. Srinivasan, V. K. Pamula, R. B. Fair, *Lab Chip* **4**, 310 (2004).
- [149] S. K. Cho, H. J. Moon, C. J. Kim, *J. Microelectromech. Syst.* **12**, 70 (2003).
- [150] Y. Fouillet, J. L. Achard, *C. R. Physique* **5**, 577 (2004).
- [151] B. Berge, J. Peseux, *Eur. Phys. J. E* **3**, 159 (2000).
- [152] R. A. Hayes, B. J. Feenstra, *Nature* **425**, 383 (2003).
- [153] B. R. Acharya, T. Krupenkin, S. Ramachandran, Z. Wang, C. C. Huang, J. A. Rogers, *Appl. Phys. Lett.* **83**, 4912 (2003).
- [154] J. Lee, C. J. Kim, *J. Microelectromech. Syst.* **9**, 171 (2000).
- [155] G. Lippmann, *Ann. Chim. Phys.* **5**, 494 (1875).
- [156] A. Froumkine, *Actual. Sci.* **373**, 1 (1936).
- [157] J. A. M. Sondag-Huethorst, L. G. J. Fokkink, *J. Electroanal. Chem.* **367**, 49 (1994)
- [158] J. A. M. Sondag-Huethorst, L. G. J. Fokkink, *Langmuir* **10**, 4380 (1994)
- [159] B. Berge, *C. R. Acad. Sci. III* **317**, 157 (1993).
- [160] M. Vallet, B. Berge, L. Vovelle, *Polymer* **37**, 2465 (1996)
- [161] M. Vallet, B. Berge, M. Vallade, *Eur. Phys. J. B* **11**, 583 (1999)
- [162] W. J. J. Welters, L. G. J. Fokkink, *Langmuir* **14**, 1535 (1998)
- [163] N. Ivosevic, V. Zutic, *Langmuir* **14**, 231 (1998).
- [164] V. Bahadur, S. V. Garimella, *Langmuir* **23**, 4918 (2007).
- [165] T. N. Krupenkin, J. A. Taylor, T. M. Schneider, S. Yang, *Langmuir* **20**, 3824 (2004).
- [166] N. Verplanck, E. Galopin, J. C. Camart, V. Thomy, *Nano Lett.* **7**, 813 (2007).
- [167] H. J. I. Verheijen, M. W. J. Prins, *Langmuir* **15**, 6616 (1999).
- [168] E. Seyrat, R. A. Hayes, *J. Appl. Phys.* **90**, 1383 (2001).
- [169] M. Vallet, M. Vallade, B. Berge, *Eur. Phys. J. B* **11**, 583 (1999).
- [170] T. N. Krupenkin, J. A. Taylor, E. N. Wang, P. Kolodner, M. Hodes, T. R. Salamon, *Langmuir* **23**, 9128 (2007).
- [171] T. Krupenkin, J. A. Taylor, P. Kolodner, M. Hodes, *Bell Labs Technical Journal* **10**, 161 (2005).
- [172] R. B. Bjorklund, S. Zangoie, H. Arwin, *Appl. Phys. Lett.* **69** 3001 (1996).

- [173] L. De Stefano, I. Rendina, L. Moretti, S. Tundo, A. M. Rossi, *Appl. Optics* **43**, 167 (2004)
- [174] G. Garcia Salgado, T. Diaz Becerril, H. Juarez Santiesteban, E. Rosendo Andres *Optical Materials* **29**, 51 (2006)
- [175] N. S. Murthy, R. D. Prabhu, J. J. Martin, L. Zhou, , R. L Headrick, *J. Appl. Phys.* **100**, 023528 (2006).
- [176] C. Reinhardt, S. Passinger, V. Zorba, B.N. Chichkov, C. Fotakis, *Appl. Phys. A* **87**, 673 (2007).